SELF-CATALYZED AND CATALYST-FREE III-V SEMICONDUCTOR NANOWIRES GROWN BY CBE

by

Omer Arif

Supervisor: Prof. Lucia Sorba

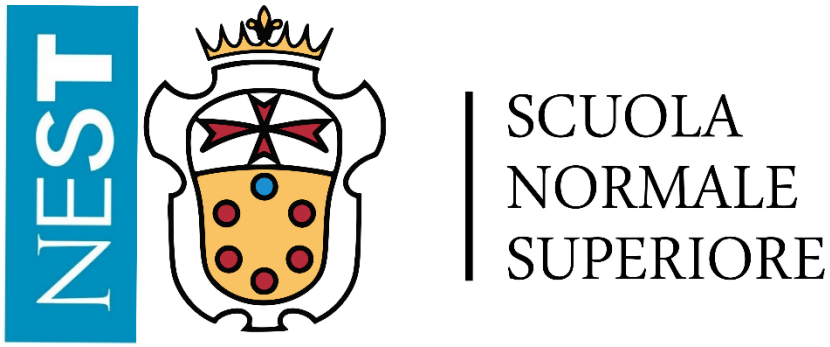

A thesis submitted in fulfilment for the degree of

Doctor of Philosophy

of

Scuola Normale Superiore

Pisa, Italy

26 February 2021

Abstract

In this thesis, the growth dynamics and mechanisms of III-V semiconductor nanowires (NWs) and their heterostructures are studied. III-V NWs are realized by self-catalyzed and catalyst-free growth methods on Si (111) substrates by means of chemical beam epitaxy. The Au-free growth approach is particularly important for the integration of III-V semiconductors on silicon toward a CMOS-compatible electronics. The morphological and structural properties of the grown NWs are investigated by scanning (SEM) and transmission electron microscopy (TEM). These NWs exhibit very high aspect ratio and good material quality, which makes them useful to be employed for fundamental studies as well as for application in electronics and optoelectronics.

The first part of the thesis is focused on the growth of InAs/InP/GaAsSb core-dual-shell (CDS) NWs. Detailed morphological, structural, and compositional analyses of the NWs as a function of growth parameters are carried out by SEM, TEM, and by energy-dispersive X-ray spectroscopy. Furthermore, by combining the scanning transmission electron microscopy-Moiré technique with geometric phase analysis, we studied the residual strain and the relaxation mechanisms in this system. We found that InP shell facets are well-developed along the crystallographic <110> and <112> directions only when the nominal thickness is above 1 nm, suggesting an island-growth mode. Moreover, the crystallographic analysis indicates that both InP and GaAsSb shells grow almost coherently to the InAs core along the ⟨112⟩ direction and elastically compressed along the ⟨110⟩ direction. For an InP shell thickness above 8 nm, some dislocations and roughening occur at the interface. This study provides useful general guidelines for the fabrication of high-quality devices based on these CDS NWs. Indeed, we investigated the tunnel coupling between the outer p-type GaAsSb shell and the n-type InAs core in InAs/InP/GaAsSb CDS NWs. Low-temperature (4.2 K) transport measurements in the shell-shell configuration in CDS NWs with 5 nm-thick InP barrier reveal a weak negative differential resistance. Differently, when the InP barrier thickness is increased to 10 nm, this negative differential resistance is fully quenched. The electrical resistance between the InAs core and the GaAsSb shell, measured in core-shell configuration, is significantly

higher with respect to the resistance of the InAs core and of the GaAsSb shell. The field effect, applied via a back-gate, has an opposite impact on the electrical transport in the core and in the shell portions. Our results show that electron and hole free carriers populate the InAs and GaAsSb regions respectively and indicate InAs/InP/GaAsSb CDS NWs as an ideal system for the investigation of the physics of interacting electrons and holes at the nanoscale.

The second part of this thesis is dedicated to the growth of self-catalyzed InAs/InSb axial heterostructures. The growth mechanisms of these heterostructures are thoroughly investigated as a function of the In and Sb line pressures, and growth time. Some interesting phenomena are observed and analysed. In particular, the presence of an In droplet on top of the InSb segment is shown to be essential to form axial heterostructures in the self-catalyzed vapor-liquid-solid mode. Axial versus radial growth rates of InSb segments are investigated under different growth conditions and described within a dedicated model containing no free parameters. It is shown that a widening of the InSb segment with respect to the InAs stem is caused by the vapor-solid growth on the nanowire sidewalls rather than by the droplet swelling. The In droplet can even shrink smaller than the nanowire facet under Sb-rich conditions.

The third part of the thesis is focused on the realization of self-catalyzed InSb quantum dot (QD) embedded into InAs NW. A systematic study on the influence of the growth parameters on the morphology of such NWs is performed. Radial and axial growth rates are studied as a function of growth parameters in order to realize InSb QD NW with controlled morphology. In particular, we have explored different growth conditions to minimize the InAs shell around the InSb QD. We found that the shell thickness around the InSb QD decreases with increasing growth temperature while it increases with an increase of the As line pressure. Furthermore, from the high resolution-TEM analysis, we observed that InAs-stem and InAs-top segment have a wurtzite (WZ) crystal structure with several defects such as stacking faults and twins perpendicular to the growth direction. It is commonly observed that the InAs NWs grown by catalyst-free and self-catalyzed growth methods show highly defective (or mixed WZ/ZB) crystal structure. By contrast, here the InSb QD shows a defect-free zincblende (ZB) crystal structure without any stacking faults, consistently with the energetically preferred cubic structure of the InSb crystals generally attributed to the low ionicity of group III to Sb bonds. This study gives useful information for the

realization of InSb QDs with controlled morphology and optimized quality embedded in InAs NWs in the self-catalyzed regime.

Contents

List of Abbreviations

BF	Bright-field
BOE	Buffered oxides etch
BR	Bragg reflection
CBE	Chemical beam epitaxy
CDS	Core-dual-shell
CF	Catalyst-free
CMOS	Complementary metal–oxide–semiconductor
CS	Core-shell
DF	Dark-field
EBL	Electron beam lithography
EDX	Energy-dispersive X-ray spectroscopy
FET	Field effect transistor
FFT	Fast Fourier Transform
FIB	Focused ion beam
GPA	Geometric phase analysis
HAADF	High angle annular dark field
HR-TEM	High resolution transmission electron microscopy
HS	Heterostructures
MBE	Molecular beam epitaxy
MO	Metal-organic
MOCVD	Metal-organic chemical vapor deposition
NDR	Negative differential resistance
NP	Nanoparticle
NWs	Nanowires
QDs	Quantum dots
RHEED	Reflection high-energy electron diffraction
SC	Semiconductor
SEM	Scanning electron microscopy
STEM	Scanning transmission electron microscopy
TBAs	Tertiarybutylarsine
TBP	Tertiarybutylphosphine
TDMASb	Tris(dimethylamino)antimony
TEGa	Triethylgallium
TEM	Transmission electron microscopy
TFET	Tunnel field effect transistor
TMAl	Trimethylaluminum
TMIn	Trimethylindium
TMSb	Trimethylantimony
UHV	Ultrahigh vacuum
VLS	Vapor-liquid-solid
VS	Vapor-solid
WZ	Wurtzite
XRD	X-ray diffraction
ZB	Zincblende

Statement of Original Authorship

The work contained in this thesis has not been previously submitted to meet requirements for an award at this or any other higher education institution. To the best of my knowledge and belief, the thesis contains no material previously published or written by another person except where due reference is made in the text.

Signature: omer arif

Date: 26-02-2021

Acknowledgements

First of all, it is a great pleasure for me to express my respect and a deep sense of gratitude to my Ph.D. supervisor Prof. Lucia Sorba, for the opportunity and the confidence that she provided me to pursue my Ph.D. at NEST, Scuola Normale Superiore. I am thankful for her wisdom, vision, expertise, guidance, enthusiastic involvement, and persistent encouragement during the planning and development of this research work. I also gratefully acknowledge her efforts on improving the manuscript.

I am thankful to Dr. Valentina Zannier for her valuable training and advice to use the CBE system and hundreds of discussions e.g. about the growth and the crystal structure of nanowires. Her creative ideas have helped me tremendously to design well-planned experiments, analyse the data and write articles in a clear and concise way.

I am also thankful to Dr. Daniele Ercolani for giving me scientific and technical training in various characterization techniques. For many fruitful discussions and for sharing his knowledge with me. His kind and friendly nature give me an opportunity to learn a lot from him.

I am also thankful to Dr. Francesca Rossi for performing TEM measurements of our nanowires, for many fruitful discussions, and for sharing her expertise with us.

I am deeply grateful to our collaborators Prof. Vladimir G. Dubrovskii, Dr. Ang Li, Dr. Francesco Rossella, and Dr. Sedighe Salimian for their contribution to complete this work.

I am obliged to my parents, siblings, and friends back home in Pakistan for their moral support, love, encouragement, and blessings to complete this task.

Finally, I wish to express my appreciation to my friends at SNS Akash, Ajesh, Neeraj, Chamseddine, Ayush, Mahdi, and Isha. I also would like to express my deep and sincerely thanks to my friends and all other persons whose names do not appear here, for helping me either directly or indirectly in all even and odd times.

Omer Arif

List of Publications

1. **Arif, O.**; Zannier, V.; Li, A.; Rossi, F.; Ercolani, D.; Beltram, F.; Sorba, L. Growth and Strain Relaxation Mechanisms of InAs/InP/GaAsSb Core-Dual-Shell Nanowires. *Cryst. Growth Des.* **2020**, *20*, 1088–1096.
2. **Arif, O.**; Zannier, V.; Dubrovskii, V. G.; Shtrom, I. V.; Rossi, F.; Beltram, F.; Sorba, L. Growth of Self-Catalyzed InAs/InSb Axial Heterostructured Nanowires: Experiment and Theory. *Nanomaterials* **2020**, *10*, 494.
3. Salimian, S.; **Arif, O.**; Zannier, V.; Ercolani, D.; Rossi, F.; Momtaz, Z. S.; Beltram, F.; Roddaro, S.; Rossella, F.; Sorba, L. Electrical probing of carrier separation in InAs/InP/GaAsSb core-dualshell nanowires. *Nano Res.* **2020**, *13*, 1065–1070.
4. **Arif, O.**; Zannier, V.; Rossi, F.; Ercolani, D.; Beltram, F.; Sorba, L. Self-Catalyzed InSb/InAs Quantum Dot Nanowires. *Nanomaterials* **2021**, *11*, 179.

Chapter 1: Introduction

1.1 Background

Material science is one of the key fields in the development of humankind. Design, engineering and discovery of new types of materials, ceramics, metals, semiconductors, and biomaterials are very crucial to establish new applications and devices, which will facilitate people in order to carry their daily life activities in a more appropriate and easiest way. The present study is dedicated to the realization of novel nanosystems based on semiconductor (SC) materials in which carriers are confined in one or more directions. SC nanostructures have already played their role in a vast range of different applications. In fact, they are important building blocks of modern electronics and optoelectronics [1] which enable the technology that helps us to communicate, entertain, travel, control the energy and many more. Furthermore, according to the Moore's law, the miniaturization of integrated circuits by scaling down the device dimensions has been the principal driver for the SC technology roadmap in the last decades [2,3]. Indeed, the advantage of SC materials with low dimension is not only to reduce the size of devices but it also helps for high speed and low power consumption electronics. However, the big problem with the current CMOS technology is high power consumption due to increment of leakage currents and saturation of supply voltage [4,5]. In order to overcome this problem, new materials and new device architectures are required. Therefore, novel one-dimensional SC nanowires (NWs) based devices are proposed as one of the potential candidates due to high capability to inject more carriers in a faster manner [6].

1.2 III-V semiconductor NWs

Semiconductor NWs are defined as quasi-one dimensional crystalline structures with diameters typically less than 100 nm and length of several μm [7]. They have unique geometry and free-standing nature which confer significant advantages over conventional SC planar geometry such as high surface to volume ratio, efficient strain relaxation [8], wave-guiding nature [9,10], and improved light trapping properties [11,12]. These extraordinary properties make them suitable for a wide range of applications in electronic, optoelectronics, biological and chemical sensors [13-30].

In this thesis, different types of SC NWs are investigated such as InAs, InP, and Sb-based NWs. InAs NWs, due to their low energy band gap and high electron mobility have been employed to realize devices, including high-speed electronic devices [31], tunnel field effect transistors (FETs) [32], single-electron transistors [19], resonance tunneling diodes [26], gas sensors [33], and field emission sources [34]. Sb-based SC NWs like InSb, GaSb and their ternary alloys have attained great interest for a lot of potential applications such as low power high-speed electronics [35], thermoelectric generation [35,36], quantum transport [37], Majorana fermions [38], and mid to long infrared optoelectronics [39]. This is due to their properties such as very narrow band gap, broken type-III band gap, high hole mobilities, low effective masses, strong spin-orbit interactions, and large g-factor [35,40-42].

1.3 Growth methods of NWs

The realization of SC NWs is achieved by several growth methods. They are mainly categorized into two different approaches: top-down and bottom-up. In the top-down approach, the realization of NWs starts with high quality bulk material from which ordered arrays of nanostructures are obtained by a combination of different lithographic and selective etching techniques. This approach has several limitations, such as that only SC materials and SC material combinations already existing in the bulk form can be used. Furthermore, excess of material is used and a carefully control of the etching process is required because it can degrade the quality of the material. Moreover, as the length of devices reduces, the top-down method is becoming problematic to control all the process to get high quality material at nanoscale [43-45].

Instead, the bottom-up approach helps to overcome many of these issues. The bottom-up method involves the direct synthesis of NWs and the result depends upon starting material that grows on the substrates by providing proper growth conditions such as temperature, beam flux and ratio [43-45]. By growing the NWs with this method, it is possible to carefully control different combinations of materials. The bottom-up method provides opportunities for the fabrication of atomically sharp and complex NWs. Several epitaxial techniques have been used for the NW growth such as molecular beam epitaxy (MBE), chemical beam epitaxy (CBE), metal-organic or solid source chemical vapor deposition (CVD), and pulsed laser ablation [40]. Within the bottom-up approach, there are several methods to grow NWs such as metal-seeded, self-catalyzed, and catalyst-free [43-45].

1.3.1 Metal-seeded growth protocol

The most common metal seeded growth method is also known as a vapor-liquid-solid (VLS) mechanism. It is the most widely used method. It was first introduced by Wagner and Ellis in 1964 [46] to explain the growth mechanism of silicon (Si) wires catalyzed by Au particles. In general, the NW growth formation depends on an anisotropy of the growth rate. The NWs nucleate in a single point where the Au seed is located and elongate in one direction in which the highest growth rate exists. The slower growth rate in the other directions constrains the NWs to develop a one-dimensional (1D) shape. The VLS growth mechanism consists of three phases as shown in Fig. 1.1: (i) the formation/deposition of solid catalyst nanoparticles onto a crystalline substrate, (ii) alloying and melting of the precursors with the catalyst nanoparticle, and (iii) nucleation and growth of the NW. The Si precursor is provided in the vapor phase at a given growth temperature, the Au seed forms a liquid eutectic alloy with the Si. The Au-Si alloy particle reaches supersaturation with a further supply of Si, and the Si crystal precipitates at the particle-semiconductor interface to develop a solid crystalline Si wire [43,45].

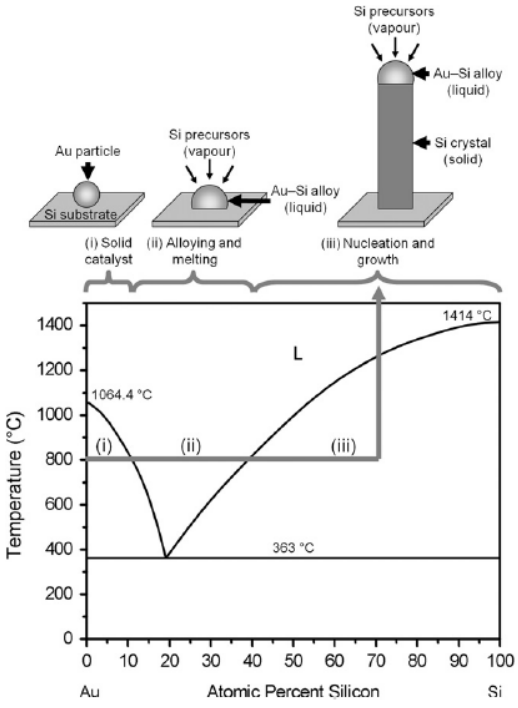

Figure 1.1. Schematic diagram of the VLS growth process of Si wires using an Au catalyst particle. The Au-Si binary phase diagram illustrated in the lower portion describes that different phases of the Au–Si particle can be achieved under different growth temperatures and composition ranges. Labels (i), (ii), and (iii) explain the different levels of nanowire growth for a growth temperature of 800 °C, and the corresponding state of the Au–Si particle, Figure is an adopted from Ref. [45].

Wagner and Ellis deduced possible explanations to describe the Si NW growth. The metal particle acts as a catalyst, which decreases the activation energy barriers and increases the decomposition rate of the gas-phase precursors. The liquid droplet also helps to reduce the melting temperature of Au and Si to form Au-Si metal alloy droplets, which behave as preferential sites for the absorption of Si to introduce supersaturation of the alloy droplet from the vapor source, which leads towards a nucleation of a solid Si phase. A continuous supply of Si precursor leads to the formation of NW with an Au-Si droplet on the top of the wire [43,45,46].

Hiruma et al. in 1990 [47] applied the same procedure previously employed for Si NWs to grow III–V SC NWs. They also used Au nanoparticles to growth these III–V NWs via a VLS-like mechanism.

In general, for the growth of III-V NWs, several different metal particles have been explored so far such as Au, Ag, Cu, Ni, and Sn [43]. However, Au is used widely because it offers many promising properties such as, formation of low melting alloys with group-III materials, high diffusion coefficient, and resistance to oxidation [48]. There are several ways to form Au nanoparticles on the substrate: deposition of an Au thin film, drop-casting of Au colloidal solutions, and electron beam lithographic patterning [49]. The first two methods are most commonly used due to simple procedure protocol and cost-effectiveness. The main target of these methods is to control the density and size of Au nanoparticles. The use of nanoparticles formed by Au thin film annealing is widely used. With this method, a thin film of Au is deposited on the substrate and annealing is carried out at a high temperature, which gives Au nanoparticles as a consequence of dewetting process. The size of the nanoparticles is controlled by the initial film thickness, the dewetting temperature and the time of annealing. However, the main limitation with this method is that it gives a large Au nanoparticle diameter distribution, which results in a large NW diameter distribution. In case of Au colloidals, the nanoparticles are deposited directly on the substrate. This method provides controllability over diameter of NWs because it gives a very narrow dispersion in NW diameter. The selection of these methods fully depends on the desired characteristic of NWs [49].

1.3.2 Self-catalyzed and catalyst-free growth methods

Despites the impressive progress and results reported so far with Au-seeded NW growth, this method presents some limitations. In fact, Au is not compatible with

current Si-based semiconductor technology, as it creates deep levels in the Si band gap which can act as carrier traps that might degrade the properties of the devices [43,48,50,51]. Moreover, it is quite challenging to grow axial heterostructured NWs with sharp interfaces when there is an interchange in the group III elements, because of the reservoir effect or memory effect associated with the incorporation of group III material into the nanoparticle even after the group III flux is turned off. In addition, the Au-assisted method does also not provide an ideal platform for core-shell (CS) NW growth due to undesired axial growth of NWs as well as kinking [52-54]. To overcome all these issues, alternative growth methods were introduced such as catalyst-free and self-catalyzed.

The self-catalyzed growth is similar to the VLS growth but the droplet is composed of an element of the NW instead of a foreign metal [48]. Mostly group III elements served as a catalyst due to their low melting point and the ability to form liquid droplets. For example, in the self-catalyzed growth of GaAs NWs Ga droplets act as catalyst [48] while in the case of self-catalyzed InAs NWs the In species are employed as a catalyst [50]. With this method, the catalyst droplet is obtained on the substrate by in-situ pre-deposition of group III elements or by carrying the growth under group III rich condition [48,50,51,55]. The NW growth then starts when also the group V precursor is introduced. The liquid droplet on the tip of NWs allows growing NWs in VLS growth mode in a near-equilibrium condition [55-59]. Examples of self-catalyzed GaAs and InAs NWs grow on Si substrates are shown in Fig. 1.2.

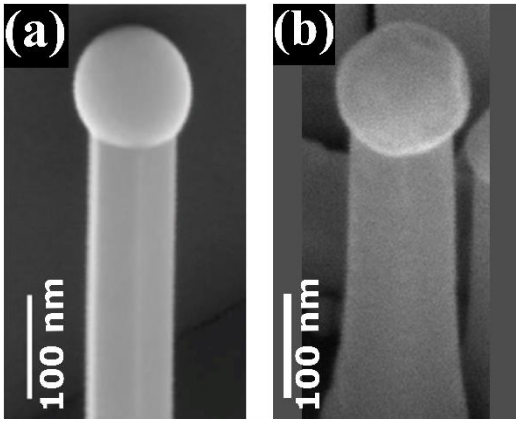

Figure 1.2. (a) Self-catalyzed GaAs NW grown directly on Si (111) by MBE. The figure is adopted from Ref. [60] (b) Self-catalyzed InAs NW grown directly on Si (111) by CBE. The figure is adopted from Ref. [55].

However, the self-catalyzed growth requires a careful optimization of growth conditions such as growth temperature and group V/III ratio. Many groups have

investigated the effect of growth temperature on the growth of In-catalyzed InAs NWs. Radial and axial growth rates of NWs showed monotonic behaviour as described by Anyebe et al. [61]. The axial growth of In-catalyzed InAs NWs is limited by group V flow at optimal growth temperature [55,61,62], while radial growth of self-catalyzed InAs NWs is limited by group III flow and it increases linearly with group III flux at optimal growth temperature [55,61,62].

In addition to the possibility to grow high-quality structures free from foreign elements, another advantage of the self-catalyzed growth is the possibility to alter the size or volume of the catalyst particle dynamically during the growth. The variation in size of the catalyst is directly linked to the contact angle of particle and diameter of NWs. The simple modification of the catalyst size also gives a way to control axial and radial growth. The axial growth of NWs can be stopped by the complete consumption of nanodroplets and the radial growth starts. Furthermore, axial growth can be reassumed again by redepositing the droplet on the tip of NWs. As has been demonstrated, such growth protocol gives a large degree of freedom to grow a different kind of axial and radial heterostructures [51].

An alternative method is the catalyst-free growth that is also known as vapor-solid (VS) or self-induced method and it does not involve any catalyst particle. VS depends on the imbalance of crystal growth velocities as a function of crystallographic orientations [51]. In the VS method, the growth starts by islands that are formed on the substrate and evolve into NWs due to lattice-mismatch between substrate and grown material such as for example InAs NWs on Si substrates [51]. However, the self-assembled method requires pre-treatment of substrates to control the nucleation sites and different approaches have been proposed. The growth of catalyst-free NWs is obtained by employing thin oxides deposited on the substrate and without oxide. Koblmüller et al. demonstrated the growth of InAs NWs on sputtered SiO_2 thin films on Si substrates that were subsequently etched down to a thickness between 2.5 nm and 6 nm [63]. Rieger et al. studied the growth of InAs NWs on Si substrates by the VS process by using different thicknesses of the oxide layer deposited on Si substrates by chemical oxidation method via hydrogen peroxide solution [64]. Gomes et al. reported that the deposition of SiO_2 by an RF magnetron sputtering introduced some surface defects that acted as nucleation sites for the growth of catalyst-free NWs [65]. The pre-treatment process of the substrates plays an important role in controlling the

density of NWs with respect to the parasitic islands [64,65]. An example of self-assembled growth of InAs NWs by the catalyst-free method is shown in Fig. 1.3.

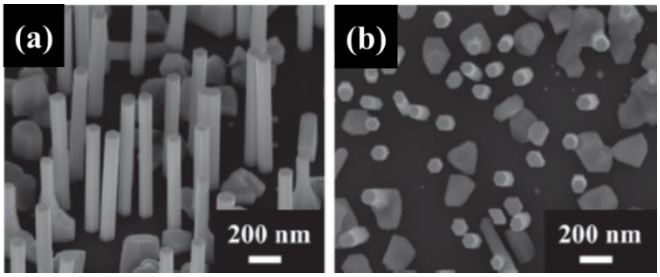

Figure 1.3. (a) 45° tilted SEM image of catalyst-free InAs NWs grown on Si (111) (b) Top view SEM image clearly reveals the presence of parasitic islands co-existing with InAs NWs. Images are adopted from Ref. [66].

1.4 Nanowire heterostructures

Heterostructures (HSs) are combinations of different materials. They are serving as the key component of most SC devices. Since materials have different lattice parameters, strain fields could arise by combining lattice-mismatched materials in the epitaxial thin-film growth. The NWs instead provide a new platform to form heterostructures with high crystalline quality because strain energy is accommodated due to high surface to volume ratio of NWs. The HS in NWs can be of two types: axial and radial. In the case of axial HS NWs, the material is varied along the growth axis during the growth of NWs. In the case of radial HS NWs, after growing the core of the NWs, a coaxial radial shell (core-shell (CS)) of material is formed around the core [67], so the composition changes perpendicularly to the growth axis.

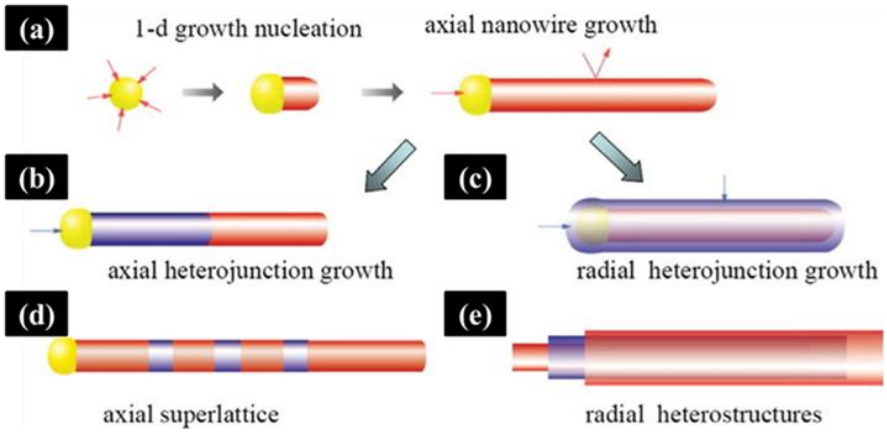

Figure 1.4. Schematic diagram of metal catalyzed NWs and HS NWs. (a) NW growth through catalyst-assisted axial growth. (b,d) The switching of the source material results in axial HS NW and superlattices. (c, e) Conformal deposition of different materials leads to the formation of core shell and core-multishell radial HS NW. Adopted from Ref. [68].

A schematic illustration of axial and radial HS NWs is shown in Fig. 1.4. In literature, several examples of defect-free III-V axial and radial HS NWs are reported, such as InAs-InSb, GaAs-GaSb, InAs-GaSb, GaAs-InAs, GaAs-InGaAs, InP-InGaP, GaP-InGaP, and InAsP-InP [43].

1.4.1 Bandgap engineering

The main idea of the employment of HSs is that they provide precise control over the location and motion of the charge carriers in SC. When different materials combine to form an HS their bandgap alignments change. The type of band alignments is divided according to the relative arrangement of band edge energies [69]. SC HSs exhibit three types of band gap alignments, type-I (straddling gap), type-II (staggered gap), and type-III (broken gap). The alignment of the bands depends on the material type. The three bandgap alignments are schematically illustrated in Fig. 1.5.

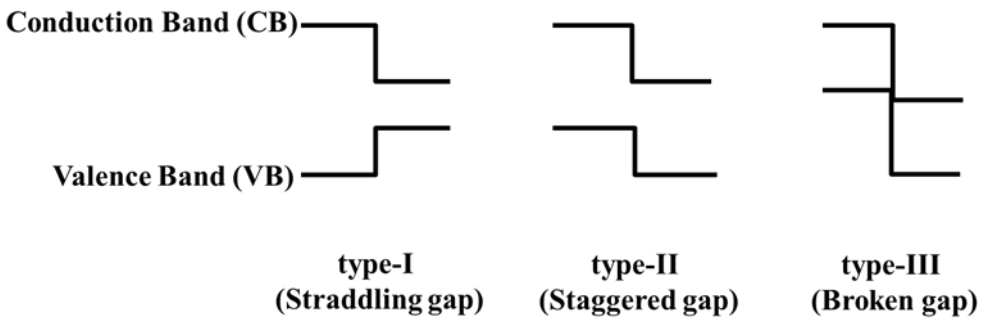

Figure 1.5. Three different types of band alignment in SC HS.

In type-I alignment, both electrons and holes are confined in the SC material with the lower band gap. It is the most commonly observed band gap alignment in III-V SC. Typical examples of type I alignment are GaAs/AlGaAs and GaAs/InAs HSs [70,71]. A type II alignment is also known as a spatially indirect band gap in which electrons are confined in one material and holes in the other material. InAs/AlSb and InP/$In_{0.52}Al_{0.48}As$ HSs are well known examples of type II alignment [69]. In case of NWs, type II alignment can also be realized in the same type of NWs having alternating zincblende (ZB) and wurtzite (WZ) crystal structures such as InAs, InP, and GaAs [72-76]. A type III alignment is also called a zero-gap system. For example, InAs/GaSb and InAs/InSb HSs exhibit type III broken band alignments [35,42].

1.4.2 Strain properties of NWs

The growth of radial HS NWs with lattice-mismatched materials develops strain fields inside the structure similarly to the case of thin films. The strain value correlates with the thickness of the growing material and after a certain thickness the strain energy starts to be released through the development of defects inside the structure. This thickness is known as critical thickness. In order to explain the strain relaxation in radial HS NWs a continuum elastic theory has been used [77]. Several models have been introduced to explain the strain properties in HS NWs. The strain energy tensor is calculated by the displacement field which is related to the local variation of lattice constants. In the case of radial HS NWs, the core material acts as substrate and the shell as a grown material. A coherency limit exists between core and shell materials, which is closely related to the lattice-mismatch between core and shell material, the diameter of the core and the shell thickness [78].

Several experimental techniques have been used to measure the strain relaxation of HS NWs such as HR-TEM analysis with geometric phase analysis (GPA), X-ray diffraction (XRD) and XRD reciprocal space mapping [79,80-82]. Among them, HR-TEM with the combination of GPA maps is the most suitable technique to study the strain properties of a single HS NW thanks to the higher spatial resolution.

Figure 1.6 panels (a,b) shows a radial HS NWs of InAs/GaSb, in which a core of InAs is surrounded by a shell of GaSb [79]. The NWs were grown by MBE on Si (111) substrates. The authors reported a pseudomorphic growth of a 40 nm thick GaSb shell around a 100 nm thick InAs core without the formation of misfit dislocations while in the case of planar films strain relaxation starts to occur when GaSb layer thickness exceeds 20 nm. Other examples of radial HS NWs are present in literature: Treu et al. reported that the critical thickness of the InP shell for InAs/In(As)P CS NWs is below 10 nm with an InAs core diameter of 75 nm while above it starts to relax producing dislocations [80]. Yuan et al. reported strain analysis of $GaAs_{1-x}Sb_x$/InP CS NWs by HRTEM and GPA maps [82]. They found that the interface between core and shell is very sharp. The core of $GaAs_{0.56}Sb_{0.44}$ has a hexagonal shape with {110} side facets while the InP shell has a triangular cross-section with {112}A polar side facets. No dislocations were observed by HRTEM and GPA mapping, which indicates a coherent growth of the InP shell. This is reasonable because with 44% Sb content there is only 0.4% lattice-mismatch between the core and the shell. The authors have also exploited the same type of CS NWs with less Sb content ($GaAs_{0.71}Sb_{0.29}$) The

theoretical critical thickness with 1.5% lattice-mismatch is about 30 nm while InP shell thickness in this sample is 12 nm. Therefore, a coherent interface exists between core and shell and the InP shell is under compressive strain but no dislocations are found.

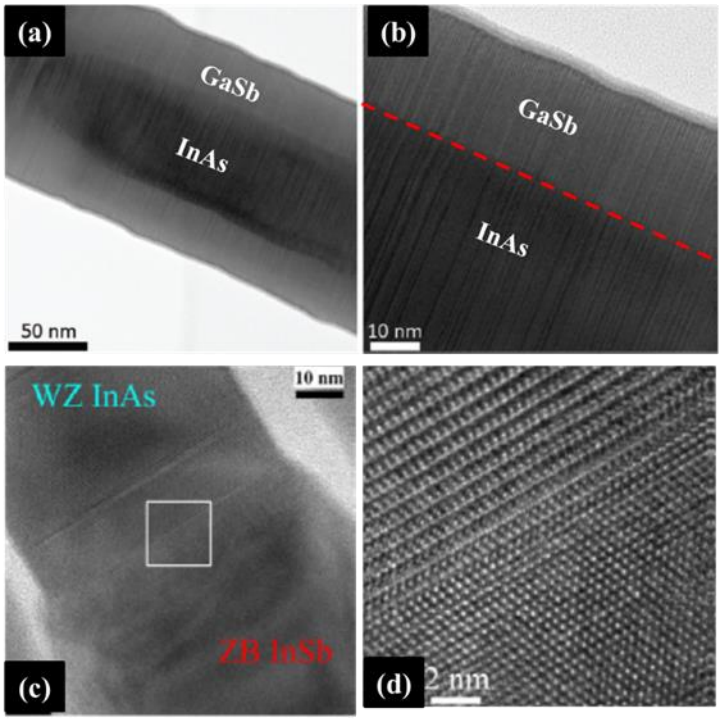

Figure 1.6. Example of radial and axial HS NWs: (a,b) High-resolution transmission electron microscopy (HR-TEM) images of InAs/GaSb CS NW, adopted from Ref. [79]. (c,d) TEM study of the interfacial region between InAs and InSb segments of axial HS NWs, adopted from Ref. [83].

Figure 1.6 (c,d) is an example of an axial HS NW, where the axial HS is formed along the InAs/InSb NW [83]. Axial HS NWs are achieved by changing the group V precursor from As to Sb during the CBE growth of the NWs. A very sharp interface is observed between InAs and InSb axial junction with few stacking faults in the InAs segment, while the InSb segment is defect-free. The lattice-mismatch between InAs and InSb is 7% [83], and the strain energy is elastically relaxed within a few nanometers from the InAs/InSb interface without plastic relaxation due to the NW geometry.

Therefore, the investigation of strain relaxation mechanisms and critical shell thickness in HS NWs is an important and fundamental step towards the fabrication of high-performance devices with high-quality HS NWs. As a result, a detailed study of strain relaxation mechanisms in case of InAs/InP/GaAsSb core-dual-shell (CDS) NWs will be described in chapter 3.

1.5 Crystal structure of III-V semiconductor NWs

According to literature, mostly III-V SCs in the bulk form are found in a stable ZB crystal structure with the exception of III-nitride compounds, which show WZ crystal structure. Instead, SC NWs can be realized in both ZB and WZ crystal structures or in a mixture of ZB and WZ [84]. The ZB crystal structure is a face-centered cubic crystal system and the unit cell consists of two face-centered cubic crystals that they have an offset of two different atoms to each basis point. Since all sides of a cubic unit cell are equal, the ZB crystal structure has only one lattice constant. WZ is a hexagonal close-packed structure composed of two hexagonal unit cells with an offset of two different atoms to each basis point. The WZ unit cell is defined by a straight parallelepiped with an equilateral rhombus at the base. Therefore, two lattice constants are required to define the WZ unit cell, one lattice constant defines the base of the rhombus and the second one defines the height of the unit cell. Both crystal structures form by tetrahedral bonds between the atoms as shown in Fig. 1.7. The energetic difference between these two crystal phases appears from the third nearest-neighbour atomic spacing, which is smallest for WZ as compared to ZB. The corresponding stacking sequence of WZ and ZB along the <111> directions is displayed in Fig. 1.7 [45,84].

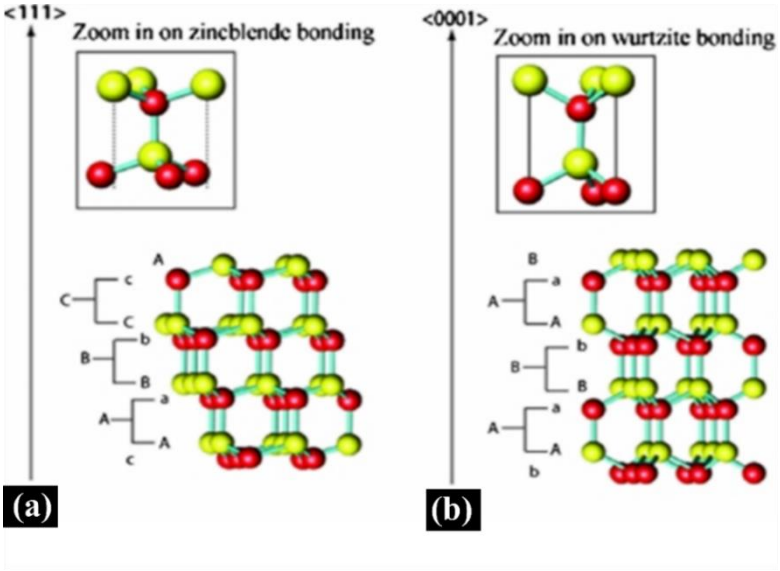

Figure 1.7. Stacking sequence in ZB (a) and WZ (b), respectively, crystal structures in the <-110> viewing direction. Different atom colours display the two types of atoms (groups III and V), while upper and lowercase letters indicate layers of these two atom types. The insets show zoomed-in views of the bonding configuration in the ZB and WZ crystal structures. Images adopted from Ref. [84].

Typically, NW growth occurs in the direction perpendicular to the close-packed planes in the crystal structure which is the <111>B crystal direction for the ZB structure and the <0001>B crystal direction for the WZ structure [84]. NWs are grown in a layer-by-layer fashion in close-packed planes, and crystals are made of a bilayer, and each bilayer consist of III-V pairs of atoms. Both WZ and ZB crystal structures are quite similar along the <111> crystallographic direction, and the only difference between them is the stacking sequence of bilayers A, B, C of III-V atom pairs as shown in Fig. 1.7. For the ZB crystal phase, the repeated stacking sequence of three distinct bilayers defines as ABCABC…. along the crystal <111> directions. While the WZ phase consists of a stacking sequence of two distinct bilayers described as ABAB… along the <0001> crystal direction. A small change in the stacking sequence of layers leads to defects or changes in the crystal structure. This change in the crystal structure has a significant impact on the properties of the NWs [45,84], such as different band gaps for WZ and ZB phases.

Therefore, a good control over the crystal structure of NWs is essential for the realisation of NW-based electronic and optoelectronic devices. The parameters that can influence the crystal structure are growth temperature, flux, V/III ratio, and NW diameter, growth direction, catalyst particle size, and contact angle. The predominant crystal structure of InAs and InP NWs is WZ, while for InSb and GaSb NWs it is ZB [84].

For example, the crystal structure of InAs NWs strongly depends on the NW diameter, i.e. for small diameters they show a WZ crystal structure while for large NW diameters they exhibit a ZB crystal structure. It has been observed that in the case of InP NWs, V/III ratio and the growth temperature can control the crystal structure. Lower V/III ratio and lower growth temperature give ZB crystal structure while higher V/III ratio and higher growth temperature give WZ crystal structure. The predominant existence of WZ phase in this material is linked with lower surface or edge energy [84]. In contrast to InAs and InP NWs, the Sb-based NWs usually show pure ZB crystal structure. The high quality of ZB crystal structure in Sb-based NWs is mainly connected to the low ionicity of the group III to Sb bonds. The Sb-based materials have smallest ionic bonds and, therefore are more stable with ZB phase as compared to WZ phase [85].

1.6 Motivation and challenges

1.6.1 InAs/InP/GaAsSb core-dual-shell NWs

Transistors are fundamental building blocks of electronic devices. Many efforts have been done over the past years in downscaling and miniaturization of metal-oxide-semiconductor (MOS) FETs by using III-V SC NWs. The NW geometry provides promising surrounding gate architecture, which enables to enhance the ON-state current under a lower applied voltage as well as reduced OFF-state leakage current as compared to conventional Si-based metal-oxide-semiconductor FETs [86]. The use of a CS NW geometry in a transistor architecture allows a promising path to manage the drive current issue without compromising neither chip area nor device electrostatics [28]. Currently, tunnel FET (TFET) have been considered as one of the top candidates for future low power devices [27,28]. III-V SC materials and in particular, InAs/GaSb CS NWs have been intensively studied for the last ten years and they are considered as best candidates for TFETs due to excellent properties such as narrow and broken band gap alignment, minimum tunnelling barrier, and high tunnelling probability [27,43]. The InAs/GaSb based TFET improved the on-state current by reducing the tunneling barrier thickness. Moreover, the best performance TFET device up to now is made of InAs/InGaAsSb/GaSb, which exhibits a higher on-state current [43].

Furthermore, InAs/GaSb CS NWs provide tuneable broken bandgap alignment as a function of source-drain voltage, back-gate voltage and by field effect modulation which creates a new pathway to explore broken-gap systems and band-to-band tunnelling in Esaki diodes [87,88] as well as to the study of spin-orbit interaction [89,90]. In addition, InAs/GaSb CS NWs could open an interesting way to fundamental studies on Coulomb drag phenomena in low dimension [91] as well as to novel schemes for the detection of indirect excitons [92]. For this purpose, we introduced a thin InP barrier between InAs core and GaSb shell to electrically insulate n-type and p-type conduction in the InAs core and the GaSb shell, respectively. We selected InP as barrier because of its small lattice mismatch and large bandgap compared to both InAs and GaSb. According to the strain study specified above, it is quite interesting to see the effect of InP barrier thickness on the quality of the heterointerfaces, bandgap alignment, and strain properties. Therefore, the complete study of growth mechanisms, strain properties, quality of heterointerfaces, device

fabrication, and electrical transport of these NWs has been conducted and is described in detail in chapters 3 and 4.

1.6.2 NW-based quantum dots

Quantum dots (QDs) are zero-dimensional nanostructures with a typical lateral size of the order of 10 nm, and therefore the charge carriers are confined in all three directions. So far, several types of QD NWs were grown and investigated both electrically and optically, such as AlGaAs/GaAs [93], GaAsP/GaAs [94], GaP/GaAsP [95], InP/InAsP [96], InAs/InP [97], ZnSe/CdSe [98], GaN/AlN [99].

InAs/InSb QDs are attractive systems with peculiar properties that can be employed for various applications such as mid-IR range optoelectronic devices [100,101], gas sensors [102], quantum computation spintronic, and high-speed electronics [103]. Also, the InAsSb alloy provides a narrowest tuneable bandgap for most of the infrared spectrum range which would broaden applications of Sb-based semiconductors. Consequently, they can be used for high quality mid and long wavelength infrared emission and detection devices, especially in environmental gas detectors, and security [104-107].

From the last decade, a lot of effort is made on the growth of InSb and InAsSb QD materials by self-assembled methods [100-102,108-114]. The growth of InSb and InAsSb QDs is very challenging on commonly available semiconductor substrates due to a large lattice mismatch as well as Sb segregation and surfactant effects [111,112]. To the best of our knowledge defect-free growth of InSb QDs on InAs and silicon substrates have not been achieved yet [115]. Different approaches have been reported for different types of substrates by introducing an intermediate layer of different material between the substrate and InAs/InSb in order to reduce lattice mismatch [102,111] leading to very difficult growth protocol [100,102,111]. Moreover, due to the large lattice mismatch between InAs and InSb the critical thickness value is very small [114]. All these challenges could be solved by using NW architecture.

Consequently, in this study we explored for the first-time successfully the growth of InSb QD embedded in InAs nanowires in self-catalyzed regime. We adopted the self-catalyzed growth method over the commonly used Au-assisted growth method because this growth method provides more control over growth dynamics of InAs/InSb QDs in terms of morphology. The growth mechanisms and dynamics of this system is

a completely new area of study and it has not been reported before. Hence, a systematic study of growth parameters is performed in order to achieve optimized morphology of InSb QD and to study growth mechanisms and dynamics involved. This investigation could be useful in the development of Sb-based materials for the application of optoelectronic devices operating in the middle infrared range. Therefore, a complete study of growth mechanisms, morphological, and structural properties has been conducted and it is described in chapter 6.

1.7 Scope and outline of this thesis

The main objective of this thesis is to develop new strategies with the required appropriate choice of growth parameters to realize radial InAs/InP/GaAsSb and axial InAs/InSb NWs in catalyst free and self-catalyzed growth regimes. The growth is performed by chemical beam epitaxy on Si substrates and the growth mechanisms are studied by tuning the growth parameters and conditions. Detailed morphological, structural, and compositional analyses of the grown NWs, as well as evaluation of the electrical properties have been performed.

The outline of this thesis is:

- The growth method and characterization techniques used in this thesis are briefly explained in Chapter 2.
- In chapter 3, the growth mechanisms of InAs/InP/GaAsSb CDS NWs are described and a complete strain relaxation mechanism is discussed.
- Chapter 4 is dedicated to the investigation of the transport properties of InAs/InP/GaAsSb CDS NWs with different InP barrier thicknesses.
- In chapter 5, a detailed investigation of the impact of the growth parameters on self-catalyzed InAs/InSb axial NWs is presented and explained with a dedicated theoretical model.
- In chapter 6, the growth of self-catalyzed InSb/InAs QD NWs is presented with a complete morphological and structural characterization.
- In chapter 7, a summary of the achieved results together with their future perspectives is described.

Chapter 2: Experimental methods

2.1 Introduction

In this chapter, a description of the experimental techniques and methods employed for substrate preparation, NW growth and their characterization is presented. Chemical beam epitaxy (CBE) has been used for the growth of semiconductor NWs and scanning electron microscopy (SEM) for the morphological studies of grown NWs. The chemical composition of NWs was studied by energy-dispersive X-ray spectroscopy (EDX) and structural analyses were probed by high resolution transmission electron microscopy (HR-TEM). In this chapter, I will describe briefly all these techniques.

2.2 Substrate preparation

In this work, all NWs have been grown on Si (111) substrates. In order to carry the catalyst-free or self-catalyzed growth of nanowires, Si (111) substrates have been covered with 20 nm thick silicon dioxide (SiO_2) film. To do this end, in the first step, the two-inch Si (111) wafer was etched with buffered oxide etching (BOE) solution for 2 min to remove the native oxide and rinsed in deionized water for 1 min. Afterward, the Si wafer was immediately transferred to radio frequency (RF) magnetron sputtering unit and pumped for 1 hour to obtain a chamber pressure of 9×10^{-6} Torr. Argon gas was used to obtain ionized energetic particles with Ar flow = 50 sccm. The sputtering process is controlled by sputtering DC bias and time. In all the substrates, the SiO_2 layer was deposited with optimized DC biased of 400 V for 80 sec to achieve 20 nm thick SiO_2 film. Prior to start the growth, the sputtered SiO_2 layer was removed with BOE and the etched substrate was immediately transferred to CBE system. This procedure (SiO_2 sputtering and etching) is fundamental for the catalyst-free NW growth. Indeed, during the sputtering process, the high energetic ions create some kind of surface defects, which act as nucleation sites for the NWs growth [65]. At the same time, the SiO_2 removal ensures the epitaxial growth of uniformly oriented InAs NWs [66].

2.3 Chemical beam epitaxy

Chemical beam epitaxy is one of the most important techniques for the epitaxial growth of III-V semiconductor materials. It is an ultrahigh vacuum (UHV) deposition technique. The other most commonly used techniques for the epitaxial growth are metalorganic chemical vapor deposition (MOCVD) and molecular beam epitaxy (MBE). Both techniques have some advantages and disadvantages. For example, in MBE the growth is performed in ultrahigh vacuum environment that allows to grow high purity materials with very low impurity incorporation and extremely low growth rates. This ensures a precise control over doping and compositional profiles of the growing material, at single atomic layer level. However, in MBE elemental solid sources are used located inside the chamber, so the vacuum of the system has to be broken for the source refilling and it takes several days to reach again ultrahigh vacuum level. Moreover, it is hard to grow alloy semiconductors with more than two group V elements or with abrupt change of the beam fluxes. On the other hand, in MOCVD the growth is conducted at moderate or reduced pressure and metalorganic (MO) gaseous precursors are used. These sources can be continuously supplied with controlled and tuneable fluxes into the reactor, allowing a very high flexibility in material combination. However, in MOCVD the growth involves chemical reactions, and not only physical absorption of the precursors. Furthermore, the growth rate is generally higher, so it is more difficult to grow high quality ultrathin films with monolayer control and pure composition [116]. The advantages of both MOCVD and MBE techniques are merged in CBE systems. All the sources of group III and V elements are in a gaseous form derived from the MO precursors, but the growth is carried in a UHV environment similar to MBE system. The beam nature of the sources in CBE allows a very high flexibility in combining different material and precursor fluxes. Due to UHV growth chamber, the mean-free paths between molecular collisions become longer compare to source inlet and substrate distance and gas transport turn into collision-free. At the same time, the UHV environment and the low growth rates allow to grow semiconductor materials and heterostructures with monolayer thickness control same as in MBE [117,118]. In a typical CBE growth procedure, first, the substrate is heated some hundreds of degrees, depending upon the type of growth, and the precursors of group III and V elements are supplied through the gas-lines into the UHV growth chamber. The precursors of group V such as tertiarybutylarsine (TBAs) and tertiarybutylphosphine (TBP) are pre-cracked in injectors at 1000 °C, while for

the group III elements, like trimethylindium and triethylgallium, the substrate temperature is sufficient to pyrolysis them. The molecules strike on the hot surface of the substrate through chemical beam and group III and V atoms incorporate to form very slowly and systematically ultra-thin layers. The CBE system used to grow the NWs presented in this thesis is a Riber Compact-21 as shown in Fig 2.1.

The CBE system consists of three chambers connected with each other through gate vales and have its own pumping system. The first one is a load-lock chamber, which allows us to load and unload the samples. The load-lock chamber is pumped by a turbo-molecular pump and typical pressure is 10^{-8} Torr achieve in 1-2 hours. The In bounded substrates mounted on molybdenum plates carry through cassette from load-lock chamber to next chamber by opening the gate valve. The second chamber is the preparation chamber. This chamber is pumped with an ion pump and its typical pressure is 10^{-10} Torr. It also contains a heating stage to degas or remove contaminations form the substrates before entering the growth chamber.

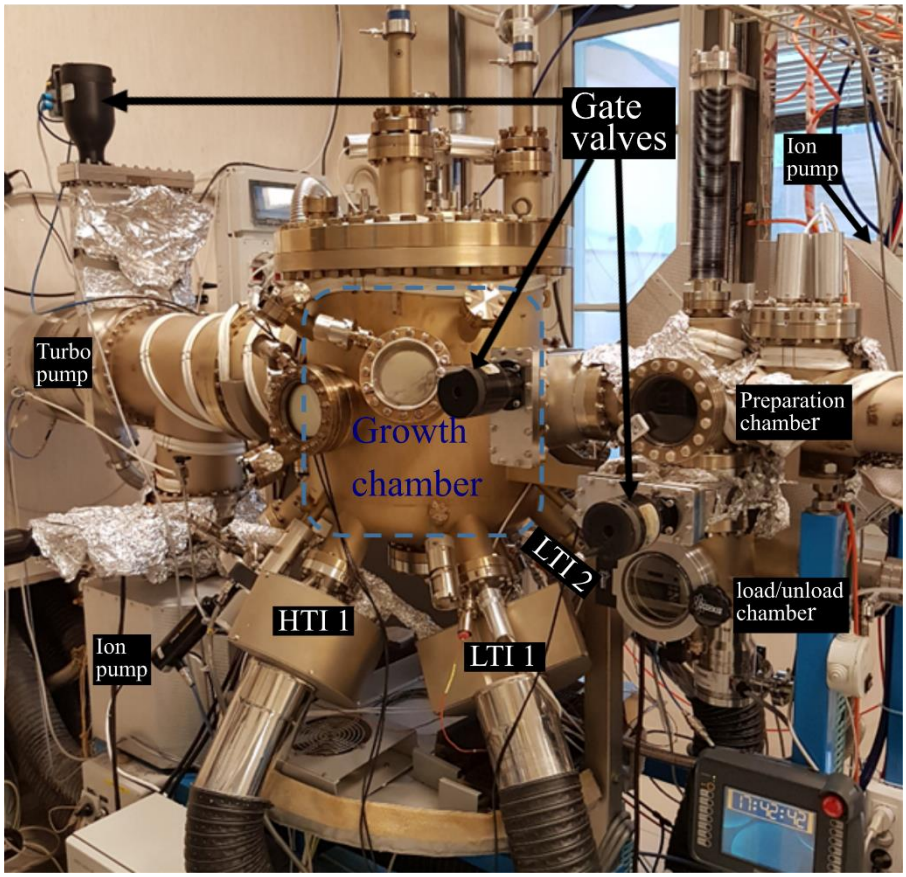

Figure 2.1. An image of Riber Compact-21 CBE system located at NEST laboratory Pisa. Three chambers with corresponding parts are highlighted.

The third is a growth chamber, which is pumped with turbo molecular and ion pump to achieve base pressure around 10^{-10} Torr. The chamber is a UHV stainless-steel chamber surrounded by a cryopanel filled with liquid nitrogen in order to keep pressure low inside the growth chamber by surface trapping of contaminations and residual gases on the wall. It is also equipped with a quadrupole mass spectrometer or residual gas analyser that allows to monitor the background composition and to evaluate the level of water, oxygen, nitrogen, and other contaminants by determining the atomic weights of the chemical elements. The CBE system is equipped also with electron gun and fluorescent screen for in situ reflection high-energy electron diffraction (RHEED) to study surface reconstruction during the growth. The sample is moved from preparation chamber to the growth chamber with a magnetic rod (fork). The substrate temperature is controlled by a thermocouple which is located above the substrates holder and accurate temperature measurements are performed by an optical pyrometer. During the growth process the pressure of the chamber reaches 10^{-6} to 10^{-5} Torr.

Our CBE system contains the following MO precursors for group III: trimethylindium (TMIn), triethylgallium (TEGa) and trimethylaluminum (TMAl) and for group V: tertiarybutylarsine (TBAs), tertiarybutylphosphine (TBP), trimethylantimony (TMSb), tris(dimethylamino)antimony (TDMASb). The ditertiarybutyl selenide (DtBSe) precursor is used as a source for n-type doping. The MO sources are stored in stainless-steel bottles in the gas cabinet room. These precursors are carried from bottles to the gas injectors through dedicated gas lines pumped by turbo pump through a vent and run valves configurations. The CBE system is equipped with different types of injectors: two low temperature and two high temperature gas injectors. TMIn, TEGa, TMAl, TDMASb and DtBSe precursors are provided with low temperature gas injectors operating at 50 °C. In fact, for these MO precursors, the elements are derived by pyrolysis directly on the substrate surface. On the other hand, TBP, TBAs and TMSb precursors need to be pre-cracked in the high temperature gas injectors operated at 1000 °C. In front of each gas injector, a shutter allows rapid interruption and resumption of beam fluxes. The precursors flow is controlled by the vent and run valves. The fluxes are prepared in vent mode before entering into the growth chamber and then switched to the run mode configuration. Before the gases are switched to either the vent or run mode, they pass a needle valve

and a baratron manometer. The input line pressure value is used as a set point for the pressure control unit, which adjusts the needle valve to reach the set value and keep it constant. The precursor fluxes are directly proportional to the line pressures. Therefore, by using run mode, the beam fluxes enter the growth chamber and the growth process starts by simultaneously opening group III and V precursors. The beam of group III and V molecules strikes directly on the heated substrate and adatoms start to incorporate into appropriate lattice sites. Several processes occurred on substrate surface such as diffusion, adsorption, desorption and incorporation of adatoms. At the end, when the growth process finishes remaining gases inside the growth chamber and lines are pumped and collected in dry scrubber to remove hazardous gases.

2.4 Scanning electron microscopy

The scanning electron microscopy (SEM) is one of the most widespread techniques for the morphological study and analyses of micro to nano structures in the field of material science. SEM produces three dimensional image of a sample by scanning it with a focused beam of electrons. The electron beam is produced in an electron gun by thermionic or field emission. For the acceleration of electrons, a high potential difference is applied between the cathode and anode. The electron beam is focused on the specimen surface with the help of three electromagnetic lenses. When primary beam touches the sample surface, it generates different kinds of signals such as secondary and back scattered electrons, Auger electrons and X-rays photons and cathodoluminescence as shown by the Fig. 2.2 [119]. Then these signals are collected by suitable detectors and converted into an electric signal. One of these signals is made of secondary electrons, which are a result of inelastic interactions between the electron beam and the sample and they are low energy electrons. They escaped from few nano-meters of surface of the sample. The signal generated from secondary electrons is used to form images of sample surface.

This characterization technique is very useful to study the morphology of grown NWs. Samples are generally mounted on sample holder with a conductive adhesive such as carbon tape and must be grounded to avoid the accumulation of electrical charge. Insulator samples are made conductive by a deposition of a thin conducting layer. In our case, there is no need of sample preparation for SEM imaging because as grown array of NWs can be directly imaged due to their semiconducting nature as well as grown semiconductor substrates. Top-view imaging was performed in order to

collect information about areal density, homogeneity, and kinking of NWs. 45°-tilted SEM images were used to measure diameter and length of NWs, and morphology of 2D and island growth.

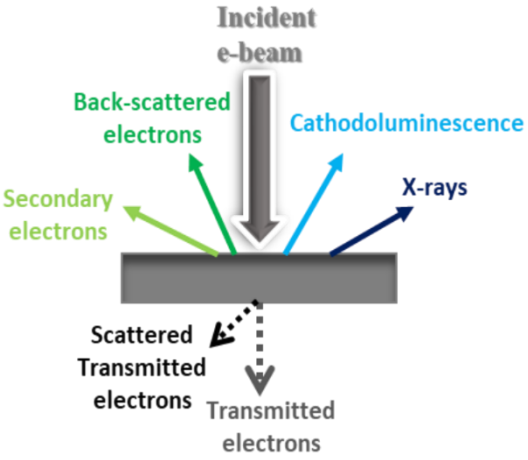

Figure 2.2. Different kind of signals produced by interaction of electron beam with the sample, which provide information, related to the morphology, chemical composition, and optical properties of the sample.

In the present work, Zeiss MERLIN and Zeiss Ultra Plus field emission SEM were used operated at 5 keV. The SEM Zeiss MERLIN is equipped with a GEMINI II column, a process chamber with a 5-axes motorized stage (X, Y, Z, tilt, and rotation) and a semi-automatic airlock. The stage and specimen surface are located at the eucentric point, which means that all rotation axes intersect the same point. This assured that the focus is maintained when the specimen is tilted at a certain working distance. We can get very high resolution of 0.8 nm. A Zeiss MERLIN SEM installed in the NEST laboratory is shown in Fig. 2.3.

Figure 2.3. An image of Zeiss MERLIN SEM located at NEST laboratory in Pisa.

2.5 Transmission electron microscopy

Transmission electron microscopy (TEM) is a very powerful tool for structural, morphological, and chemical composition analysis of nanomaterials. It is a microscopy technique in which a high energetic beam of electrons shines into a very thin specimen and it is transmitted through the specimen. An image is generated from the interaction of transmitted electrons. The image formation depends upon several image modes such as bright-field (BF), dark-field (DF) and high resolution (HR) TEM modes. Since electrons used in TEM measurements have high energy this allows the TEM to capture very fine information even as small as a single column of atoms. Different kind of information is collected by using various detectors such as backscattered and secondary electron detectors, electron energy loss and X-ray detectors, bright field and dark field transmitted electron detectors. Consequently, it gives detail on the crystal structure, quality and size of different kinds of materials, structural defects, grain boundaries, dislocations, strain and chemical compositions of different materials [119].

Over the past few years, another extraordinary feature of HR-TEM is scanning TEM (STEM) mode that has become a valuable tool for the characterization of nanostructures. The STEM operates on the similarly way of normal SEM: the electron beam is focused in a spot over the specimen and the desired signal is collected to generate an image. A BF detector is placed below the sample to collect transmitted beam while an annular DF (ADF) detector collects scattered electrons through small angles and a high angle ADF (HAADF) detector gathers electrons scattered at higher angles. Each detector gives a unique and compactable view of specimens. HAADF images are produced to as Z-contrast images because the contrast relates to the atomic number Z of the chemical element [120].

The STEM mode is also useful to obtain a spatially distributed chemical composition of the specimen with EDX. The focused electron beam is incident on the sample and the X-ray spectrum is measured by an energy dispersive spectrometer. This spectrum is a fingerprint of each chemical element and its analysis gives the chemical composition of the sample.

In the present work, the crystal structure, the elemental composition, and the chemical phase distribution of NWs were measured with a JEOL JEM-2200FS microscope operated at 200 keV, equipped with an in-column Ω filter and a detector

for X-ray energy-dispersive spectroscopy. Imaging was performed either in HR-TEM mode combined with zero-loss energy filtering or scanning (STEM) mode using a high-angle annular dark-field (HAADF) detector yielding atomic-number (Z) contrast. For TEM observation, the NWs were mechanically transferred onto carbon-coated copper grids.

2.5.1 Focused ion beam

Focused ion beam (FIB) has become the most popular and demanding technique in the semiconductor industry. It was developed at the University of Chicago and at the Oregon Graduate Institute in the 1970s. It is used for the surface modification of materials, bottom-up and top-down approach for the material fabrication, for the etching of materials and for the preparation of structural cross-sections [120,121]. This technique is also used for the sample preparation for the TEM analysis because for TEM measurements the sample should be very thin (50-100 nm). A FIB system consists of three main parts: a source of ions, an optical column of ions, and a sample displacement table. The basic working principle of FIB is similar to SEM but instead of an electron beam, an ion beam is used. A focused ion beam is fixed and the stage is moved in various positions in a high vacuum environment. The ion column is joined with the high vacuum chamber. A Ga liquid metal ion source (LMIS) is typically used in FIB because of the low melting point and a low vapor pressure [120,122]. The ion column is equipped with all the required elements for the acceleration, focusing and deflection of ion beam. The ions are accelerated and focused through electrostatic lenses to obtain focused beam. As displayed in Fig. 2.4, the Ga ion beam (primary beam) strikes on the surface of the sample and a small amount of sputtered particles of material as well as neutral ions or secondary ions and also secondary electrons leave the sample surface. The sputtered particles enable local removal of material from the sample surface. These particles are further processed or collected through different kind of detectors to give various information about the sample and they are used for FIB imaging, etching, deposition, sample preparations for SEM and TEM and tomography.

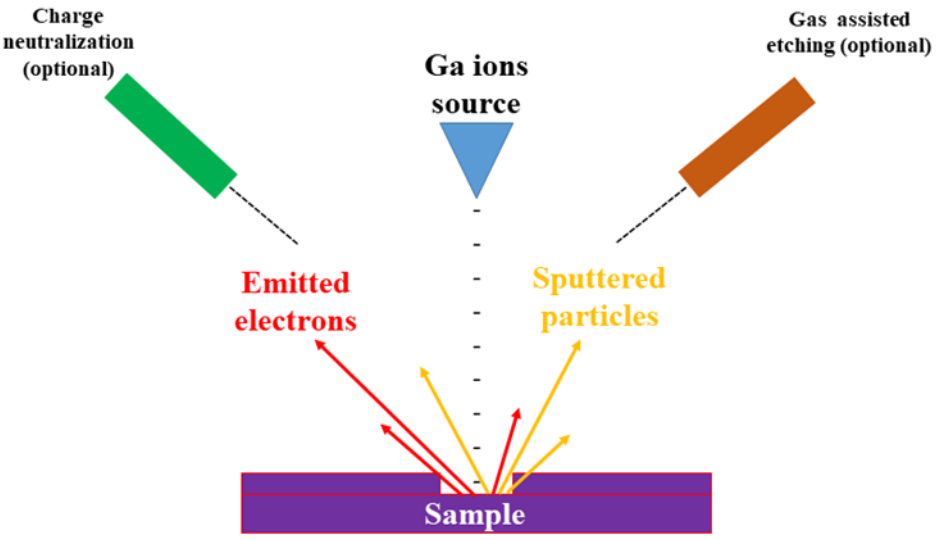

Figure 2.4. Schematic illustration of basic principle of FIB technique.

FIB is the most commonly used technique for the preparation of TEM samples. The lamellae of semiconductor material can be formed 10-15 µm wide, 8-10 µm deep, and 50-100 nm thick within the area of interest for example to examine specific defects at the interface between different materials [122]. Prior to the FIB process, the surface of sample is polished with conducting material such as carbon or gold material. The next important step is the deposition of protection layer of platinum or tungsten on area of interest. The ion beam of a FIB is scanned over the sample surface and an area of interest is located with the help of secondary ions or electrons: the progress of sputtering process is observed by acquiring secondary electron images of the sample by tilting it and the thickness of sample is measured. The process is carried out to get the final required sample thickness.

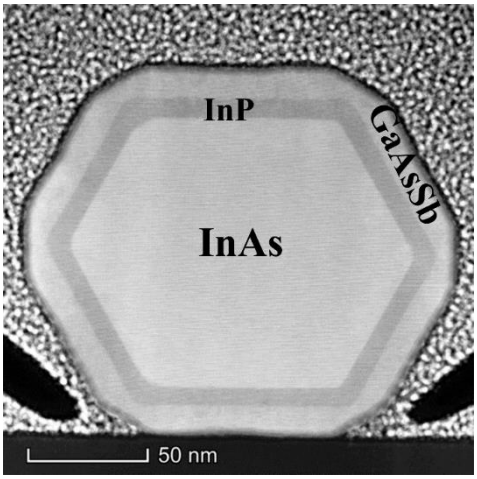

Figure 2.5. A STEM image of lamella of InAs/InP/GaAsSb CDS NW prepared using FIB technique.

In this work, cross-sectional lamellae of InAs/InP/GaAsSb CDS NWs were prepared by FIB (FEI-Helios 650) at the university of Beijing with a Pt deposited protection layer by transferring as-grown NWs onto a suitable substrate. These lamellae are useful to study structural properties at InAs/InP and InP/GaAsSb interfaces such as defects, dislocations, interface roughness and strain. An example of typical prepared lamella of InAs/InP/GaAsSb CDS NW is shown in Fig. 2.5.

2.5.2 Geometric phase analysis

Geometric phase analysis (GPA) is a method used in HR-TEM to quantify the local lattice displacements and strain field of crystalline materials with the nanoscale resolution. This method was first reported by Hytch et al. in 1998 [123]. The basic algorithm of this method is related to the Fourier transform of HR-TEM images. The Bragg reflections (BR) are obtained from Fourier transmission. These BR spots represent the two-dimensional (2D) unit cell of the corresponding crystal structure of HR-TEM image. A sharp BR spot gives perfect crystal while diffused BR spot represents variation in lattice planes of the crystal. An image is formed by choosing these two BR reflection spots, which help to determine the local variation of the corresponding crystal structure. The local variation is obtained by an image in a 2D color map format. An image of perfect crystal is defined by Fourier sum as:

$$\boldsymbol{I(r) = \Sigma_g\, H_g\, exp\, exp\, \{2\pi i g.r\}} \tag{2.1}$$

Where I(r) is defined as the intensity at position r and g is reciprocal lattice vector of corresponding to the BRs of the lattice. The Fourier component H_g is written as $H_g = A_g exp\{iP_g\}$, here A_g represent the amplitude of lattice fringes and P_g is the phase. After insertion of H_g relation the equation 2.1 can be written in term of amplitude and phase of corresponding lattice fringes or reciprocal lattice vector g,

$$\boldsymbol{I(r) = A_0 + \Sigma_{g>0} 2A_g\, cos\, cos\, \{2\pi g.r + P_g\}} \tag{2.2}$$

The image of the corresponding particular set of BR fringes $B_g(r)$ is written as,

$$\boldsymbol{B_g(r) = 2A_g\, cos\, cos\, \{2\pi g.r + P_g\}} \tag{2.3}$$

To convert this equation in the image format by GPA, one BR has to be filtered from the Fast Fourier Transform (FFT) image and perform the inverse FFT. In other word, the equation 2.3 represent the image, which would be obtained by Bragg filtering of original image by placing a mask around the positions ±g in the Fourier transform.

The images can be generated by considering both the phase and amplitude of images. The displacement field is extracted from the components of the phase image in the direction of two non collinear reciprocal lattice vectors. Strain maps are calculated by taking derivative of displacement field U_i, (i = x,y) that is $\varepsilon_{ij} = \frac{dU_i}{dj}$ [123].

In our case GPA maps of InAs/InP/GaAsSb CDS NWs were performed by using STEM_Cell software [124] in order to quantify the strain field at InAs/InP and InP/GaAsSb heterointerfaces as well as to directly observe dislocations. Figure 2.6 panel (a) shows STEM image of InAs/InP/GaAsSb CDS NW along {110} side walls of the NW. The corresponding FFT image is displayed in panel (b). Two FFT spots are selected as indicated by green and red rectangles. The resultant phase and amplitude image obtained by inverse FFT is shown in Fig. 2.6 (c). In order to observe variation in a lattice, 2D strain maps can be formed by choosing InAs as the reference and measuring the lattice variation in the other phases (InP and GaAsSb). The corresponding GPA maps of ε_{xx} (i.e. variation of the interplanar spacing in the <112> direction, parallel to the interface) and ε_{yy} (i.e. variation of the interplanar spacing in the <110> direction, perpendicular to the interface) are displayed in Fig. 2.6 panel (d) and (e), respectively.

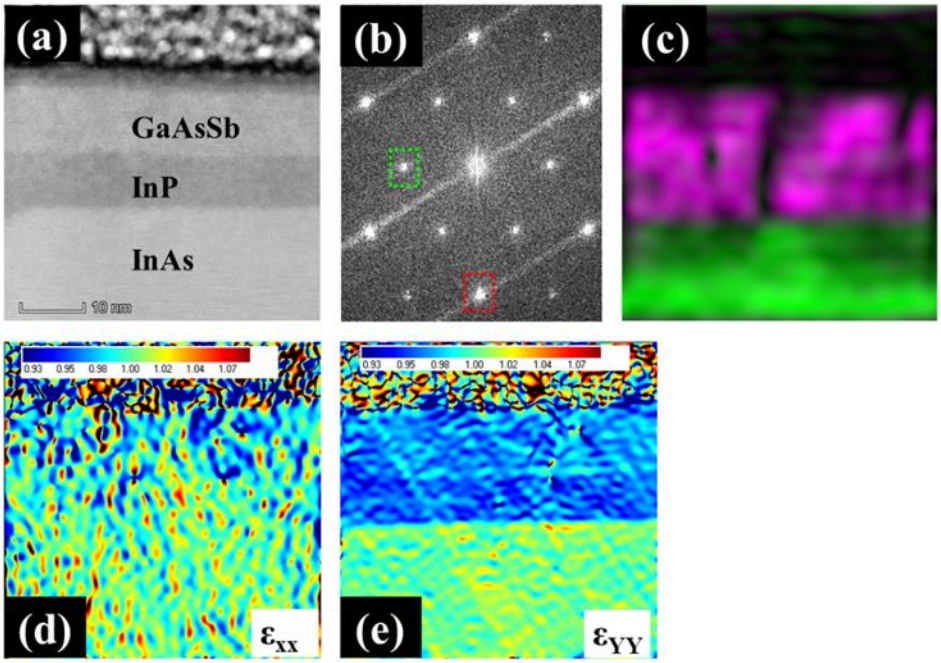

Figure 2.6. Procedure to perform GPA analysis: (a) a STEM image of InAs/InP/GaAsSb CDS NW at the {110} side walls. (b) The FFT micrograph of image in panel (a). (c) Phase and amplitude image obtained by applying inverse FFT. (d)-(e) Strain maps ε_{xx} and ε_{yy}, respectively.

2.6 Summary

In this chapter, we briefly described the experimental techniques and methods employed in this work. The first part of the chapter was mainly dedicated to experimental techniques such as the RF-Magnetron sputtering, which we have used for substrate preparation, and to the chemical beam epitaxy (CBE) technique, which was employed for the growth of semiconductor NWs. In the second part of the chapter, we described the techniques that have been employed for the characterization of the grown NWs. Scanning Electron Microscopy (SEM) measurements were performed for the morphological investigation of grown NWs. Moreover, the chemical composition of NWs was determined by energy-dispersive X-ray spectroscopy (EDX), while the structural analyses were performed by high-resolution transmission electron microscopy (HR-TEM). Furthermore, by combining the scanning transmission electron microscopy (STEM)-Moiré technique with geometric phase analysis, we studied the residual strain and the relaxation mechanisms in the core-dual shell NWs.

Chapter 3: Growth protocol and strain relaxation mechanisms of InAs/InP/GaAsSb core-dual-shell NWs

3.1 Introduction

Over the past few years, CS NWs become major topic of research because radial geometry can improve the performance and/or add new properties in NW-based devices [53,125]. For example, surface passivation by the introduction of one or more shells around the core can enhance the radiative emission efficiency reducing the carrier surface recombination [126]. So far, many CS NWs based on III-V semiconductors were demonstrated, among them, InAs/GaSb CS NWs attracted great attention because of their peculiar properties such as InAs and GaSb have very small effective masses with high electron and hole mobility, respectively, type-III broken gap band alignment [87], and a very low lattice mismatch of 0.6% [127]. All these properties make InAs/GaSb CS NWs suitable for applications in devices like tunnel field effect transistors [128], Esaki diodes [87], frequency multipliers [126], and for fundamental studies on spin states [129] and electron-hole hybridization [89]. Indeed, electronic devices fabricated with these heterostructures implement radial interface between n-type and p-type conductors, and can display negative differential resistance owing to transport across the broken-gap junction [87]. Furthermore, interesting electronic device configurations can be achieved if the carriers are separated in two channels, i.e. in the InAs core and GaSb shell, respectively. To this end, in the present work we inserted thin InP barriers of different thickness in between InAs core and GaSb shell. We choose InP as barrier material because of its small lattice mismatch with InAs and GaSb, and its larger band gap compared to both InAs and GaSb. The InP barrier will provide a separation of the carriers in two distinct channels, i.e. electrons in the InAs core and holes in the GaSb shell and it will allow to realize novel electronic devices.

It is well known that electronic and optical properties of semiconductor heterostructures are affected by the presence of strain fields arising from lattice

mismatch between the combined materials [130,131]. Pseudomorphic growth of NWs in a CS geometry implies a coherency limit in the core diameter and the shell thickness that depend on the lattice mismatch between the two materials [77,78,132]. For a given NW core diameter, the shell material will grow coherently strained only below a critical thickness, while above this it is energetically favoured to produce misfit dislocations that degrade device performance [133]. Therefore, it is clear that a fundamental step towards the fabrication of high performance devices with HS NWs is the investigation of strain relaxation mechanisms and critical shell dimensions.

The first section of this chapter we will discuss the growth of catalyst-free InAs, InAs/InP and InAs/GaAsSb CS NWs by employing different growth parameters in order to obtain homogenous and smooth InAs/InP/GaAsSb CDS NWs. The second section of this chapter is focused on the study of strain relaxation mechanisms of InAs/InP/GaAsSb CDS NWs as a function of the InP shell thickness. The transmission electron microscopy measurements were performed in collaboration with Francesca Rossi (IMEM-CNR, Parma, Italy) and Ang Li (Beijing Key Laboratory of Microstructure and Properties of Solids, Beijing University of Technology, Beijing, China). The results presented in this chapter are published in Ref. [134].

3.2 Growth protocol of InAs core NWs

The growth of catalyst-free InAs NWs was carried on Si (111) substrates. First, 20 nm thick silicon dioxide (SiO_2) film was deposited by sputtering on silicon substrates. More details on the effect of sputtering parameters and thickness of SiO_2 are reported in Ref. [65]. Before mounting, the substrates inside the growth chamber, they are etched in (BOE solution for 2 min to remove SiO_2 and rinsed in water for 1 min. The substrate is mounted with indium on a molybdenum plate and immediately transferred into an introduction chamber. Then the substrate is mounted into the CBE growth chamber and hydrogen-terminated Si (111) substrate is annealed at 700 ± 5 °C under TBAs line pressure of 1 Torr for 15 min. The annealing step under As flux is crucial to obtain As-terminated surface and to convert the Si (1×1)-H surface to Si (1×1)-As [65,86,135-137]. The As-terminated surface is the best surface for growing polar semiconductors on non-polar substrates and to obtain perpendicular NWs on Si (111) substrate [86,137]. After completing the annealing step, the temperature was ramp down to 300 ± 5 °C. The growth of catalyst-free InAs NWs consists of two steps.

The first step is called low temperature (LT) growth step and the second is high temperature (HT) growth step.

3.2.1 LT growth step

The LT growth is performed for 10 min at 300 ± 5 °C with a line pressure of TBAs = 3 Torr, TMIn = 0.3 Torr and then growth temperature ramp up to 430 ± 5 °C in 10 min while keeping the same line pressure of group III and V. The LT step is important for the nucleation of NWs, which helps in avoiding thermal desorption of In from the surface. The resulting objects obtained after this LT step are shown in Fig. 3.1. We can easily observe that on the substrate two types of objects are present, one has irregular shape and the second has hexagonal cross sections as shown on top view SEM micrograph of Fig. 3.1 panel (a). The morphology is clearer from 45° tilted SEM image of Fig. 3.1 (b), crystals elongated perpendicular to substrates are NWs while irregular objects are islands. After the LT step, the average length and diameter of InAs NWs are 120 ± 10 nm and 20 ± 3 nm, respectively.

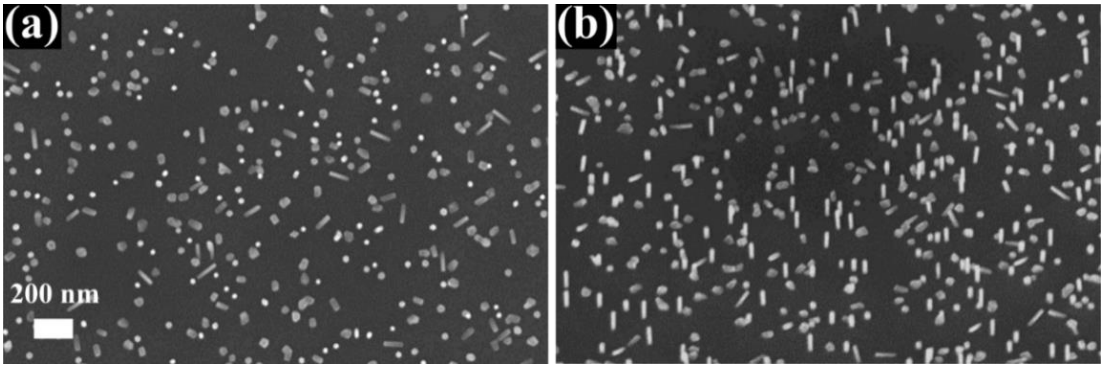

Figure 3.1. (a)-(b) SEM images of the resulting objects obtained after the LT growth: top view (left) and 45° tilted (right) image. The scale bar is the same in both images.

The density and the number of islands and NWs are investigated in Ref. [65] where the formation of nano-objects is explained in terms of formation of surface defects induced by bombardment of high energetic sputtered ions which act as nucleation points for the NW growth. The density of nucleation objects strongly depends on sputtering parameters [65].

It is also observed that temperature of LT growth step can influence the density of islands and NWs. We have investigated the LT growth step at three different growth temperatures, 280 ± 5 °C, 300 ± 5 °C, and 340 ± 5 °C. The corresponding SEM images are shown in Fig. 3.2. We can realize from Fig. 3.2 panel (a) that 280 ± 5 °C is more favorable to grow islands and average length and diameter of NWs at this temperature

are 60 ± 10 nm and 20 ± 5 nm, respectively. It is seemed that 340 ± 5 °C is instead a very high temperature for the growth because both islands and NWs start to desorb as displayed in panel (c). The average length and diameter of NWs at this stage are 100 ± 10 nm and 30 ± 5 nm, respectively. Therefore, the optimized temperature is 300 ± 5 °C, where high density of NWs and reduced island density are present on the substrate. The average length and diameter of the InAs NWs measured from panel (b) are 120 ± 10 nm and 20 ± 3 nm, respectively.

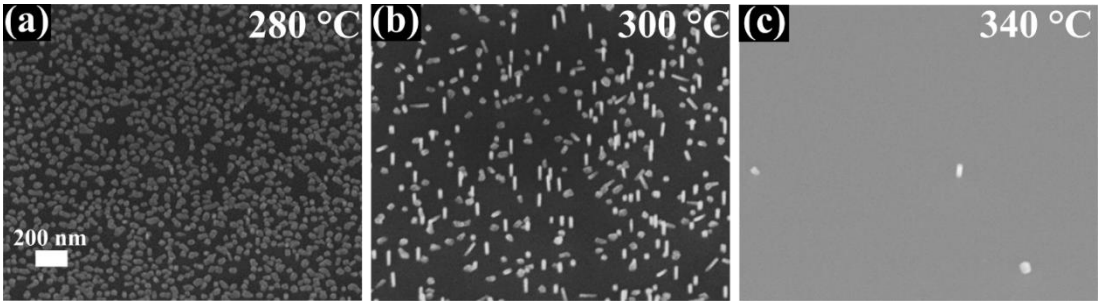

Figure 3.2. (a)-(c) 45° tilted SEM images of catalyst-free InAs NWs: images at the end of LT growth step on different LT. The scale bar is the same in all the images.

3.2.2 HT growth step

The HT growth step has strong influence on the morphology of InAs NWs with respect of the length and diameter of NWs. The HT growth is performed for 60 min with a line pressure of TBAs = 3 Torr, TMIn = 0.3 Torr and the growth temperature is varied from 390 ± 5 °C to 450 ± 5 °C. The SEM images of the resulting InAs NWs are displayed in Fig. 3.3 panels (a)-(d). We measured almost 50 NWs on each sample to extract the average length and diameter values. It is found that when the HT growth is 390 ± 5 °C, the average length and diameter of the InAs NWs are 495 ± 60 nm and 86 ± 5 nm, respectively. Then further increment in growth temperature to 410 ± 5 °C leads to an average length and diameter of 585 ± 70 nm and 75 ± 4 nm, respectively. We have found that increasing further the growth temperature to 430 ± 5 °C the InAs NWs have maximum average length and diameter of 950 ± 70 nm and 69 ± 3 nm, respectively. When the temperature is further increased to 450 ± 5 °C, the InAs NWs start to desorb and the resulting average length and diameter of InAs NWs are 800 ± 80 nm and 80 ± 4 nm, respectively. From this study we can conclude that 430 ± 5 °C is the optimal temperature to achieve a high aspect ratio (length/diameter) of InAs NWs. In Table 3.1, we summarized all the statistical morphological information of InAs NWs at different HT.

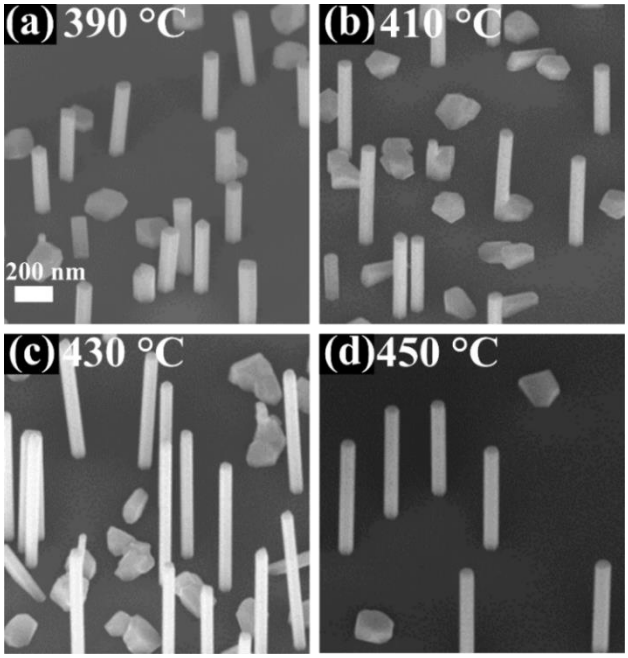

Figure 3.3. (a)-(d) 45° tilted SEM images of catalyst-free InAs NWs: InAs NWs at the end of HT growth step at different HT. The scale bar is same in all the images.

Table 3.1: The influence of HT temperature on the morphology of InAs NWs is summarized.

HT Growth	**Length (nm)**	**Diameter (nm)**	**Aspect Ratio (L/D)**
390 ± 5 °C	495 ± 60	86 ± 5 nm	5.7 ± 0.8
410 ± 5 °C	585 ± 70	75 ± 4 nm	7.8 ± 0.95
430 ± 5 °C	950 ± 70	69 ± 3 nm	13.7 ± 1.1
450 ± 5 °C	800 ± 80	80 ± 4 nm	10 ± 1.1

The observed behavior of length and diameter of grown InAs NWs versus HT temperature could be explained by considering different mechanisms. In general, the growth of NWs occurs by considering the following mechanisms: (1) direct impingement of adatoms on the metal-particle, (2) collection of adatoms from the side walls of NWs, and (3) collection of adatoms from the substrate and diffuse on side wall. Since in our case we do not have any particle or droplet on the top of NWs so we can neglect first growth mechanism. When we increased the temperature, the diffusion length of In adatoms is enhanced and then the probability of In adatoms to reach the tip of the NWs as compared to sidewall is enhanced and they are contributing to axial

growth. The NW length increased to a maximum at 430 ± 5 °C, while diameter decreased. Similar results were reported previously in Refs. [61,63,66,138,139]. The resulting NWs after two-hour growth time grown at 430 ± 5 °C are showed in Fig. 3.4.

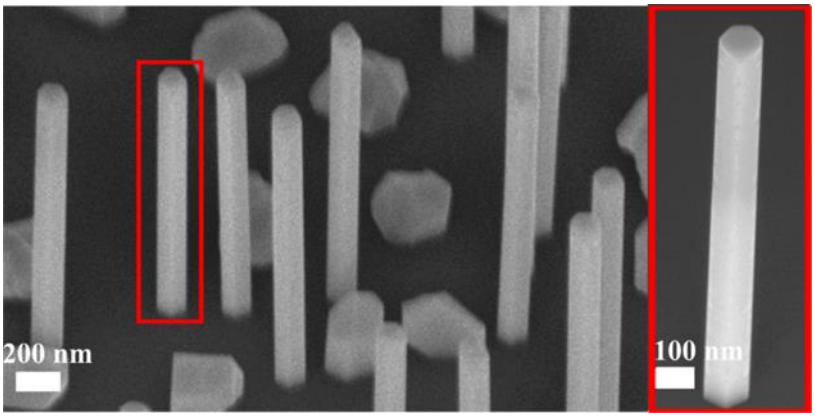

Figure 3.4. The 45° tilted-view SEM image of InAs NWs obtained after two-hour growth. The red box displayed a magnified image of the respective highlighted NW.

The average length and diameter are 1.5 ± 0.1 μm and 130 ± 5 nm, respectively. The InAs NWs have a hexagonal cross-section with a flat top facet parallel to the (111) substrate surface. The tilted-view SEM image shows that the NWs do not exhibit detectable tapering displaying a uniform diameter along the entire length as shown in red rectangular box of Fig. 3.4.

3.3 Study of InAs/InP core-shell NWs

After achieving InAs core NWs with maximum aspect ratio, we have investigated the impact of the growth parameters on the growth of InAs/InP CS NWs. First, we studied the influence of growth temperature and then the effect of line pressures on the morphology of InAs/InP CS NWs.

3.3.1 Growth temperature

In order to investigate the influence of the growth temperature on the InP shell, we grew a series of samples in which all other parameters (line pressure ratio of TMIn/TBP 0.3/1.0 and growth time 15 min) were kept constant. Figure 3.5 (a)-(c) shows the InAs/InP radial heterostructured NWs obtained at different growth temperatures. The InP shell grown at 360 ± 5 °C (panel a) shows very rough sidewalls and the top facet is not flat showing an irregular cross-section. By increasing the growth temperature to 370 ± 5 °C (panel b), we found InAs/InP NWs with regular hexagonal cross-section, smoother sidewalls, and flat top facet. A further increase of

the growth temperature to 380 ± 5 °C (panel c) gives NWs with still smooth sidewalls, but larger axial InP growth, resulting in a visible InP top segment.

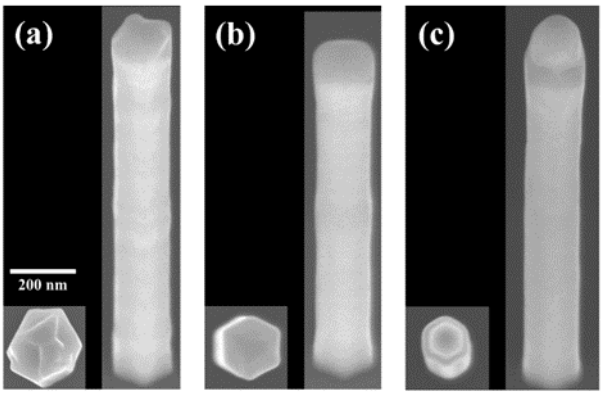

Figure 3.5. (a)-(c) SEM images of catalyst-free InAs/InP CS NWs: Insets and 45°-tilted images of InAs/InP CS NWs growth at different shell growth temperatures as shown from left to right panels: (a) 360 ± 5 °C, (b) 370 ± 5 °C, and (c) 380 ± 5 °C. Scale bar is the same in all panels: 200 nm. Inset: from the top-view images, the hexagonal cross-sections of all NWs are clearly visible.

In order to quantify the thickness of the InP shell and axial segment grown on the InAs NW we acquired EDX compositional maps like the one shown in Fig. 3.6 (a)-(c) for 10 NWs at each growth temperature and from the axial and radial line scans we determined the average values reported in Fig. 3.6 (f).

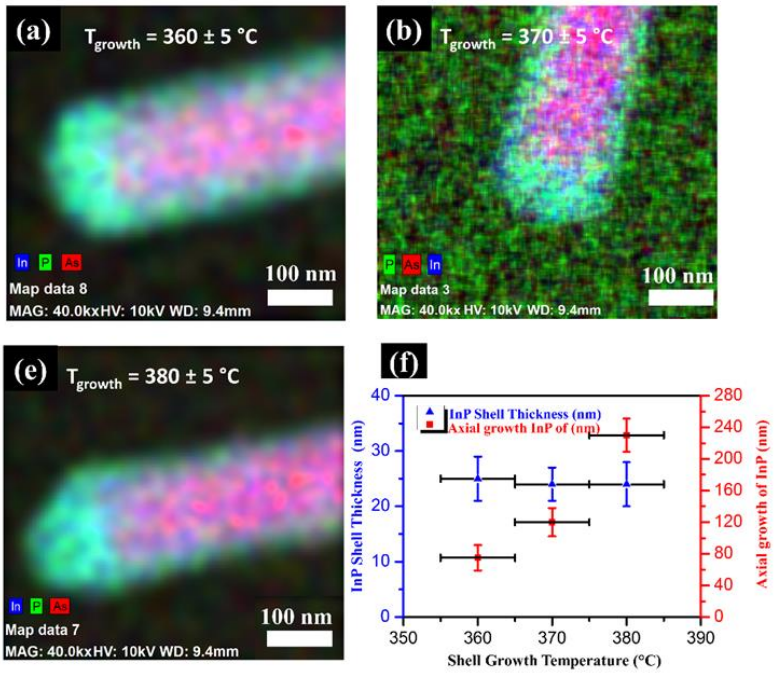

Figure 3.6. (a)-(c) EDX maps of the upper portion of the InAs/InP CS NWs displayed in figure 3.5 grown at different InP shell growth temperatures indicated in the panels: (a) 360 ± 5 °C, (b) 370 ± 5 °C, and (c) 380 ± 5 °C. (f) Plot of InP radial and axial growth versus InP shell growth temperature. The axial and radial InP thickness were measured by EDX line scans.

Data show that the radial growth rate of InP shell is constant in this range of growth temperature explored, while the axial growth rate of InP increases linearly with the growth temperature. This increased axial growth rate stems from the higher kinetic energy of the In adatoms on the NW sidewalls at higher temperatures: they can more efficiently reach the top facet of the NW and contribute to the axial growth. Based on this analysis we selected 370 ± 5 °C as the optimal growth temperature since it is high enough to provide an InP shell with smooth sidewalls, on the other hand, it is low enough to keep a low InP axial growth rate.

3.3.2 Influence of metal-organic line pressures

Using the optimal growth temperature of 370 ± 5 °C, the effect of group III/V line pressure ratio such as TMIn/TBP 0.3/1.0 (sample A) and TMIn/TBP 0.3/0.70 (sample B) were investigated for InAs/InP CS NWs by keeping the constant growth time to 15 min. The corresponding observed results are shown in Fig. 3.7. The results shown in Fig. 3.7 revealed that by decreasing TBP flux from 1 Torr to 0.7 Torr a droplet is formed on top of NWs as shown in panel (b), while in case of higher TBP flux (1 Torr) no particle is observed.

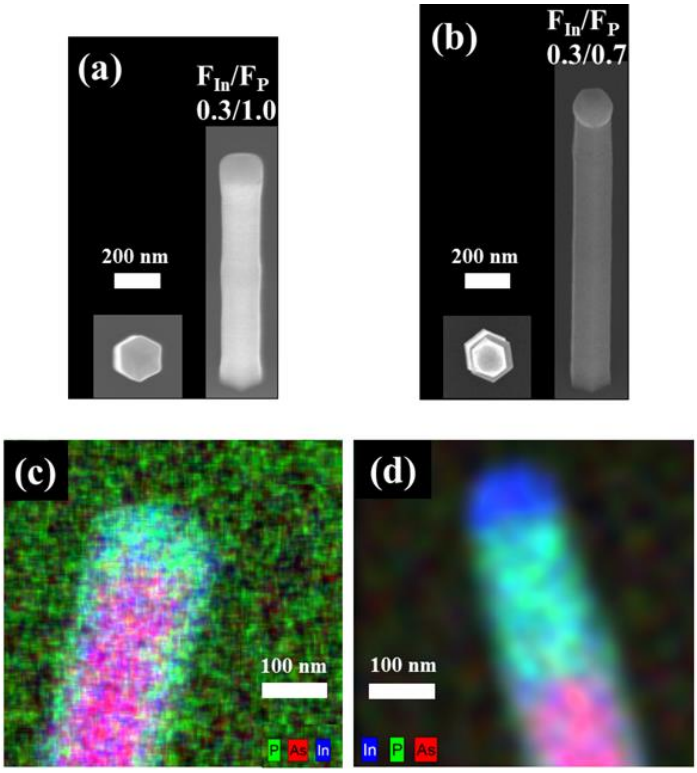

Figure 3.7. (a)-(b) SEM images of InAs/InP CS NWs: top view (Insets) and 45°-tilted images obtained after 15 min of InP shell growth at a fixed In of 0.3 Torr and different P as indicated in the panels. (c)-(d) EDX maps of the upper portion of the InAs/InP CS NWs as displayed in panel (a)-(b).

We have found by the EDX analysis that the nanoparticle on the top of the NW is purely In droplet as shown in panel (d). The formation of In droplet on the top of the NWs must be due to In-rich conditions during the growth of InP, as it was also observed for In catalyzed InAs and Ga-catalyzed GaAs NWs [55,140]. With low P flux probably the growth mechanism changed from VS to VLS growth mode. The measured average of axial and radial thickness of InP from EDX line scan profiles are 120 ± 18 nm and 24 ± 3 nm for sample A (high P flux) and 225 ± 20 nm and 18 ± 4 nm for sample B (low P flux), respectively. Therefore, we can conclude that in the VLS growth mode the axial rate is higher while the radial growth rate is reduced [35,140,141]. The catalyst-free growth approach is more suitable in order to achieve CDS growth because radial growth is enhanced with respect to axial growth.

3.3.3 Crystal structure analysis

Figure 3.8 (a) shows the HR-TEM image acquired in [110] zone axis of a representative InAs/InP CS NW with the InP shell grown at the optimized temperature (370 ± 5 °C) for 3 minutes. Several defects such as stacking faults and twin perpendicular to the growth axis are visible in both InAs core and InP shell. It is known that the crystal structure of InAs NWs obtained by catalyst-free VS growth is a mixture of zinc blende and wurtzite segments, so that the NWs have several stacking faults perpendicular to the growth direction [66] and such defects propagate in the InP shell. The interface between the two materials is visible in the HR-TEM image (highlighted with the red lines).

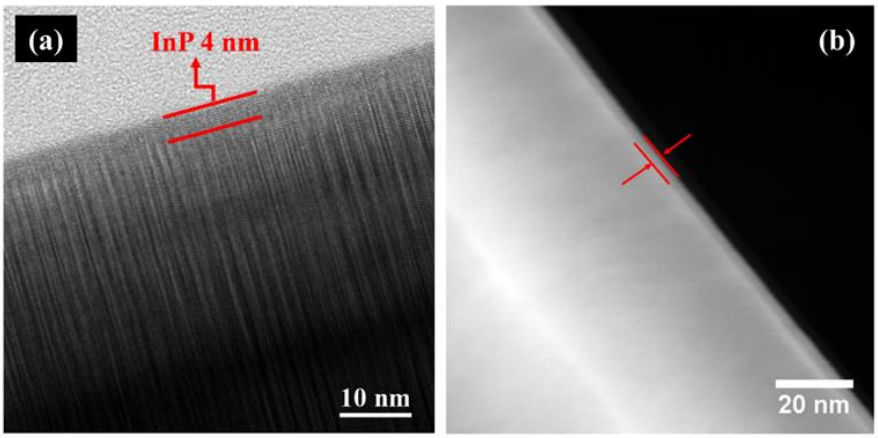

Figure 3.8. (a) Bright field HR-TEM image, acquired in [110] zone axis, of an InAs/InP core shell NW. The red lines indicate the InP shell. (b) STEM-HAADF image, acquired in [112] zone axis, of a NW from the same sample confirming the smooth and homogenously thick (4 nm) InP shell around the InAs core.

We measured the shell thickness of more than 10 NWs at different positions along the growth axis and we found an average InP thickness of 4.0 ± 0.5 nm (see a representative STEM-HAADF image in Fig. 3.8 (b)), accordingly with what expected from the growth rate. We could not evaluate the chemical composition of this very thin shell from EDX analysis because the P signal is very low and the atomic % quantification can be misleading. A more accurate EDX analysis, allowing the precise element quantification, is performed in cross-sectional lamellae of the final CDS NWs, as it will be shown later.

3.4 InAs/GaAsSb core-shell NWs

In order to optimize the growth of a GaSb shell with the best morphology, we first investigated GaSb growth directly around the InAs NWs (without InP) at 370 ± 5 °C (with same optimal temperature of the InP shell) using different precursor line pressures, keeping the same III/V ratio, previously optimized [87]. The best results in terms of growth rate were obtained by using 0.5 Torr and 0.43 Torr of TEGa and TMSb line pressures, respectively. Some incorporation of As is present in the GaSb shell due to background As present inside the growth chamber. Figure 3.9 shows the InAs/GaAsSb CS NWs obtained after 90 min of GaSb growth. Panel (a) shows a representative STEM-HAADF image of a single NW, aligned along the [112] zone axis. The STEM analysis of various NWs confirms the presence of a shell with uniform thickness all along the growth axis for the whole NW length, around the InAs core. Panels (b) and (c) show the EDX analysis of the same NW depicted in Fig. 3.9 (a), performed by using the Kα emissions of Ga and As, and the Lα emissions of In and Sb. The EDX composition map shown in panel (b) clearly shows the presence of a GaAsSb shell of 17 ± 1 nm thickness around the core as indicated with green color. The shell growth rate is therefore 0.21 ± 0.01 nm/min. The growth rate is very low probably because of the low fluxes and growth temperature selected in order to ensure homogenous and smooth sidewalls.

Panel (c) shows the cross-sectional line profile of the NW, from which we confirmed the presence of In in the core and Ga in the shell. The apparent presence of In in the shell can be explained considering that In and Sb signals are partially overlapping. The same overlapping influences the intensity of the Sb signal in the core part of the NW. On the other hand, the As signal is well resolved, therefore the non-zero intensity of the As signal in the shell really indicates the presence of As together

with Ga and Sb here. The reason of this unintentional As incorporation in the shell is probably the persistence of an As background in the growth chamber during the GaSb deposition, due to the very high As line pressure used for the catalyst-free InAs NW, combined with the very low growth rate of the shell. The precise quantification of the chemical composition of the GaAsSb shell is done in the CDS final structure, as it will be shown later.

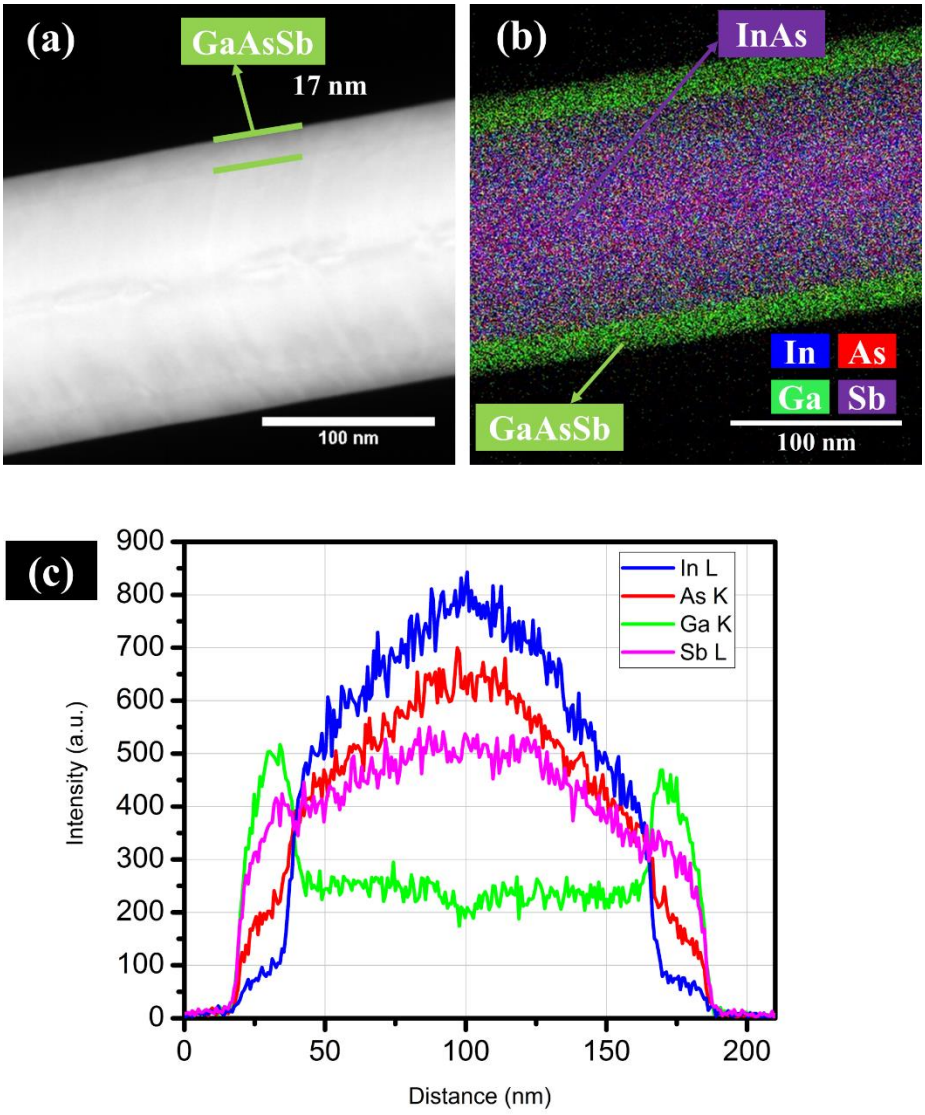

Figure 3.9. (a) STEM-HAADF image of one representative InAs/GaAsSb CS NW obtained after 90 min of GaSb deposition at 370 ± 5 °C with TEGa and TMSb fluxes of 0.5 Torr and 0.43 Torr, respectively. (b) EDX compositional map and (c) elemental line profiles in cross-section of the same InAs/ GaAsSb NW depicted in (a). The results indicate the growth a GaAsSb shell of 17 ± 1 nm thickness around InAs core.

3.5 InAs/InP/GaAsSb core-dual-shell NWs

After the growth optimization of InP and GaAsSb shells separately on the InAs NW core, we combined the three materials in single InAs/InP/GaAsSb CDS

heterostructured NWs. In first step we have grown InAs/InP CS NWs with desired InP shell thickness at 370 ± 5 °C, by using TMIn and TBP line pressures of 0.30 Torr and 1.0 Torr, respectively. Finally, in a second growth step the outer GaSb shell was grown. First, the InAs/InP NWs were kept in UHV environment at room temperature for 30 minutes, while the growth chamber was pumped in order to decrease As and P residual background. Then the sample was re-introduced into the growth chamber and warmed up under TMSb pressure to 370 ± 5 °C, at which we started the outer shell growth using TEGa and TMSb line pressures of 0.50 Torr and 0.43 Torr, respectively. The growth time of the GaAsSb shell was varied to obtain different thicknesses. Finally, the growth was terminated by cooling the sample under TMSb flux.

Figure 3.10 shows a STEM-HAADF image of a representative InAs/InP/GaAsSb CDS NW, aligned along the [112] zone axis, with the corresponding compositional EDX map. InP and GaAsSb growth times were 10 and 140 minutes, respectively, at the same growth temperature of 370 ± 5 °C. The resulting thicknesses of InP and GaAsSb shells measured from STEM images were 14 ± 1 nm and 30 ± 2 nm, respectively. The analysis of several NWs confirmed the presence of the two shells with uniform thicknesses along the growth axis for the whole NW length. As we have already discussed the reason of this unintentional presence of As in the shell is probably the persistence of an As background in the growth chamber during the GaSb deposition, due to the very high As line pressure used for the catalyst-free InAs NW, growth rate of the shell.

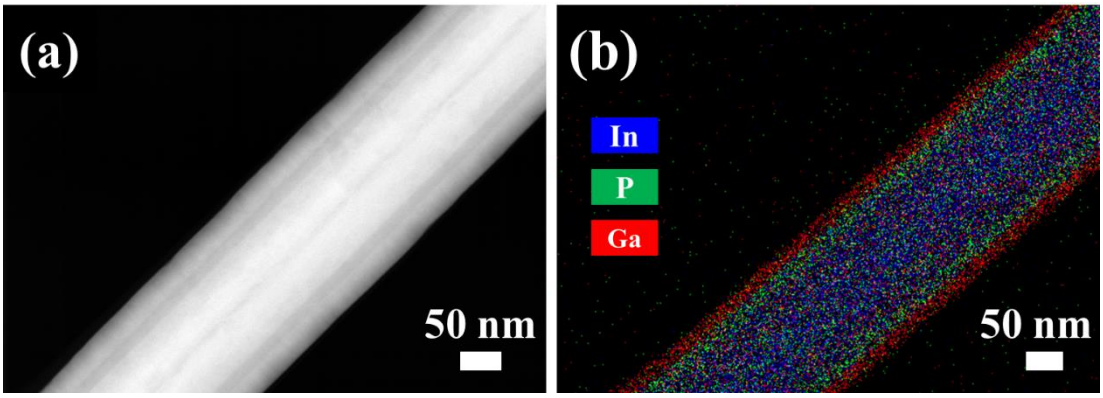

Figure 3.10. (a) STEM-HAADF image acquired in [112] zone axis and (b) EDX compositional map of the middle region of a InAs/InP/GaAsSb CDS NW grown with flux ratio of TMIn/TBP 0.3/1.0 and growth time of 10 min at 370 ± 5 °C for the InP shell (resulting in a 14 ± 1 nm thick InP shell) and flux TEGa/TMSb 0.5/0.43 and growth time 140 min at 370 ± 5 °C for the GaAsSb shell (resulting in a 30 ± 2 nm thick GaAsSb shell).

The HAADF intensity profiles of InAs/InP and InAs/InP/GaAsSb NWs in cross-section along <112> zone axis shown in Fig. 3.11 reveal that the InAs/InP CS NWs have six {110} side facets, so the InP shell grew keeping the same side facet orientation than the InAs core (see panel (a) of Fig. 3.11). Instead, the InAs/InP/GaAsSb CDS NWs show twelve facets: six belong to the {110} family and six belong to the {112} family of planes. This behavior of the GaAsSb shell developing {112} side facets was already observed in the growth of InAs/GaSb [79] and InAs/GaAs [141] CS NWs, and explained by the Wulff's construction [142] that ascribes the final shape of a crystal to the different surface energies of the different facets.

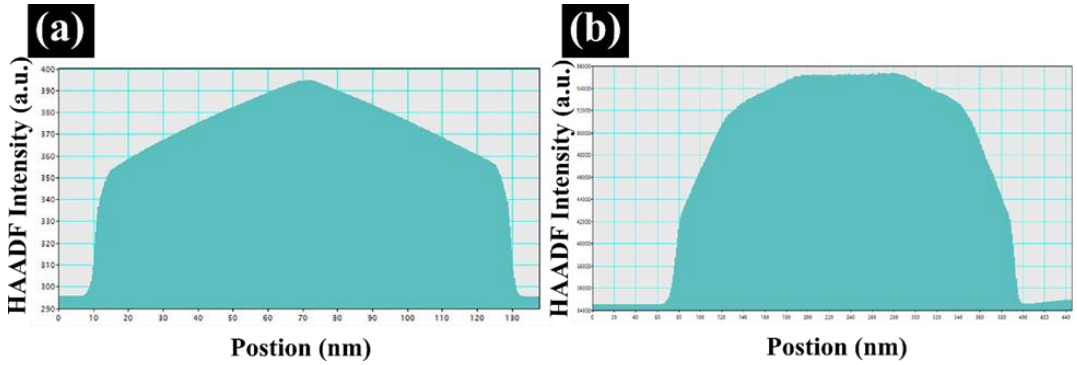

Figure 3.11. STEM-HAADF intensity profiles obtained in cross section on (a) InAs/InP CS NWs and (b) InAs/InP/GaAsSb CDS NWs oriented in <112> zone axis. The InAs/InP CS NW is bounded by six {110} side facets and InP shell follows the same faceting of the InAs core. The InAs/InP/GaAsSb CDS NW is bounded by twelve side facets of the {110} and {112} type.

Furthermore, the Wulff's construction is a method to determine the equilibrium shape of a crystal based on energy minimization arguments [143]. The method states that a point-to-plane distance from the center of a particle to a facet is proportional to the surface energy of the facet. It means that surfaces having larger energy will have a larger growth rate, and this growth rate anisotropy ultimately defines the morphology of the crystal: the slowest growing surface will appear as the largest developed facet in the crystal. Such growth rate anisotropy is governed by the specific surface energies of the respective facets, that are sensitive to the chemical potential, hence by the growth conditions. In our case, with the growth conditions we used, we found that growth rate of GaAsSb is higher in <110> direction as compared to <112> direction, that suggests a higher surface energy of {110} side facets than the {112} ones. This explains why the GaAsSb shell immediately develops {112} side facets in addition to the {110} facets of the InAs NW core, i.e. to minimize the total energy. More details

about growth rate of GaAsSb in different crystallographic directions are explained latter.

3.6 Strain distribution in InAs/InP/GaAsSb core-dual-shell NWs

For strain analysis, the as-grown InAs/InP/GaAsSb CDS NWs were transferred to a suitable substrate and cross-sectional STEM lamellae were cut by FIB (FEI-Helios 650) with a Pt deposited protection layer. The STEM-Moiré pattern of the samples was generated by a probe aberration-corrected STEM (FEI-Titan-Themis) operated at 300 kV equipped with a monochromator. The HAADF detector distance was chosen to gain a collection angle ranging from 40 to 200 mrad, and the scanning resolution was set as 1024 by 1024 pixels with a pixel resolution of 0.19 nm. In order to avoid artifacts due to sample drift, the dwell time of each scanning point was set as 16 μs (18.23 s per frame). The Geometric Phase Analysis (GPA) to calculate the lattice strain was performed by STEM_Cell software [124].

3.6.1 Study of STEM-Moiré patterns

In order to study the strain accommodation at the heterointerfaces in the CDS NWs, we prepared cross-sections perpendicular to the NW growth direction of three samples having different nominal thickness (1, 4 and 8 nm) of InP shell and same of the GaAsSb shell nominal thickness (12 nm) by FIB, and these cross-sectional lamellae were inspected by STEM. In order to identify structural defects and distortions, STEM Moiré patterns [144] were acquired for each sample by aligning the scanning direction along the <112> crystallographic direction and by carefully choosing the line resolution during the scanning. In this case Moiré patterns are generated since the scan step is comparable to the lattice periodicity and fringes are formed in one direction, similarly to a single set of crystalline lattice planes. The results are shown in Fig. 3.12 for the three samples with different InP thickness: 1 nm (a, d, g), 4 nm (b, e, h), and 8 nm (c, f, i).

In all samples the different materials can be easily identified thanks to the Z contrast of the HAADF imaging mode, as visible in panels (a), (b) and (c), which are the STEM-Moiré images of the entire lamellae: the inner part corresponds to the InAs core, the dark central ring represents the InP shell and the external ring is the GaAsSb shell. From the Moiré analysis (<112> scan direction) of the NW cross-sections (panels d-i) of each sample we could identify some structural defects. In particular, in

the sample with InP nominal thickness of 1 nm some dislocations could be found located at the corners (Fig. 3.12 (d)). The InP shell is not well developed here and this could be the reason of the presence of structural defects in this region of the sample. In fact, when all InP facets are well developed, as in case of 4 nm, no defects were found at the corners (see panel (e)).

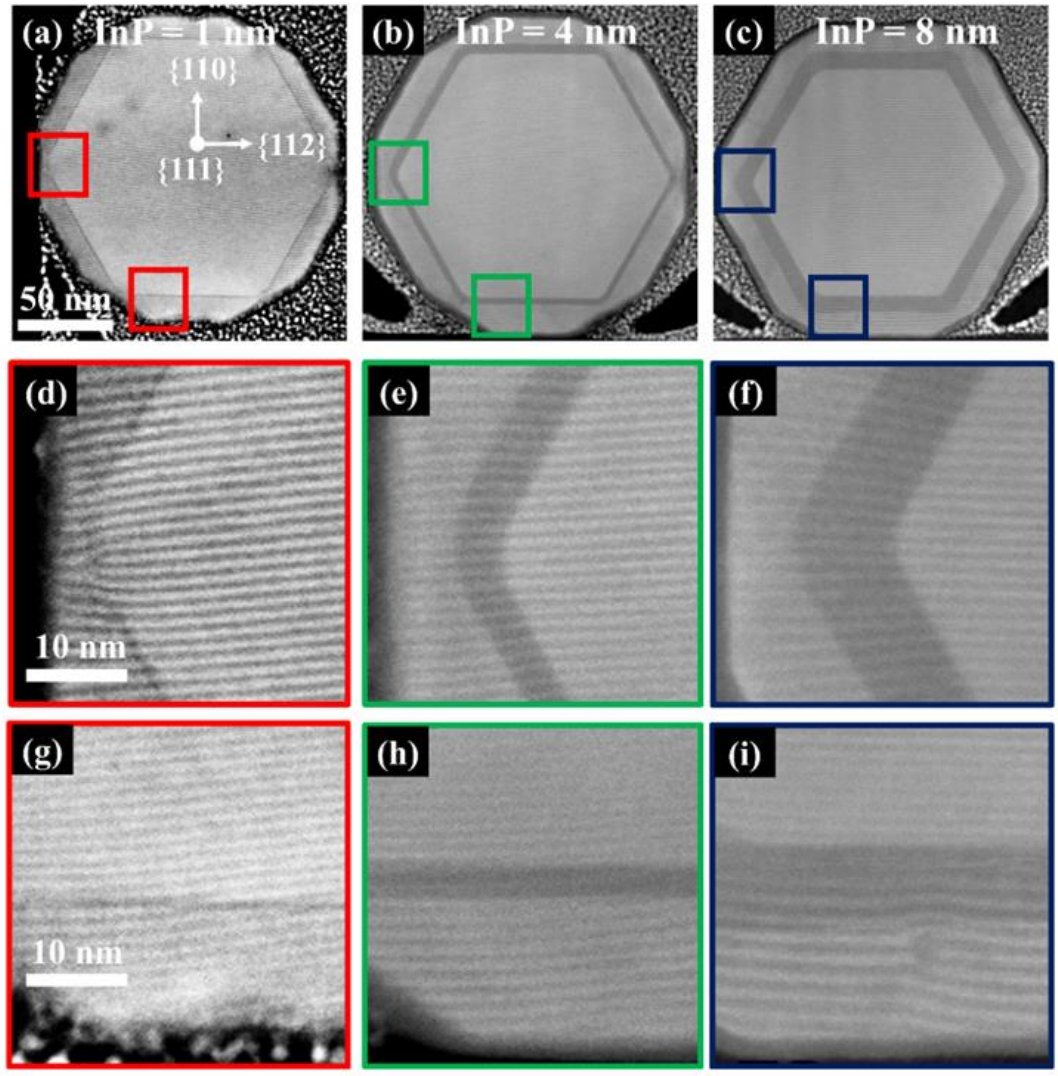

Figure 3.12. (a)-(c). STEM-Moiré images of entire cross-sectional lamellae of the three samples having different InP shell thickness (indicated in the panels). (d)-(f) STEM-Moiré patterns of the selected regions of the lamellae indicated by the colored frames at the {112} side walls. (g)-(i) STEM-Moiré patterns of the selected regions of the lamellae as highlighted by the colored frames at the {110} side walls of NW.

However, for thicker InP shell (8 nm) some dislocations appear see panel (f). We have investigated carefully also the {110} side walls of the CDS NWs, as shown in panels (g, h, i). While the samples with InP nominal thickness of 4 nm do not show any dislocation, the sample with InP nominal thickness of 8 nm shows some dislocations at both the InAs/InP and InP/GaAsSb interfaces and the Moiré pattern

shows lattice distortion (panel i). Moreover, in the 8 nm-InP sample, the HR-STEM analysis reveals that the InAs/InP and InP/GaAsSb interfaces are not atomically flat and an increased roughness is observed as shown in HR-TEM images of Fig. 3.13. This roughening may play a role in the relaxation process of the strain of the system [145].

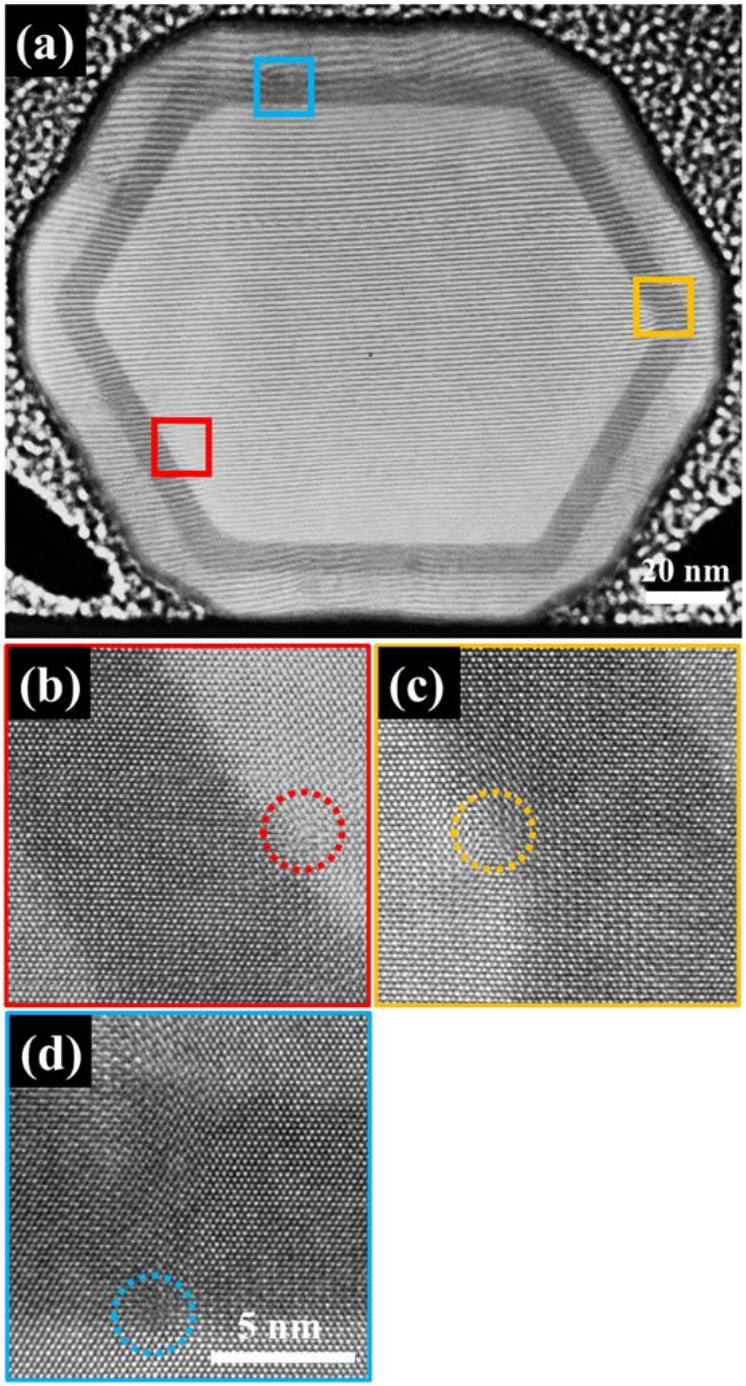

Figure 3.13. STEM analysis of the InAs/InP interface of the sample with 8 nm InP barrier. (a) STEM-Moiré image of entire NW cross section. (b)-(d) HR-STEM images of the defected InAs/InP {110} sidewall interfaces. The colored squares are indicating the corresponding locations and the defects are emphasized by circles.

3.6.2 Thickness analyses

From the STEM analysis of these lamellae as shown in Fig. 3.14, we also noticed that the actual shell thicknesses are different along the <110> and <112> directions of the NWs, as summarized in Table 3.2.

Table 3.2: Actual shell thicknesses in the <110> and <112> directions of the NWs.

	Measured thickness in <110> direction (nm)		**Measured thickness in <112> direction (nm)**	
Nominal InP thickness (nm)	**InP**	**GaAsSb**	**InP**	**GaAsSb**
1	1.0 ± 0.1	11.0 ± 0.9	<1.0	Unknown (interface not visible)
4	4.0 ± 0.9	13.0 ± 1.0	4.0 ± 0.9	5.5 ± 1.2
8	8.0 ± 0.5	11 ± 0.7	9.0 ± 0.6	6.6 ± 1

In the sample with 1 nm InP (nominal thickness), the average values for the thickness of InP and GaAsSb along the <110> direction (perpendicular to the InAs side facets) are 1.0 ± 0.1 nm and 11.0 ± 0.9 nm, respectively. On the other hand, along the <112> direction (InAs corners) the InP shell is at least 2 monolayers thinner, as suggested by the lack of a clear HAADF contrast in the image, that makes difficult to measure also the GaAsSb thickness in this direction. In the sample with InP nominal thickness of 4 nm the mean value of GaAsSb shell thickness is 13.0 ± 1.0 nm along the <110> direction and 5.5 ± 1.2 nm along the <112> direction. The InP shell, instead, is uniformly grown along both directions with a thickness of 4.0 ± 0.9 nm in this case. Finally, in the sample with InP nominal thickness of 8 nm we measured GaAsSb and InP shell thickness in the <110> direction of 11 ± 0.7 and 8.0 ± 0.5 nm, respectively. The shell thicknesses of GaAsSb and InP along the <112> direction are 6.6 ± 1 nm and 9.0 ± 0.6 nm, respectively.

So the analysis of the shell thickness along the two directions suggests that the growth rate of the GaAsSb shell is higher in the <110> direction as compared to <112> direction, leading to a non-uniform shell thickness. This explains also the development of the low energy <112> facets in the GaAsSb shell [142]. By contrast, the InP shell is quite uniform in the two directions when the nominal thickness is higher than 1 nm. For shorter InP growth times, however, the InP shell is well defined only in the <110> direction, suggesting an island-growth mode with preferential nucleation on the InAs

side facets. This kind of behavior can be attributed to the different surface energy, surface reconstruction, surface diffusion and nucleation kinetics in the different crystallographic directions [82]. However, a deeper analysis of the growth mechanisms is beyond the scope of the present study.

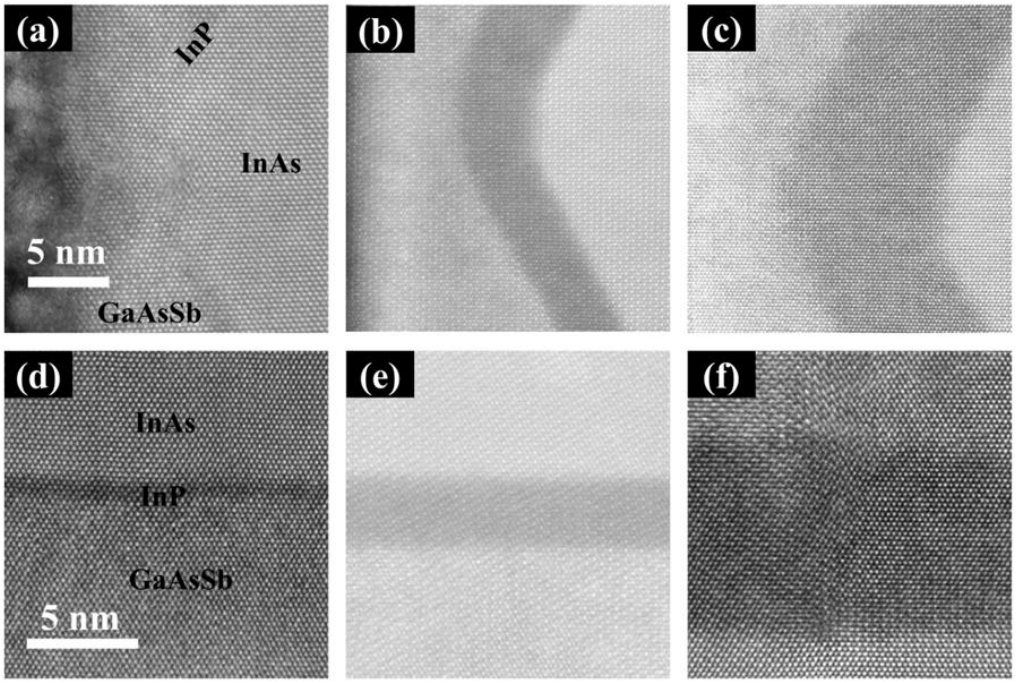

Figure 3.14. HR-STEM images of InAs/InP/GaAsSb CDS NWs at the {112} (a-c) and {110} (d-f) sidewalls.

3.6.3 Strain mapping

For the detailed strain analysis at the heterointerfaces, high resolution STEM-HAADF images were acquired and processed with the geometric phase analysis (GPA) method to extract the local components of the strain in the <110> and <112> directions and get strain maps. In general, strain from GPA map is defined as $\varepsilon_{GPA} = (d_{loc} - d_{ref})/d_{ref}$, where d_{loc} is the interplanar spacing of the local part and d_{ref} is the interplanar spacing of reference part which is InAs in our case [145]. Figure 3.15 shows the results of our STEM-GPA analysis for the three samples with different InP barrier thickness. Panels (a), (e) and (i) are the STEM images of the three different samples, while panels (b,c), (f,g) and (j,k) are the corresponding GPA maps of ε_{xx} (i.e. variation of the interplanar spacing in the <112> direction, parallel to the interface) and ε_{yy} (i.e. variation of the interplanar spacing in the <110> direction, perpendicular to the interface). For the last in panels (d,h,l) we report also a line profile across the heterointerfaces.

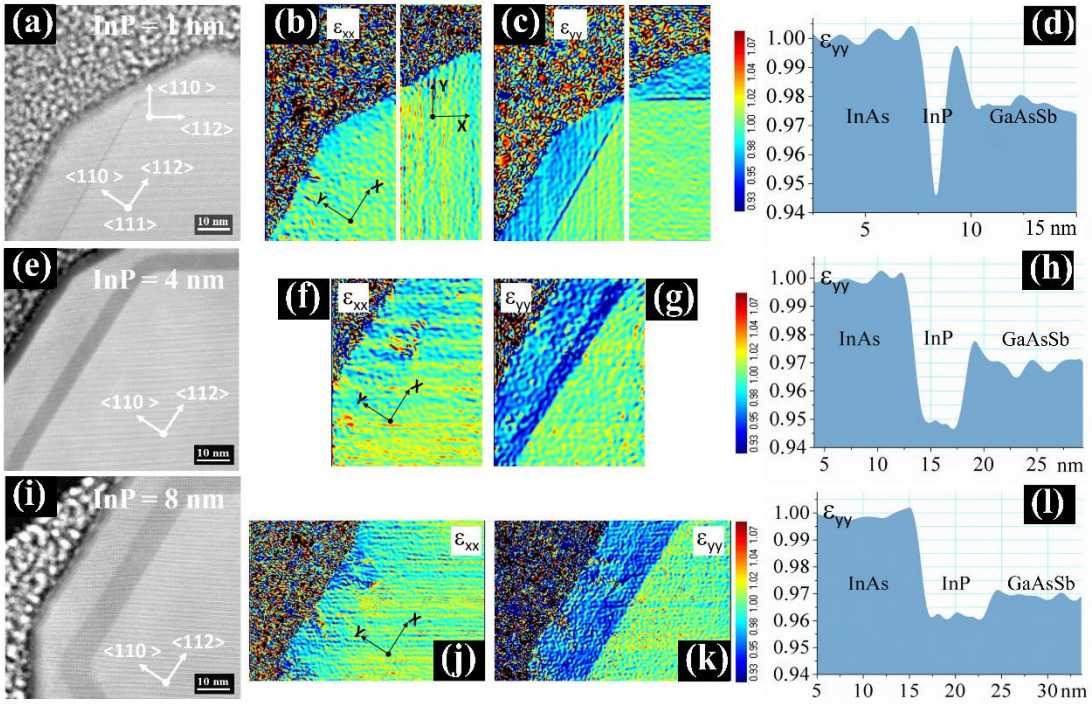

Figure 3.15. HR-STEM images (a, e, i) of the InAs/InP/GaAsSb interface region of the three samples with different InP thickness and corresponding GPA maps of ε_{xx} (b, f, j) and ε_{yy} (c, g, k) strain components. Panels (d,h,l) show the line profiles of ε_{yy} across the two interfaces.

Interestingly, no abrupt changes in ε_{xx} across the interfaces were seen, suggesting that the in-plane lattice parameter of the shell materials is fully strained and adapted to the in-plane lattice parameter of InAs. Only in the 8 nm thick InP sample, an initial relaxation is observed, in agreement with the HR-STEM findings on the presence of dislocations at the interface. On the other hand, from GPA map of ε_{yy}, the two interfaces can be easily identified in all the samples. Indeed, the interplanar spacing perpendicular to the interface varies abruptly, as clearly visible also from the ε_{yy} line profiles, meaning that the shell lattice in this direction is free to accommodate the strain. The average value of ε_{yy} for GaAsSb is -3% and for InP is -5%. In order to understand these results, we need to precisely quantify the chemical composition of the two shells, so we performed EDX analysis of these lamellae as displayed in Fig. 3.16.

As previously emphasized, from the EDX analysis it was found that the outer shell is an alloy instead of a pure GaSb shell. In the outer shell we found 40% As and 60% Sb, therefore the chemical composition is $GaAs_{0.4}Sb_{0.6}$. This explains the strain measured from ε_{yy} line profile, indeed a GaAsSb alloy with such composition is expected to have a lattice parameter in the ZB phase close to 0.59 nm [127], giving a negative $\varepsilon_{yy\text{-}GaSb}$ as experimentally observed.

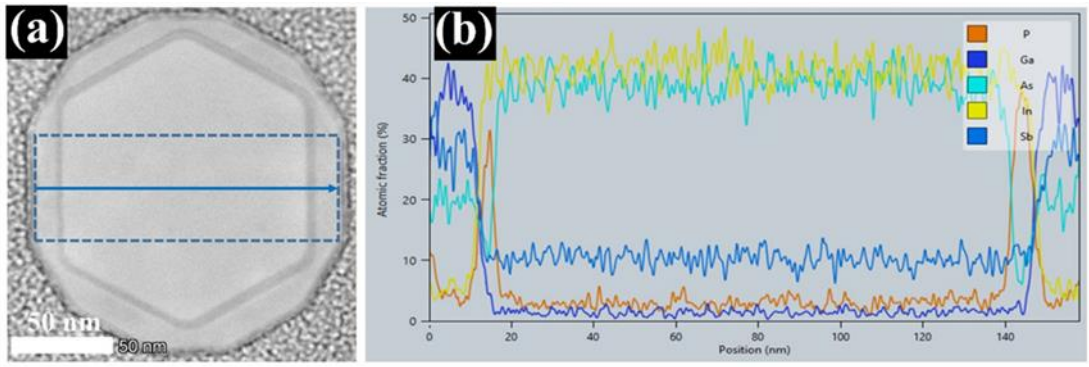

Figure 3.16. Cross-sectional STEM image (a) and elemental line profiles (b) of an InAs/InP/GaAsSb CDS NW.

Concerning the InP shell, from the EDX analysis we found a small As signal also here, but in much smaller concentration (less than 10 atomic %). As already mentioned, the unintentional As incorporation in both shells can be due to the residual As background in the growth chamber after the InAs growth with very high TBAs line pressure. The higher As incorporation during GaSb deposition, compared to the InP deposition can be a consequence of the much higher growth rate of InP (1.4 nm/min) compared with the one of GaAsSb (0.21 nm/min) and to the different Ga and In preferential bonding with As than Sb or P when both group V elements are present in the vapor phase [146]. Moreover, it is well known that chemical processes involved in the CBE technique are quite complex and that a large number of possible species and reaction pathways in the vapor phase can complicate the link between precursor flux ratios and the final chemical composition of the grown structure [147]. This problem could be reduced by increasing the GaAsSb shell growth rate, at higher growth temperature, or allowing for As pump out through a much longer growth interruption between the InAs core and the GaSb shell growth**.**

3.6.4 Strain analysis

Some considerations can be made on the experimental values of ε_{yy} from the GPA maps. According to the model presented in Ref. [148] for ZB heterostructures grown along the <hhk> direction (in our case: <110>), an epilayer (in our case: shell) pseudomorphically grown on top of a different material (in our case: InAs core) with a certain lattice mismatch Δa/a will assume an out of plane parameter d determined by the so-called tetragonal distortion. Quantitatively, for {110} interfaces,

$$\frac{\Delta d}{d} = \frac{2c_{11} + 4c_{12}}{c_{11} + c_{12} + 2c_{44}} \frac{\Delta a}{a}$$

where c_{11}, c_{12} and c_{44} are the elastic stiffness constants of the epilayer. In this approximation, for the InP shell over InAs core we can expect $\Delta d/d$ (ε_{yy} in GPA notation) =1.7 $\Delta a/a$.

Considering those of $GaAs_{0.4}Sb_{0.6}$ from the literature [149] we get $\Delta d/d = 1.5\ \Delta a/a$. The lattice constant of $GaAs_{0.4}Sb_{0.6}$ is 0.59 nm, so $\Delta a/a = -2.14$ % and we obtain $\varepsilon_{yy} = -3.2$ %, which is in good agreement the measured value of ε_{yy} (about 0.97, being 1 the InAs reference). Similarly, taking the elastic stiffness constants of an InAsP alloy with 10% As, it is expected $\varepsilon_{yy} = 1.7\ \Delta a/a$ [148]. Since the lattice mismatch for such $InAs_{0.1}P_{0.9}$ layer grown on InAs is $\Delta a/a = -2.8$ %, we obtain $\varepsilon_{yy} = -4.8$ %, which is in good agreement with the values of the ε_{yy} profile at the InAs/InP interface ($\varepsilon_{yy} = -5$ %). It should be noted that ε_{yy} in the sample with 8 nm thick InP shell is a bit smaller than the other samples. This is probably related to the partial relaxation that starts to occur in this sample: the out of plane parameter is no more constrained by tetragonal distortion but at the same time it is not yet come back to that of free InP, so that ε_{yy} takes a value in the range between - 4.8 % (tetragonal distortion) and - 2.8 % (relaxed InP).

From our analysis, we can conclude that InAs/InP/GaAsSb CDS NWs with InP thickness higher than 1 nm and at least up to 4 nm present flat interfaces without dislocations. In particular, the InP shell adopts a lattice parameter coherent with that of the InAs core along the <112> direction (parallel to the interface), while it is elastically compressed along <110> direction (perpendicular to the interface) according to a tetragonal distortion of the lattice. This distortion can accommodate strain energy without misfit dislocations and is a well-known process that occurs when two lattice mismatched materials are grown one on each other, below the critical thickness. Indeed, above a certain thickness the strain energy is too high to be accommodated through a lattice distortion, so the system relaxes more efficiently by producing misfit dislocations [150]. This is consistent with our observation that in InAs/InP/GaAsSb CDS NWs with 8 nm InP some dislocations and interface roughness occur at the interfaces as a consequence of the increased strain field.

3.7 Conclusions

Optimized InAs/InP/GaAsSb CDS NWs were realized by catalyst-free CBE by varying the growth parameters. It is demonstrated that 370 °C is best growth temperature to obtain homogenous and smooth shell along growth direction for both

InP and GaAsSb shell. We found that the InP shell is not uniformly developed when the nominal thickness is around 1 nm and some dislocations are observed at the corners, where the InP is thinner. For samples with the InP thickness above 1 nm and below 8 nm the InP shell is uniform along all the crystallographic directions and we could not find any dislocation at the heterointerfaces. GPA maps indicate that the strain is accommodated through a tetragonal distortion of the lattice without forming structural defects. On the other hand, when the InP shell is thicker, the interfaces are not flat anymore, but an increased roughness is observed and dislocations start to form. Our study provides useful guidelines for obtaining device-quality InAs/InP/GaAsSb CDS NWs. Moreover, the present approach can be applied to other lattice-mismatched material combinations in order to expand the range of options for device implementation.

Chapter 4: Electrical transport study of InAs/InP/GaAsSb core-dual-shell NWs

4.1 Introduction

III-V semiconductor NWs are considered as promising candidates for engineering of unique devices in nanoscale level in the field of tunnel field effect transistors, high speed electronics, optoelectronics, and photonics [151-157]. The extraordinary features of NWs such tailoring of wide range of band gap, efficient lateral strain relaxations and free standing nature provides unique platform [40,54]. Specially, NW heterostructures with radial symmetry such as core-shell or core-multishell NWs [134,153,158] act as extremely promising systems for next generation electronic and optoelectronic nano-devices [17,87-90,159]. In these systems, the band gap alignment can be tuned by means of source-drain voltage, back-gate voltage and by field effect modulation which creates a new pathway to explore broken-gap systems and band-to-band tunnelling in Esaki diodes [87,88,159,160], should be as well as the study of spin-orbit interaction [89,90]. Recently, a charge transport study based on InAs/GaSb CS NWs is reported [87]. They demonstrated modulation of negative differential resistance (NDR) and Esaki effect as a function of field-effect. This modulation is appreciated in terms of tuning of the local band gap alignment of the InAs/GaSb interface along the radial junction. NDR is a common behaviour of electron tunnelling across a broken gap heterojunction which enables application in tunnelling field effect transistors [161,162] and tunneling diodes [163,164]. In general, this kind of radial heterostructures where mobile electrons and holes coexist at equilibrium without any need of an external electric field could open the way to fundamental studies on Coulomb drag phenomena in low dimension [91] as well as to novel schemes for the detection of indirect excitons [92]. To this end, a thin InP layer was epitaxially grown between the InAs core and the GaAsSb shell, realizing a CDS NW geometry as described in chapter 3, in order to electrically insulate n-type and p-type conduction in the core and outer shell, respectively. The existence of NDR is employed to determine the presence of radial tunnelling across the InAs/GaAsSb broken gap heterojunction.

In this chapter, we will demonstrate the impact of the thickness of the InP barrier on the NDR suppression. Furthermore, different device architectures allow us to selectively contact the core and the shell of the device and enable multiple measurement configurations: shell-shell (S-S), core-core (C-C), and core-shell (C-S). This allows us to measure radial and axial charge transport in the same nanostructure for the investigation of the coexistence of electrons and holes and of their Coulomb pairing. The device fabrication and measurements were performed in collaboration with Sedighe Salimian and Francesco Rossella. The results were published in Ref. [165].

4.2 Experimental details

4.2.1 Growth protocol of InAs/InP/GaAsSb core-dual-shell NWs

Catalyst-free InAs/InP/GaAsSb CDS NWs were grown on Si (111) substrates, following the growth protocol described in chapter 3. In particular, we have grown two samples with different thickness of the InP shell and same thickness of GaAsSb shell. The average length of the NWs was 1.8 ± 0.2 μm. The resulting thicknesses of InP and GaAsSb shells measured from STEM images, were 5 ± 1 nm and 34 ± 4 nm for sample A and 10 ± 1 nm and 32 ± 4 nm for sample B. Average edge-to-edge and facet-to-facet InAs core diameters were 165 ± 4 nm and 143 nm $\pm$ 4 nm, respectively. The resulting STEM images are shown in Fig. 4.1 panel (b) and (c). The shell thickness along the growth direction of NWs is smooth and homogenous in both InP and GaAsSb shells.

4.2.2 Device fabrication and architectures

In order to fabricate NW-based devices, the InAs/InP/GaAsSb CDS NWs were transferred from the grown substrate to SiO_2/Si^{++} (300 nm/500 μm) substrate by dry transfer method and then electrical contacts were formed with the help of electron beam lithography (EBL). In first step, we fabricated a set of two-contact devices with a pair of electrodes placed onto the GaAsSb shell, enabling the configuration of measure hereby referred to as “shell-shell” (S-S). The contact areas of the nanostructure was passivated by using a $HCl:H_2O$ (1:2) wet etching protocol (lasting for 30 s, stopped in H_2O) in order to remove native oxides from the NW surface. Afterwards, Ni/Au (10/300 nm) electrodes were deposited by thermal evaporation. Successively, we fabricated a second set of devices consist of four-contact, enabling in the same nanostructure three possible measurement configurations, it is referred to as “shell-shell” (S-S), “core-core” (C-C), and “core-shell” (C-S). To this end, we

established a fabrication protocol including an additional etching step to remove the GaAsSb shell and the InP barrier from both ends of the NW, uncovering the InAs core. After this etching step, we used HCl:H_2O (1:2) to passivate four selected areas in a single step, namely two areas on the GaAsSb shell and the two ends of the InAs core. Finally, we evaporated the metallic electrodes. This allowed us to selectively and independently contact the core and the shell of our InAs/InP/GaAsSb CDS NWs.

4.3 Charge transport in two-contact devices

The effect of InP barrier on the electrical transport in InAs/InP/GaAsSb CDS NWs in term of InP barrier thickness is examined. Charge transport of InAs/InP/GaAsSb CDS NW-based devices was determined between room temperature (RT) and 4.2 K. Current-voltage (*I-V*) characteristics were performed using a DL1211 current preamplifier, while a Keithley 2614B power supply was used to control the back gate voltage bias. We first analysed two-terminal devices fabricated with individual NWs from the two samples (referred to as sample A and B). The geometry with respective dimensions of single InAs/InP/GaAsSb CDS NW is shown in schematic diagram of Fig. 4.1 (a).

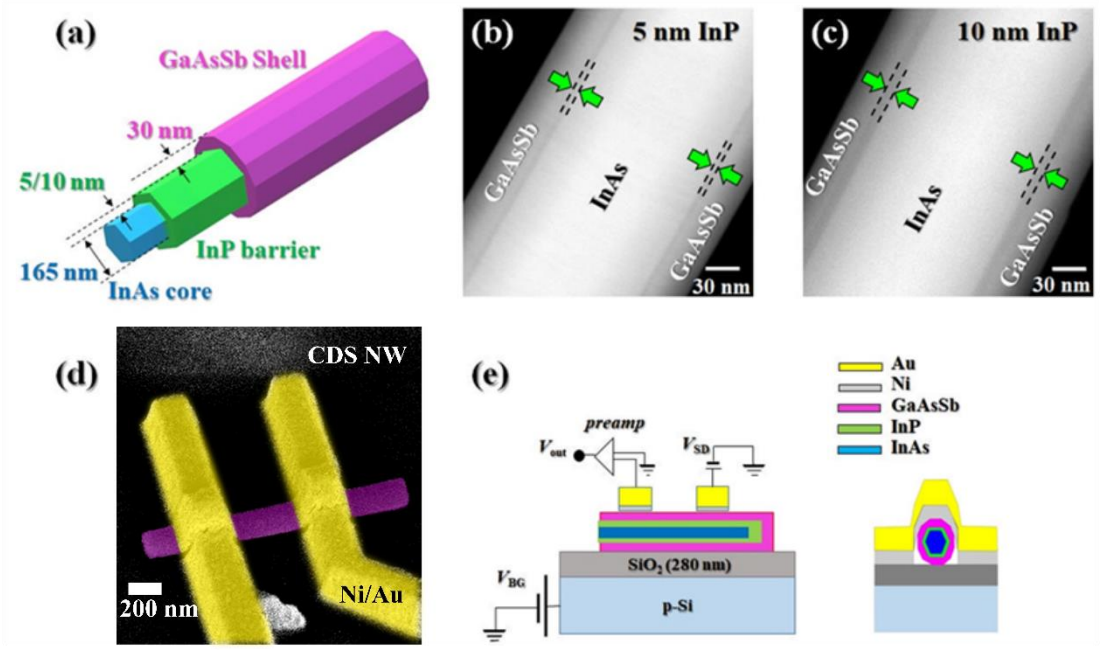

Figure 4.1. (a) Schematic diagram of InAs/InP/GaAsSb CDS NW. STEM micrographs of CDS NWs with (b) 5 ± 1 nm and (c) 10 ± 1 nm-thick InP barrier; arrows highlight the thickness of the InP shell. (d) Top view SEM image of one of our shell-shell devices fabricated onto a SiO_2/p-Si substrate. Purple and yellow colors correspond to GaAsSb shell and Au electrodes, respectively. (e) left side is the schematic of the device architecture, with the circuit for transport experiments in shell-shell configuration (two-wires) depicted in overlay and right side is the schematic of a contact cross-section.

The structure of one of our prototypical devices is shown by a false color SEM image in Fig. 4.1 (d). The two electrical contacts (yellow colored) were evaporated onto the outer most GaAsSb shell (pink colored), which allow the measurement of electrical transport in the S-S geometry. Figure 4.1 (e) illustration of the device architecture as well as the setup used to measure the *I-V* characteristics of the device in S-S configuration. The two electrodes enable us to measure the electrical resistance and to evaluate the influence of a voltage bias applied to the degenerately-doped Si^{++} back-layer of the SiO_2/Si^{++} substrate. We can consider it as a back-gate voltage which modulates the transport properties of the heterostructure.

We determined the electrical resistance in two-contact devices fabricated from CDS NWs of sample A (5 nm InP barrier) and sample B (10 nm InP barrier), at 300 K and at 4.2 K. In our two-contact devices, the electrodes were typically placed 200-300 nm far from both ends of NW. Because, EDX maps reported in Ref. [134] revealed a GaAsSb/InP axial-growth of about 200 nm at the end of NW: so it is worth to avoid to put electrodes on this parts; similarly, we avoid electrical contact to the bottom of NW. The distance between the electrodes was in the range 0.8-1 μm.

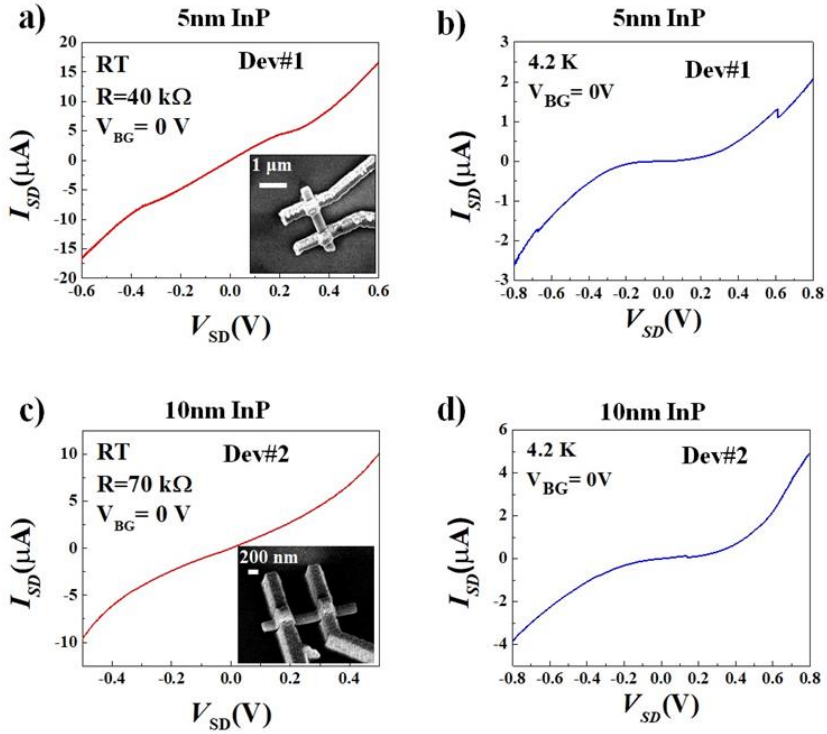

Figure 4.2. Two probe resistance of Dev#1 with 5 nm InP barrier (V_{BG} = 0 V) at (a) room temperature and (b) low temperature (4.2 K). Two probe resistance of Dev#2 with 10nm InP barrier (V_{BG} = 0 V) at (c) room temperature and (d) low temperature (4.2 K). Insets are the tilted SEM images of devices with two contacts on the GaAsSb shell of CDS NW.

In Figure 4.2 we describe the results for two of our devices: dev#1 fabricated with CDS NW from sample A, and dev#2 fabricated with CDS NW from sample B, SEM micrographs of the two devices are displayed in the insets. The resistance measured in the two devices was 40 kΩ and 70 kΩ for dev#1 and dev#2, respectively at 300 K. In the *I-V* characteristics of dev#1 at 300 K, we noticed two plateau-like features occurring at about $V_{SD} \approx$ -0.3 V and $V_{SD} \approx$ +0.3 V; At 4.2 K, these two weak features develop in marked negative differential resistance (NDR) features that occur at about $V_{SD} \approx$ -0.7 V and $V_{SD} \approx$ +0.6 V and the resistances of both devices increased significantly in the low range of source-drain voltage bias. Furthermore, the measured *I-V* characteristics curves at RT in the S-S geometry were linear in a drain-source voltage $|V_{SD}|$ range well exceeding 200 mV in case of all our devices. The electrical resistance was ranging typically from 10 to 70 kΩ in different devices, indicating a very good quality of the metal-semiconductor interface; the resistance of devices with 10 nm InP barrier was slightly higher with respect to that of the devices with a 5nm InP barrier.

A set of *I-V* characteristics obtained at 4.2 K in the S-S geometry for NWs from sample A (5 nm-thick InP shell) in the V_{SD} range from −0.75 V to +0.75 V, for different applied back-gate voltages V_{BG} in the range from −40 to +40 V is shown in Fig. 4.3 panel (a).

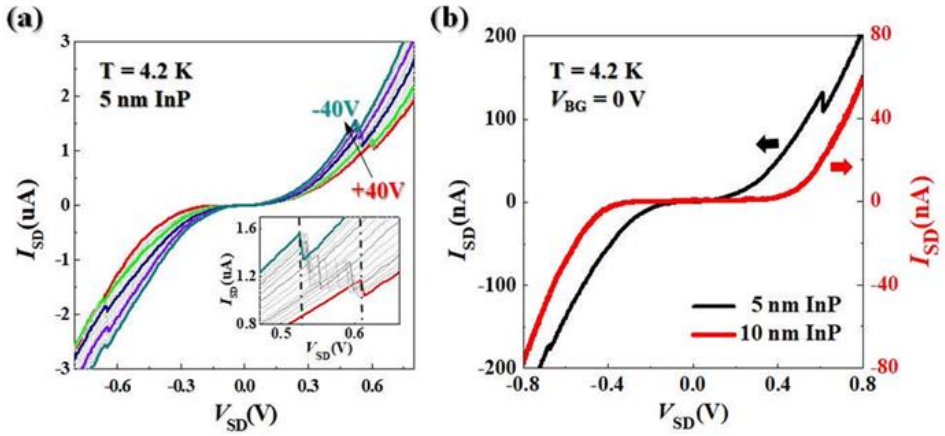

Figure 4.3. Transport properties of InAs/InP/GaAsSb CDS NW-based devices measured in S-S geometry at 4.2 K. (a) *I-V* characteristic of a NW-based device with 5 nm-thick InP, at different back gate voltages. (Inset) Magnification of *I-V* curves in the V_{SD} region displaying negative differential resistance. (b) The comparison between the *I-V* characteristics of devices characterized by 5 nm-thick (black curve) and 10 nm-thick (red curve) InP shell, with V_{BG} = 0 V.

The *I-V* curves shows the presence of NDR characteristics at $|V_{SD}| \approx 0.6$ V for both positive and negative values of V_{SD}. This phenomenology can be attributed to the

Esaki effect in presence of direct tunnelling transport mechanism through the thin InP barrier. This is signature of a shell-core-shell path of the carriers. In particular, the observation of NDR for both positive and negative values of V_{SD} is consistent with the presence of two radial back-to-back Esaki-like diodes due to presences of broken-gap junction. Further, the behavior of NDR widely discussed for InAs/GaSb NW-based devices in the previous work [87]. In the present case, however, the nonlinear feature (NDR) occurring in the *I-V* curves is quantitatively different with respect to the case of InAs/GaSb CS NWs. In fact, at V_{BG} = 0 V the NDR occurs at larger source-drain bias voltage ($|V_{SD}| \approx 0.6$ in Fig. 4.2 (b)), while the overall impact of the application of a back-gate voltage is significantly weaker. Indeed, both the position of the NDR as well as the peak-to-valley ratio (PVR) are poorly modulated by the application of a back-gate voltage, ranging from V_{SD} = 0.52 V to V_{SD} = 0.60 V and PVR = 1.16 at V_{BG} = − 40 V and PVR = 1.13 at V_{BG} = + 40 V. We observe a V_{BG} dependence consistent with a p-type semiconductor. We will address this point in more detail later in Section 4.4. In all our devices we revealed this behavior, with NDR occurring in the range $|V_{SD}| \approx$ 0.3-0.6 V and weak PVR.

We justify these experimental evidences by considering that the InP barrier introduces an additional load resistance in series with the non-linear components (InAs-GaAsSb junction), place NDR at larger source-drain bias with respect to the case of study reported in Ref. [87], and reducing the effect of the field effect. Regarding the different features of the NDRs reported for opposite V_{SD} in Fig. 4.3 (a), these can be tentatively ascribed to non-idealities of the heterojunctions. In an ideal device, one could feature a uniform band alignment along the azimuthal angle of the NW, yielding to identical NDR features for opposite V_{SD}. In a real device, any local built-in disorder or slight asymmetry in the electrical contacts may lead to non-uniformities of the junctions or to NDR conditions locally occurring at different values of V_{SD}. On top of this, no uniformity in the junction can be affected by the back-gate, due to its asymmetry with respect to the NW center that yields to a different impact on the NW facets for a given S-D bias (particularly in the case of the top and bottom facets).

Figure 4.3 (b) reports two *I-V* curves at 4.2 K and V_{BG} = 0 V, measured in the V_{SD} range from -0.8 V to +0.8 V in the S-S configuration for two different devices: the black curve refers to a device fabricated with a 5 nm-barrier CDS NW (sample A),

while the red curve corresponds to a 10 nm-barrier CDS NW (sample B). We estimated the device resistance from the linear fit of the two *I-V* characteristics for $|V_{DS}| > 0.6$ V, and we obtained ≈ 2 MΩ for device with sample A NW and 5 MΩ for device with sample B. The key qualitative difference between the black and red curves concerns the presence of NDR: increasing the InP shell thickness is found to completely suppress this characteristic nonlinear feature. At 4.2 K, we measured more than 10 devices for both samples. We systematically observed that devices with NWs of sample B are more resistive (by factor two or three) with respect to devices with NWs of sample A. Besides, they did not show NDR but a monotonic increase of $|I_{SD}|$ for increasing $|V_{SD}|$.

Moreover, we measured the *I-V* characteristics of devices with CDS NW from sample A (5 nm InP barrier) and B (10 nm InP barrier) as a function of temperature are reported in Fig. 4.4. Panel (a) highlights two temperature range: high temperature range, evidenced with red bars and magnified in panel (b); low temperature range, evidenced with light-blue bar and magnified in panel (c). In panel (a), the position of NDR measured at about 300 K and 100 K is indicated with dashed red lines and corresponds to $V_{SD} \approx 0.28$ V and 0.53 V, respectively. The magnified range shown in both panel (b) and (c) displays a clear shift of the NDR position as a function of temperature: the NDR moves towards higher source-drain voltage bias while the temperature decreases. Also it evolves into a sharper and stronger feature by lowering the temperature. These experimental evidences are qualitatively consistent with the results reported for InAs/GaSb CS NWs in Ref. [87]. Dev#4 and Dev#5 show that with 10 nm InP barrier the NDR is suppressed in the entire temperature range from 4.2 K to 300 K.

On the one hand, our results suggest the absence of tunnelling across the 10 nm-thick InP shell (sample B) and consequently indicates that only the GaAsSb shell contributes to the conduction. On the other hand, in general when measuring two-contact devices in the S-S configuration, it is not trivial to exactly visualize the charge trajectories, identifying the possible contributions to the current arising from the GaAsSb shell, the InAs core and the InP barrier. In order to tackle this point, starting from InAs/InP/GaAsSb CDS NWs of sample B, as already mentioned we fabricated four-terminal devices that allow us to measure independently in the same

nanostructure the electrical resistance of the InAs core (C-C), of the GaAsSb shell (S-S), and across the InAs/InP/GaAsSb heterojunction (C-S).

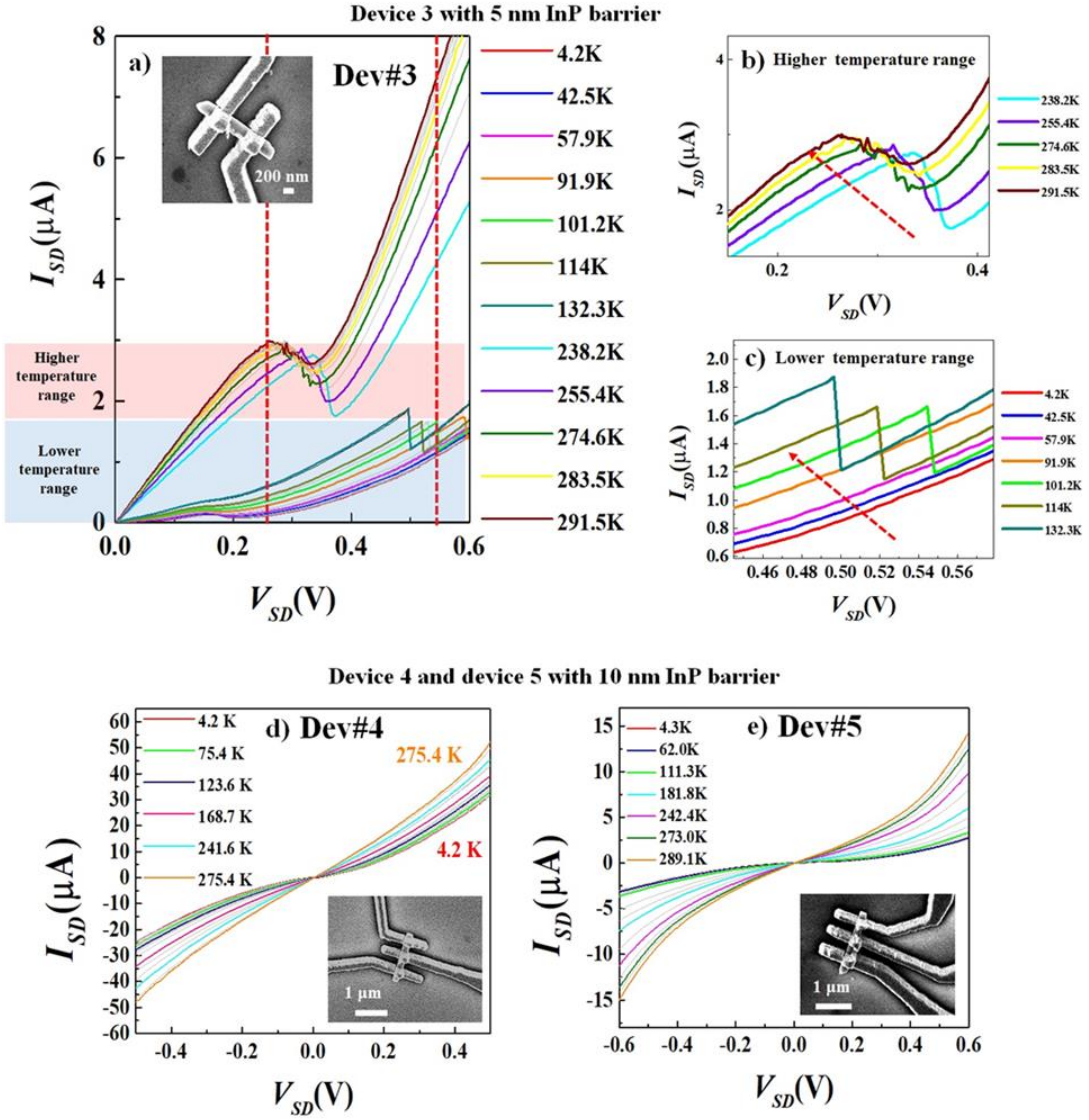

Figure 4.4. (a) *I-V* characteristic of Dev#3 as a function of temperature. (b) High temperature range of measurements from 238 K to 291 K. (c) Low temperature range of measurements from 132 K to 4.2 K. (d) I-V characteristic of Dev#4 as a function of temperature. Inset: tilted SEM image of device; two probe measurement was performed from close contacts with 400 nm distance therefore the total resistance is lower than typical resistance of other devices (10 nm InP barrier) with larger distance (≈ 0.6 to 1 μm) between the two close contacts. (e) *I-V* characteristic of Dev#5 as a function of temperature. Insets: tilted SEM image of the device.

4.4 Charge transport in four-contact devices with 10 nm InP barrier

The four-contact devices were fabricated by using the protocol described in section 4.2.2. Figure 4.5 (a) shows the pictorial view of a CDS NW before (left panel) and after (right panel) the etching step. Figure 4.5 (b) reports the SEM micrograph (top view) of a CDS NW where, at one end, the InAs core (blue colored area) is set free from the InP barrier and the GaAsSb shell (violet colored area). Noticeably, the

minimized etchant infiltration allows to remove the shells from well-defined regions and with a relatively sharp interface between the pristine and etched regions. Figure 4.5 (c) reports a top-view SEM micrograph of an InAs/InP/GaAsSb CDS NW where GaAsSb shell and InP were removed at both ends of the CDS in a single etching step, and shows the high control of the etching procedure on selective areas of InAs/InP/GaAsSb CDS NWs. This provided the key step for the fabrication of four-contact devices allowing to probe the charge transport in the InAs core, in the GaAsSb shell and across the series of radial heterojunctions (InAs/InP and InP/GaAsSb).

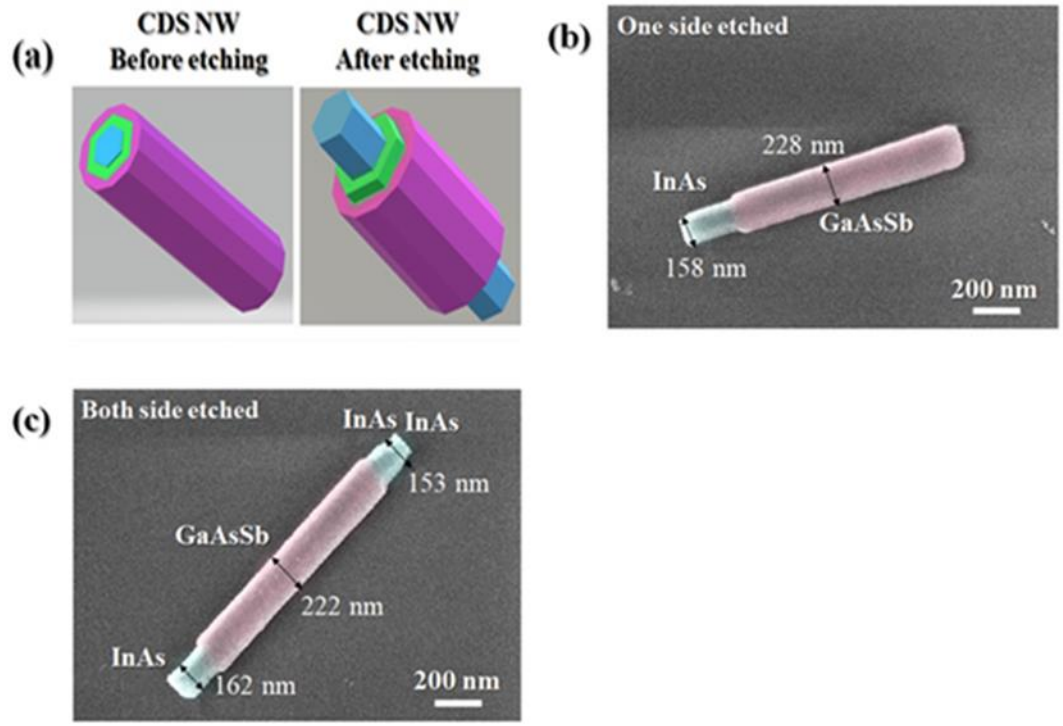

Figure 4.5. (a) Sketch of CDS NWs with 12 facets, before (left panel) and after (right panel) etching. (b) SEM images of one side etched and (c) two sides etched nanowires used for the fabrication of multiple electrodes device architectures; pink and blue colors correspond to GaAsSb shell and InAs core, respectively.

A false color SEM micrograph (top-view) of one of our four-contact devices fabricated starting from individual InAs/InP/GaAsSb CDS NWs of sample B is shown in Fig. 4.6 panel (a). Electrodes 1-4 provide electrical contact to the bare InAs core, while contacts 2-3 are connected to the GaAsSb shell. Two different cross-sectional views of our devices are schematically depicted in Fig. 4.6 (b), with color code accounting for the different materials. With this device architecture, in the same CDS NW, axial charge transport can be measured across the GaAsSb shell using contacts 2-3 and across the InAs core using contacts 1-4, while radial transport across the multiple heterojunction can be measured using contacts 1-2 (or 3-4). Besides, the application of a voltage bias to the degenerately doped silicon of the SiO_2/Si^{++}

substrate allows to probe field-effect modulation in any of the three configurations mentioned above.

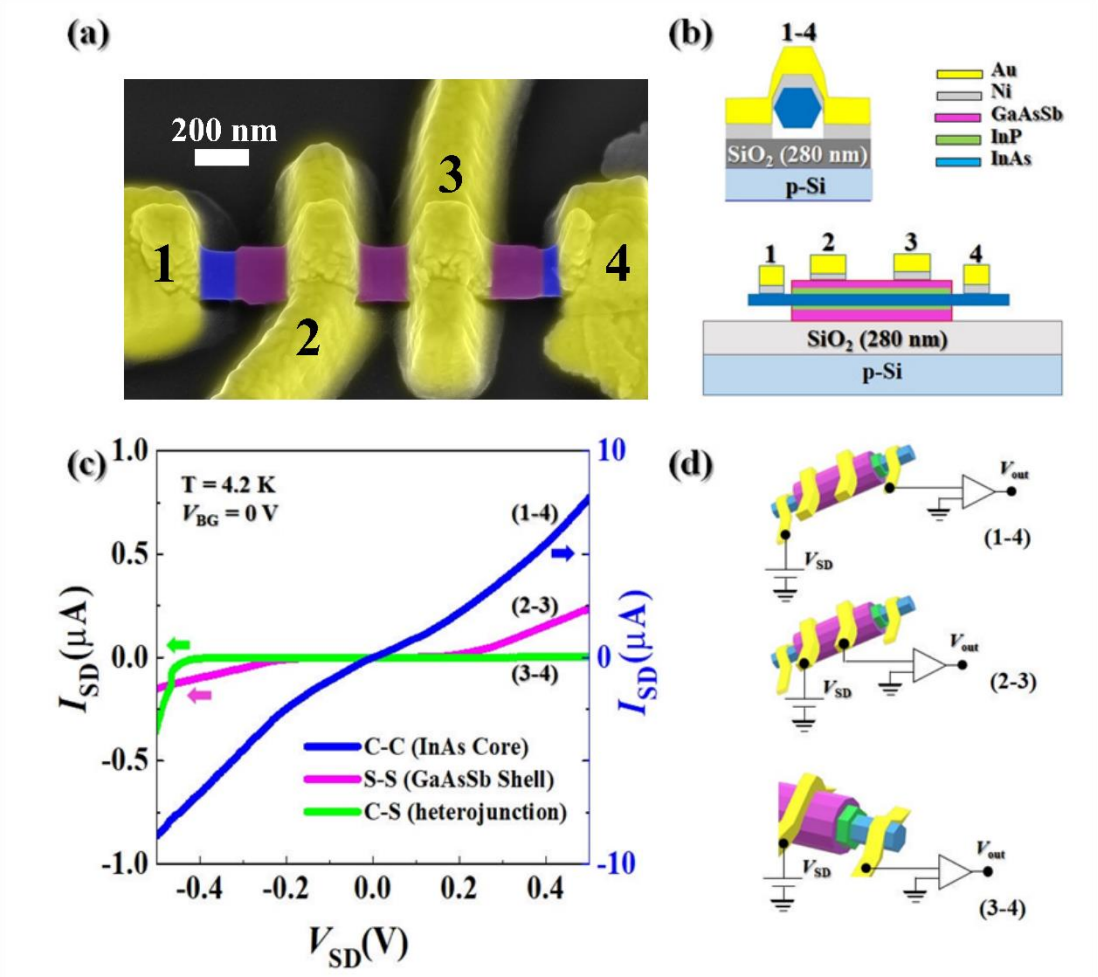

Figure 4.6. (a) SEM image of one of the investigated InAs/InP/GaAsSb CDS NW-based devices allowing measurements with multiple contact configurations in the same nanostructure. Purple, green, blue and yellow colors correspond to GaAsSb shell, InP barrier, InAs core and metallic electrodes, respectively. (b) Schematic of device architecture and a device cross-section. (c) *I-V* characteristics measured in the same nanostructure with different configurations, namely core-core (blue curve), shell-shell (pink curve) and core-shell (green curve), at V_{BG} = 0 V and at 4.2 K, the left y-scale corresponds to the S–S and C–S curves, while the right y-scale is related to the C–C curve. (d) Device architecture with circuit in overlay, corresponding to the three different configuration of measurement.

Figure 4.6 (c) reports three different *I-V* characteristics, measured at 4.2 K with applied V_{SD} in the range from -0.5 V to +0.5 V, in the same InAs/InP/GaAsSb CDS NW-based exploiting the three different measurement geometries enabled by our device architecture; the circuits corresponding to the different geometries are schematically depicted in Fig. 4.6 (d). The blue curve shown in Fig. 4.6 (c) was measured in the InAs core (C-C) using contacts 1-4 and displays a symmetric and

almost-linear behavior. It corresponds to a relatively low resistance (60 kΩ). The pink curve is measured in the GaAsSb shell (S-S configuration) using contacts 2-3, and in the linear region for $|V_{SD}| > 0.3$ V corresponds to a resistance of about 1 MΩ. The green curve is measured in C-S configuration using contacts 3-4 and it displays marked asymmetry as well as significantly higher resistance: in this configuration charge carriers must cross the insulating InP barrier.

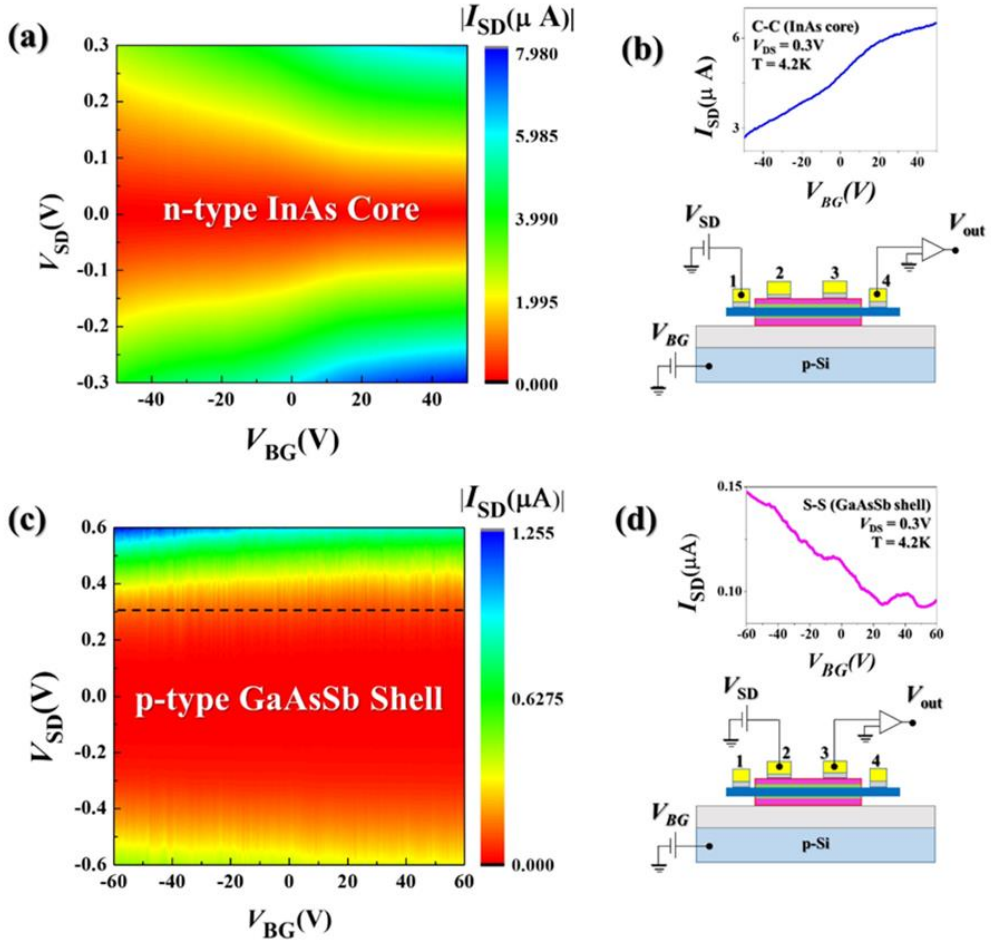

Figure 4.7. (a) Current map measured in the InAs core (C-C configuration) as a function of V_{BG} and V_{SD} at 4.2 K. (b-top) n-type transconductance curve extracted from the map in panel (a) for V_{SD} = 0.3 V. (b-bottom) schematic of the C-C measurement configuration. (c) Current map measured in the GaAsSb outer shell (S-S configuration) as a function of V_{BG} and V_{SD} at 4.2 K. (d-top) p-type transconductance curve extracted from the map in panel (c) for V_{SD} = 0.3 V. (d-bottom) schematic of the S-S measurement configuration.

The back-gate modulation of charge transport in the InAs core and in the GaAsSb shell is reported in Fig. 4.7, and clearly reveals that InAs is n-type while GaAsSb is p-type. Figure 4.7 panel (a) and (c) show two current maps measured at 4.2 K in the same InAs/InP/GaAsSb CDS NW-based device, respectively with C-C and S-S measurement configuration, as function of the V_{SD} and applied V_{BG}. The circuits

used to measure the two current maps in the two configurations are schematically depicted in Fig. 4.7 (b), (d). The InAs core clearly behaves as a n-type field effect transistor: its transconductance curve measured at V_{SD} = 0.3 V is reported in Fig. 4.7 (b)-top graph. The GaAsSb shell exhibits instead a behavior consistent with a p-type doping, as results from the transconductance curve measured at V_{SD} = 0.3 V reported in Fig. 4.7 (d)-top. Interestingly, the observation of almost linear I-V curves for the C-C configuration (with low electrical resistance at 4.2 K), together with the opposite behavior observed for C-C versus S-S configuration upon the application of V_{BG}, are consistent with the occurrence of good Ohmic contacts between the evaporated metals and the InAs semiconductor.

4.5 Conclusions

In conclusion, starting from catalyst-free InAs/InP/GaAsSb CDS NWs, we fabricated two-probe and four-probe electronic devices allowing to investigate the impact of InP barriers on the charge transport properties of the nanostructures. Measuring in shell-shell geometry, we showed that a 10 nm-thick InP barrier effectively suppressed the conduction band-to-valence band tunnelling between the InAs core and outer GaAsSb shell. Thanks to the four-terminal device architecture, in the same nanostructure we independently measured charge transport across the outer GaAsSb shell, the inner InAs core, and across the radial heterojunction. Our results obtained in C-S geometry proved that radial tunnelling across the InP barrier yielded asymmetric *I-V* curves and high electrical resistance, impressively larger respect to the resistance measured axially in the InAs core and in the GaAsSb shell of the NW. Moreover, field effect modulation of charge transport in our devices indicates n- and p-type nature of the InAs core and the GaAsSb shell, respectively. The present results demonstrate that a thin radial insulating barrier epitaxially grown between the n-type core and the p-type shell of a CDS NW efficiently quenches the tunnel coupling between electrons and holes located in the two axial channels. The InAs/InP/GaAsSb CDS NW-based device reported hereby behaves as a multifunctional device that allows for axial transport in two parallel semiconductor channels with opposite doping, together with radial transport across the two channels. This result suggests that our InAs/InP/GaAsSb CDS NW-based devices may represent a suitable platform for engineering Coulomb-coupled electron-hole systems in individual nanostructures.

Chapter 5: Self-catalyzed InAs/InSb axial heterostructured NWs

5.1 Introduction

Antimony based semiconductor materials are auspicious material for the study of fundamental phenomena and device applications. Among them, InSb is one of the promising material due to unique properties such as smallest band gap, smallest effective mass, the highest electron mobility, strong spin-orbit interaction, largest Landè g-factor, and the largest thermo-power figure of merit [127,166]. This makes InSb essential candidate for the various applications in the field of high speed electronics and optoelectronics [167,168]. Nevertheless, it is very hard to achieve epitaxial growth of InSb to the form thin film on common semiconductor substrates because of large lattice mismatch of InSb with other materials [169,170]. Therefore, to overcome this problem, it was grown in the form of NWs on lattice-mismatched substrates such as Si and InAs [171–178], which provides new path to grow InSb-based NWs. Recently, growth of InSb NWs is achieved on InSb substrates [179]. Despite development, it is absolutely hard to get to control over the morphology and dimensions of InSb NWs, and many fundamental aspects of their growth and related properties are not yet fully explored. For example, radial extension of the InSb segment can be caused by several reasons, such as the droplet inflation with either In or Sb atoms, or a rapid radial growth on the NW sidewalls, but the exact mechanism has not been revealed to our knowledge. So far, most efforts were put on the Au-assisted growth of InAs/InSb heterostructured NWs [171,173,174,176]. It is well known that the use of Au is not compatible with CMOS processing. The only remaining approach for the Au-free synthesis of InSb NWs on InAs stems should then be the self-catalyzed (or self-assisted) approach [180,181], in which the Au catalyst is replaced by In. To the best of our knowledge, only a few studies have been reported on self-catalyzed InAs/InSb NWs [172,182,183] and a detailed description of the growth mechanisms is still lacking. Consequently, we have performed the first systematic analysis of the self-catalyzed growth of InAs/InSb axial heterostructured NWs on silicon substrates. Our investigation shed new light on some general features of the growth mechanisms and the resulting properties of NWs.

The first section of this chapter will be dedicate to the growth of self-catalyzed InAs/InSb axial heterostructures NWs. The second part of this chapter is related to systematic analysis of the self-catalyzed growth of InAs/InSb axial heterostructured NWs through theoretical modelling. The theoretical modelling analyses were done in collaboration with Vladimir G. Dubrovskii (School of Photonics, ITMO University, Kronverkskiy St. Petersburg, Russia). The transmission electron microscopy measurements were performed on collaboration with Francesca Rossi (IMEM-CNR, Parma Italy). The results presented in this chapter are published in Ref. [184].

5.2 Growth Mechanisms of self-catalyzed InAs/InSb NWs

InAs/InSb axial heterostructured NWs were grown on Si (111) substrates. The MO precursors used for growth were trimethylindium (TMIn), tert-butylarsine (TBAs), and tris-dimethyl-aminoantimony (TDMASb). In the first step, stem of catalyst-free InAs NWs were grown via VS growth mode by using optimal parameters as described previously in chapter 3. The growth of InAs stem was carried out for 30 minutes with line pressure of TBAs = 3.0 Torr and TMIn = 0.3 Torr at 430 ± 5 °C. The average length and edge-to-edge diameter of InAs stem were 460 ± 50 nm and 60 ± 10 nm, respectively, with no tapering from the base to the top. In the second step, InSb segments were grown on these InAs NW stems. In order to study in detail, the growth mechanisms of InSb segment, different TMIn (F_{In}) and TDMASb (F_{Sb}) line pressures and time durations were investigated at a fixed growth temperature of 430 ± 5 °C. At the end of growth, the TMIn flux was stopped and the sample was cooled down to 150 °C in 3 min, linearly decreasing the TDMASb line pressure to 0 Torr.

5.2.1 Time evolution of the InSb segment under In-rich conditions

We first studied the evolution of the InSb segment as a function of its growth time *t*. In this series of samples, the line pressures F_{In} and F_{Sb} were fixed at 0.2 Torr and 0.35 Torr, respectively, while the growth times of InSb were varied (t = 10, 15, 20, 30, 45, 60, 120 and 180 minutes). The NW morphology was characterized by SEM in a Merlin field emission microscope operated at 5 keV. For imaging the NWs were mechanically transferred from the as-grown substrates onto a Si substrate, in order to measure the geometrical parameters (nanoparticle (NP) height and base radius, InSb segment length and diameter) from a 90° projection. SEM images of one representative NW from each sample are shown in Fig. 5.1 (a). The InAs/InSb interface is always well visible thanks to a larger diameter of the InSb segment. We performed EDX

analysis of the longest NWs (with t = 180 min). We did not find any Sb signal around the InAs stem and the InAs/InSb axial interface was quite sharp, corresponding to the position at which the NW diameter started to increase. Therefore, the InSb segment length can be measured directly from the SEM images as the distance from the InAs/InSb interface to the InSb/NP interface. A frozen In droplet (the NP) is always observable on top of InSb segment, clearly revealing the self-catalyzed VLS growth mechanism for InSb section. Accumulation of In on the NW top must be due to In-rich conditions during growth of InSb, as in Ref. [55,140], for In and Ga catalyzed InAs and GaAs NWs. We measured the following parameters for each sample (averaged over ~30 NWs): the maximum diameter of InSb segment $D = 2R$, with R as the radius of the segment, the length of InSb segment L, the base radius R_d and the height H of the NP, as described in panel (b) of Fig. 5.1.

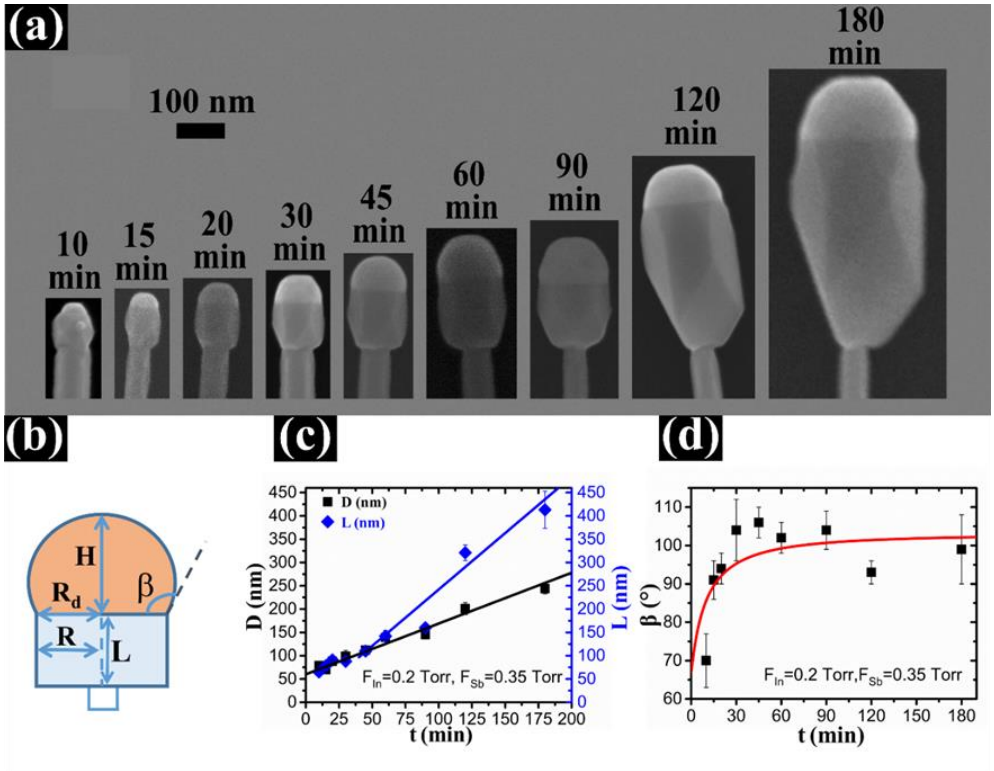

Figure 5.1. (a) Series of SEM images of InAs/InSb axial heterostructured NWs with In droplets on top, obtained with the line pressures F_{In} = 0.2 Torr and F_{Sb} = 0.35 Torr for different InSb growth times as indicated in each panel. The In droplet nucleates smaller than the NW facet, but then extends its base to cover the whole NW already after 15 min of InSb growth. (b) Schematic view of the measured geometrical parameters. (c) Time evolution of the diameter and length of InSb segments (symbols) and (d) time evolution of the contact angle of In droplets on top of InSb segments (symbols) of the sample series shown in (a). The lines in (c), and (d) are theoretical fits discussed in the modelling section.

All the average quantities with the standard deviation, for all the series of samples, are reported in the Table 5.1. The time evolution of the NP shape under these

growth conditions shows that it first appears smaller than the maximum InSb diameter due to tapering of the top NW section (after 10 min of InSb growth), but soon is pinned at the corners of vertical NW, with the aspect ratio (H/R_d) increasing toward longer times. The InSb segment length L and diameter D versus time t are shown in panel (c). We can see that both quantities increase with the growth time, but the InSb length increases faster than the diameter. Both length and diameter are approximately linear in time.

Table 5.1. Measured and calculated geometrical parameters for the time series reported in Fig. 5.1 (a): InSb segments grown under line pressures of F_{In} = 0.2 Torr and F_{Sb} = 0.35 Torr.

InSb growth time (min)	**R_d (nm)**	**H (nm)**	**NP aspect ratio (H/R_d)**	**β (Degree)**	**D (nm)**	**L (nm)**
10	26 ± 3	18 ± 3	0.69 ± 0.20	70 ± 7	79 ± 3	65 ± 5
15	29 ± 2	29 ± 3	1 ± 0.12	91 ± 5	70 ± 4	78 ± 6
20	41 ± 2	44 ± 3	1.07 ± 0.08	94 ± 4	88 ± 3	91 ± 4
30	45 ± 4	58 ± 8	1.28 ± 0.16	104 ± 8	99 ± 12	88 ± 10
45	54 ± 2	70 ± 4	1.29 ± 0.06	106 ± 4	112 ± 5	110 ± 10
60	66 ± 3	82 ± 5	1.24 ± 0.07	102 ± 4	139 ± 4	142 ± 12
90	70±3	90 ± 8	1.28 ± 0.09	104 ± 5	145 ± 7	160 ± 7
120	90 ± 6	94 ± 11	1.04 ± 0.13	93 ± 3	201 ± 13	321 ± 17
180	121 ± 4	142 ± 20	1.17 ± 0.14	99 ± 9	244 ± 11	413 ± 40

The contact angle can be obtained by assuming spherical cap shape of the NP resting on the NW top facet, and using the known expression $tan(\beta/2) = H/R_d$ [185]. This is a standard method of measuring the contact angle [186]. In order to verify that the droplet geometrical parameters measured ex-situ are representative of the actual droplet shape during growth, we carried out some cooling experiments with and without TDMASb flux and they will describe latter. The results confirm that the cooling down step does not affect the NW and droplet geometry, so the ex-situ measurements well reproduce the real shape and can safely be used for the β calculation. The plot of the contact angle versus time is shown in Fig. 5.1 (d). It is seen that the contact angle increases quite rapidly at the beginning but then saturates at 102 ± 2°.

5.2.2 Time evolution of the InSb segment under Sb-rich conditions

Next, we investigated the morphological evolution of InSb segments using a less In-rich condition by increasing the F_{Sb} value from 0.35 Torr to 0.7 Torr and keeping the same F_{In} of 0.2 Torr. We grew three different samples with t = 30, 45 and 60 min, for which the representative SEM images are shown in Fig. 5.2 (a).

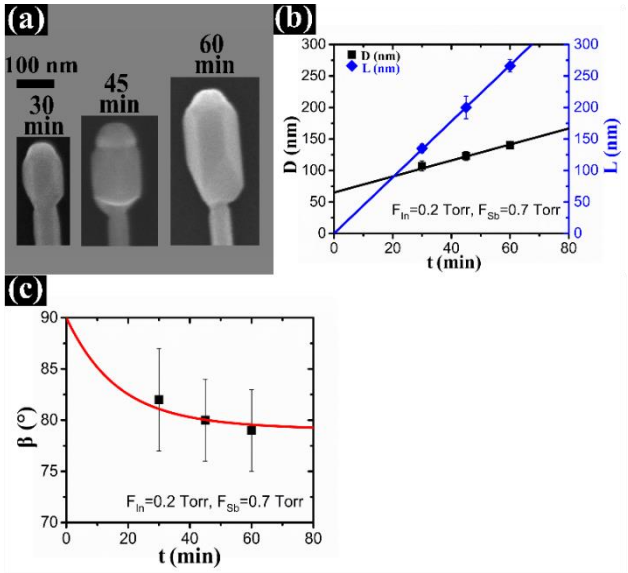

Figure 5.2. (a) Series of SEM images of InAs/InSb axial heterostructured NWs with In droplets on top, obtained under F_{In} = 0.2 Torr and F_{Sb} = 0.70 Torr for 30, 45, and 60 min of InSb growth time. The droplet diameter appears systematically smaller than the NW diameter. (b) Time evolution of the diameter and length of InSb segments (symbols) and (c) time evolution of the contact angle of In droplets on top of InSb segments (symbols) of the sample series shown in (a). The lines in (b), and (c) are theoretical fits discussed in the modelling section.

Figure 5.2 (b) shows the measured diameter and length of InSb segments as a function of the growth time. It is seen that the droplet is always smaller than the

maximum NW diameter due to tapering of the NW top. Furthermore, the droplet diameter stays almost constant during growth, while the maximum InSb diameter increases linearly with time according to Fig. 5.2 (b). By measuring the aspect ratio of the NPs, we deduced their contact angle plotted in Fig. 5.2 (c). It is seen that for these growth conditions, the contact angle saturates at approximately 79 ± 4°. The detail of all the measured average quantities with the standard deviation, for all the series of samples, are tabulated in the Table 5.2.

Table 5.2. Measured and calculated geometrical parameters for the time series reported in Fig. 5.2 (a): InSb segments grown under line pressures of F_{In} = 0.2 Torr and F_{Sb} = 0.70 Torr.

InSb growth time (min)	**R_d (nm)**	**H (nm)**	**NP aspect ratio (H/R_d)**	**β (Degree)**	**D (nm)**	**L (nm)**
30	39 ± 2	34 ± 4	0.87 ± 0.12	82 ± 5	107 ± 8	135 ± 7
45	39 ± 2	36 ± 6	0.92 ± 0.17	80 ± 4	123 ± 7	200 ± 18
60	45 ± 3	35 ± 3	0.77 ± 0.10	79 ± 4	140 ± 4	266 ± 10

5.2.3 Influence of Sb flux on the InSb segment morphology

In this section, we studied the influence of the In/Sb line pressure ratio on the morphology of InSb segments. Figure 5.3 (a) shows the representative SEM images of a series of InAs/InSb NWs as a function of F_{Sb}, obtained by keeping F_{In} at 0.2 Torr and varying F_{Sb} from 0.35 Torr to 0.80 Torr. The InSb growth time was fixed to 60 min for all samples. It is clearly seen that the size of In droplets decreases and the length of InSb segment increases with increasing the TDMASb line pressure. For lower TDMASb pressures (F_{Sb} < 0.55 Torr), the droplet covers the whole top facet of InSb NW, while for higher TDMASb line pressures it becomes smaller than the facet. The maximum F_{Sb} at which the In droplet is preserved on the NW top equals 0.8 Torr.

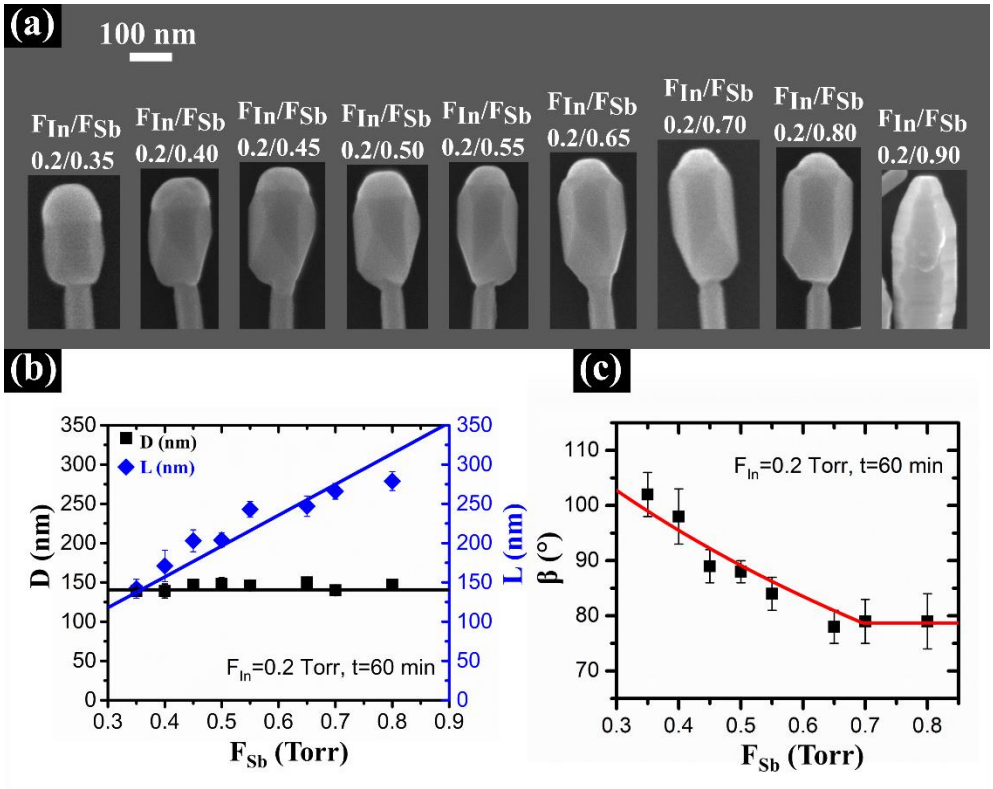

Figure 5.3. (a) Series of SEM images of InAs/InSb NWs, obtained after 60 min of InSb growth at a fixed F_{In} of 0.2 Torr and different F_{Sb}, yielding different In/Sb line pressure ratios as indicated in each panel. The droplets become smaller than the NW facet for higher F_{Sb}. (b) Diameter and length of InSb segment versus the F_{Sb} (symbols). (c) Contact angle of In droplets on top of InSb segments versus F_{Sb} (symbols). The lines in (b) and (c) are theoretical fits discussed in the modelling part. The change of the slope in the model fit comes from the minimum stable contact angle of 79°.

Higher TDMASb line pressure leads to a transition from the VLS growth to the catalyst-free VS growth mode, where no axial growth of InSb is observed. Instead, InSb starts forming a shell around the InAs stem. We can thus conclude that axial growth of InSb on InAs can only proceed in the presence of an In droplet through the VLS growth mode, while no axial growth occurs in the catalyst-free VS regime, as observed earlier in [187,188]. Figure 5.3 panel (b) shows the diameter and length of InSb segment as a function of F_{Sb}. It is seen that, while the In droplet size gradually decreases with increasing the TDMASb line pressure, the diameter of InSb segment remains constant. It clearly demonstrates that radial growth of InSb depends neither on the TDMASb line pressure nor on the In droplet size. Furthermore, the radial growth rate remains the same regardless of NW tapering at the top. Hence, radial growth should proceed independently of the VLS process occurring on the NW top. The length of InSb segment increases almost linearly with F_{Sb}, as usually observed in self-catalyzed III-V NWs [180,140,189]. By applying the same method as above, we

deduced the droplet contact angle as a function of F_{Sb}, shown in Fig. 5.3 (c). The contact angle gradually decreases with increasing the TDMASb line pressure. For lower pressures (F_{Sb} < 0.4 Torr), it remains larger than 90°, while for higher pressures (above ~0.65 Torr) it saturates at ~79°. The droplet volume further decreases by shrinking its base diameter smaller than the facet. All the measured quantities are reported in Table 5.3.

Table 5.3. Measured and calculated geometrical parameters for the samples reported in Fig. 5.3 (a): InAs/InSb NWs obtained keeping F_{In} at 0.2 Torr and varying F_{Sb} from 0.35 to 0.80 Torr.

F_{Sb} (Torr)	**R_d (nm)**	**H (nm)**	**NP aspect ratio (H/R_d)**	**β (Degree)**	**D (nm)**	**L (nm)**
0.35	66 ± 3	82 ± 5	1.24 ± 0.07	102 ± 4	139 ± 4	142 ± 12
0.40	65 ± 3	75 ± 6	1.15 ± 0.09	98 ± 5	139 ± 9	171 ± 20
0.45	62 ± 5	61 ± 6	0.98 ± 0.12	89 ± 3	147 ± 6	203 ± 14
0.50	61 ± 2	59 ± 3	0.96 ± 0.06	88 ± 2	148 ± 8	204 ± 9
0.55	54 ± 2	48 ± 3	0.88 ± 0.07	84 ± 3	146 ± 3	243 ± 10
0.65	53 ± 2	42 ± 3	0.79 ± 0.08	78 ± 3	150 ± 3	258 ± 20
0.70	45 ± 3	35 ± 3	0.77 ± 0.10	79 ± 4	140 ± 4	266 ± 10
0.80	42 ± 2	34 ± 4	0.80 ± 0.12	79 ± 5	147 ± 4	279 ± 15

When F_{Sb} is further increased to 0.9 Torr as described above discussion, a transition from the VLS growth to the catalyst-free VS growth mode (without any In droplet) occurs, and no more axial growth of InSb is observed. Instead, InSb starts forming a shell around the InAs stem, as we can see in the SEM image Fig. 5.3 (a).

5.2.4 Effect of In flux on the InSb segment morphology

In this section we will discuss the effect of group III (F_{In}) on the morphology of InSb segment of the InAs/InSb NWs. We grew a series of samples with same temperature and growth duration 60 min, keeping F_{Sb} fixed to 0.35 Torr while varying the F_{In} from 0.2 to 0.65 Torr. Figure 5.4 (a) shows a series of SEM images of

InAs/InSb NWs obtained by varying F_{In} from 0.2 Torr to 0.65 Torr at a fixed F_{Sb} of 0.35 Torr.

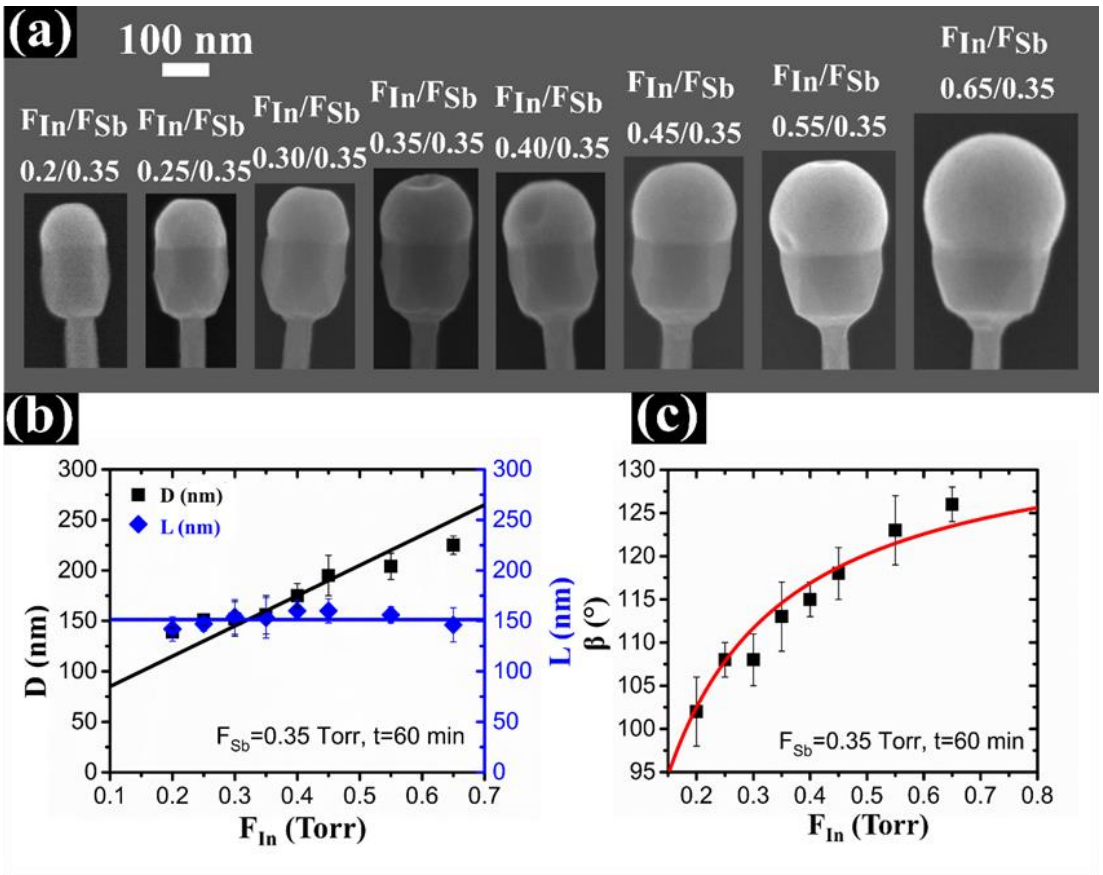

Figure 5.4. (a) Series of SEM images of InAs/InSb axial heterostructured NWs with In droplets on top, obtained after 60 min of InSb growth at a fixed F_{Sb} of 0.35 Torr and different F_{In}, yielding different Sb/In line pressure ratios indicated in each panel. Under these highly In-rich conditions, the In droplets always cover the whole NW facet. (b) Diameter and length of InSb segments versus the F_{In} (symbols). (c) Contact angle of In droplets on top of InSb segments versus F_{In} (symbols). The lines in (b) and (c) are theoretical fits discussed in the modelling section.

Clearly, all these growths proceed under highly In-rich conditions, where the volume of the In droplet gradually increases with increasing F_{In}. The In droplets cover the whole NW top facets in all cases. Figure 5.4 (b) shows the InSb diameter and length versus F_{In}. The diameter increases linearly with F_{In}, while the length is independent of F_{In}. We can thus conclude that the axial growth rate of InSb segment is independent of F_{In}, while the radial growth rate is proportional to F_{In}. Figure 5.4 (c) quantifies the droplet contact angle as a function of F_{In}, showing a rapid increase at the beginning but then showing a tendency for saturating at around 128 ± 2°. Further increase of the In droplet volume occurs by increasing the base radius. All the average quantities with the standard deviation, for all the series of samples, are summarized in the Table 5.4.

Table 5.4. Measured and calculated geometrical parameters for the samples reported in Fig. 5.4 (a): InAs/InSb NWs obtained keeping F_{Sb} at 0.35 Torr and varying F_{In} from 0.2 to 0.65 Torr.

F_{In} (Torr)	R_d (nm)	H (nm)	NP aspect ratio (H/R_d)	β (Degree)	D (nm)	L (nm)
0.2	66 ± 3	82 ± 5	1.24 ± 0.07	102 ± 4	139 ± 4	142 ± 12
0.25	73 ± 3	101 ± 5	1.38 ± 0.06	108 ± 2	151 ± 6	147 ± 7
0.30	72 ± 9	100 ± 12	1.38 ± 0.17	108 ± 3	152 ± 17	154 ± 17
0.35	77 ± 11	116 ± 16	1.50 ± 0.19	113 ± 4	156 ± 19	153 ± 20
0.40	87 ± 7	134 ± 20	1.54 ± 0.16	115 ± 2	175 ± 12	160 ± 10
0.45	96 ± 7	161 ± 10	1.67 ± 0.09	118 ± 3	195 ± 20	160 ± 12
0.55	102 ± 7	190 ± 13	1.86 ± 0.09	123 ± 4	204 ± 13	156 ± 8
0.65	117 ± 7	239 ± 8	2.04 ± 0.06	128 ± 2	225 ± 9	146 ± 17

5.2.5 Cooling down experiment

Additionally, in order to study the effect of the cooling process on the NW morphology and the droplet shape, we have grown two samples using the same parameters (F_{In}/F_{Sb} = 0.2/0.35 and 60 min growth time) but with different growth terminations. In the first case, the sample was cooled down to 150 °C in 3 min under TDMASb line pressure (as for all the other samples reported above, linearly decreasing the line pressure from 0.35 Torr to 0 Torr), while in the second case it was cooled down without any precursor flux. SEM micrographs of the NWs obtained are shown in Fig. 5.5. We measured the length and diameter of InSb segments and the contact angle of the droplets of ~ 30 NWs from each sample, following the same procedure described earlier. We found no difference between the two samples in terms of the NW length, diameter and contact angle of the droplet. We obtained L = 180 ± 10 nm, D = 162 ± 3 nm, and β = 104 ± 2° for the sample cooled down under TDMASb line pressure; and L = 190 ± 10 nm, D = 157 ± 3 nm, and β = 102 ± 2° for the sample cooled down without any flux. Therefore, we concluded that the cooling down process does

not affect the morphology of the InSb segment and the In droplet shape. This is reasonable considering that the axial growth will immediately decrease and probably stop during the cooling down step due to the lower temperature and the lower amount of Sb atoms available in vapor phase [190].

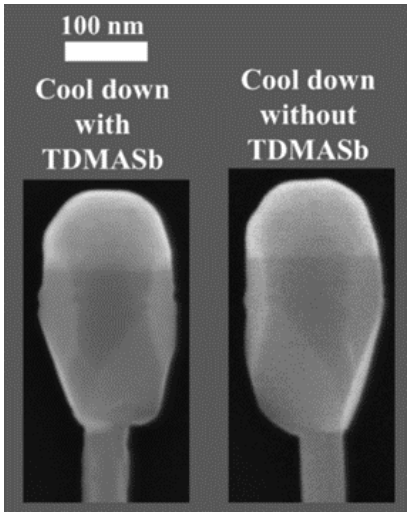

Figure 5.5. SEM images of InSb/InAs NW grown under F_{In} = 0.2 Torr and F_{Sb} = 0.35 Torr for 60 min and cooled down under TDMASb flux (left panel) and without TDMASb flux (right panel).

5.3 Crystal structure characterization

In order to study the crystal structure and the chemical composition of the grown InAs/InSb NWs, we performed TEM and EDX analyses of the InAs/InSb NWs grown under different conditions and obtained very similar results. Figure 5.6 shows two representative NWs from sample grown for 60 min at F_{In} = 0.2 Torr and F_{Sb} = 0.7 Torr. Panel (a) shows the EDX map of a NW, while panel (b) is a HR-TEM image. Panels (c) and (d) are the magnified views of the selected portions of the NW framed by the colored squares in (b), with the insets showing the FFT of the InSb lattice. In all the NWs analyzed, we found that the catalyst nanoparticles contain only In. The Sb concentration is always lower than 1%. From the HR-TEM and the FFT analyses, we found that the InAs stems have a mixed WZ/ZB crystal structure, while the InSb segments have the ZB structure with a few stacking faults, often followed by a thin WZ insertion at the NW top (close to the NW/NP interface). The TEM results confirm the self-catalyzed growth mechanism with pure In droplet on the NW top, as reported earlier in Refs. [177] and [42], and the good stability of the ZB crystal phase in InSb NWs.

.

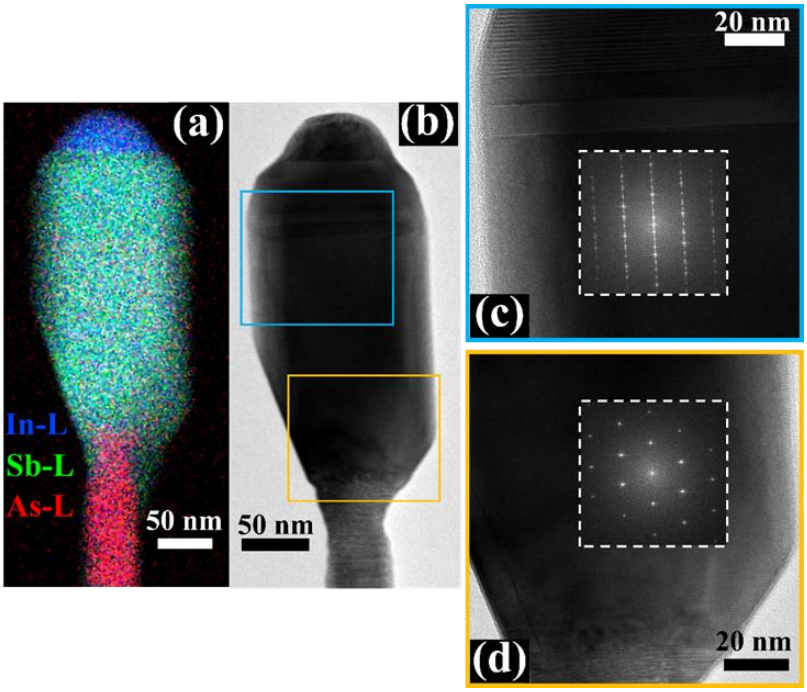

Figure 5.6. TEM analyses of the InAs/InSb NWs grown with F_{In} = 0.2 Torr and F_{Sb} = 0.7 Torr for 60 min. (a) EDX compositional map of a NW in which is visible the InAs stem in pink color, the InSb segment in green color and the In NP in blue. (b-d) show HR-TEM images with the FFTs of the selected portions (insets).

Next, we investigated the crystal structure of InAs/InSb NWs sample grown under F_{In} = 0.65 Torr and F_{Sb} = 0.35 Torr, for 60 min. Figure 5.7 shows HR-TEM images of InAs/InSb NWs. It is observed also for the NWs grown In-rich conditions from panel (b) that the crystal structure of the InSb segment is pure ZB with only a few stacking faults followed by a thin WZ portion close to the NW tip. The inset of panel (b) showed FFT of represented part of NWs which confirms the presence of pure ZB crystal structure of InAs/InSb NWs.

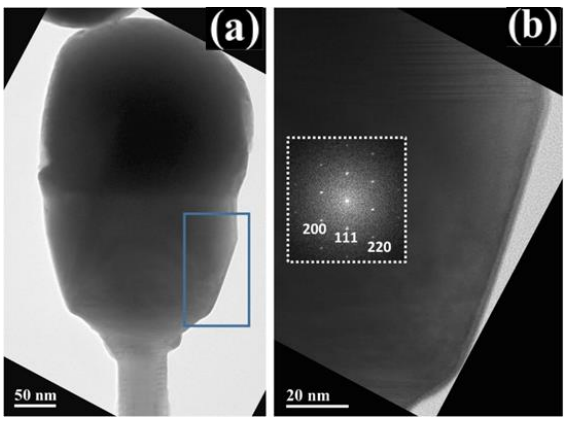

Figure 5.7. HR-TEM image of a NW obtained with F_{In}/F_{Sb} = 0.65/0.35 and t = 60 min: the whole NW (a) and the selected section (b) framed in (a). The inset in (b) shows the fast Fourier transform (FFT) of the image.

Further, we examined crystal structure of InAs/InSb NWs sample grown under the F_{In} = 0.20 Torr and F_{Sb} = 0.35 Torr for 60 min. The obtained results of InAs/InSb NWs are shown in Fig. 5.8. It is observed from HR-TEM image of panel (a) and magnified viewed of panel (b) that the crystal structure of the InSb segment is again pure ZB with only a few stacking faults followed by a thin WZ portion close to the NW tip.

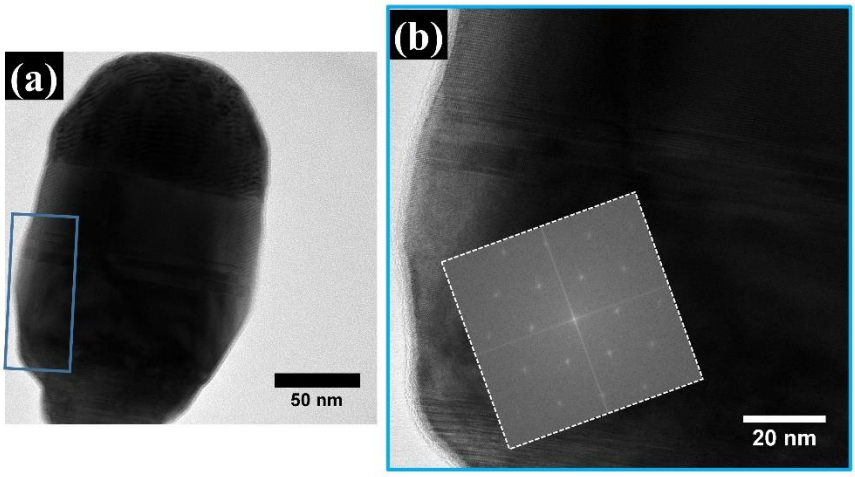

Figure 5.8. HR-TEM image of a NW obtained with F_{In}/F_{Sb} = 0.20/0.35 and t = 60 min: the whole NW (a) and the highlighted section (b) framed in (a). The inset in (b) shows the fast Fourier transform (FFT) of the image.

It is concluded from HR-TEM results that InSb segments consist of ZB crystal structure regardless of any growth conditions. We can explain this with following arguments that the crystal phase purity of InSb NW sections in the ZB structure from the surface energy point of view. We note that the difference between planar solid-vapor and solid-liquid facets for InSb $\gamma_{SV} - \gamma_{SL} =$ 0.0936 J/m^2 is quite small, corresponding to the Young's angle which is close to 90°. The Glas condition for the WZ phase formation [191], is given by $\gamma_{SV}^{l} - \gamma_{SL}^{l} - \gamma_{LV} \sin\beta < 0$, where γ_{SV}^{l} and γ_{SL}^{l} are the surface energies of the corresponding vertical facets. Assuming a small $\gamma_{SV}^{l} - \gamma_{SL}^{l}$, as for planar facets, the WZ phase seems to be always enabled around $\beta =$ 90°, as in our case. In fact, this observation was the original argument of Ref. [(Glas et al.) [191]], for the prevalence of the WZ phase in VLS III-V NWs. However, these considerations apply to vertical corner facets wetted by the droplet. It was then noticed that III-V NWs may grow with a truncated corner facets which makes nucleation of two-dimensional (2D) islands at the TPL improbable and hence the crystal phase of such truncated NWs should be ZB [192,193]. Therefore, being the ZB phase very

predominant in VLS InSb NWs in almost all cases, we speculate that InSb islands always nucleate with truncated lateral facets, as suggested in Ref. [194].

Furthermore, the nanoparticle (droplet) the composition for NWs taken from three different samples (grown under different In and Sb line pressure) were measured by EDX. The chemical composition of particle is mainly In. The results are summarized in the Table 5.5.

Table 5.5. Droplet chemical compositions measured by EDX

Growth parameters **InSb growth time (min)**	**Precursor line pressures (F_{In}/F_{Sb})**	**Composition of the droplet**	
		In (%)	**Sb (%)**
60	0.2/0.35	99.5	0.5
60	0.2/0.7	99.4	0.6
60	0.65/0.35	99.6	0.4

5.4 Modelling and discussion

The observed experimental results of InAs/InSb NWs will be explained and quantified here with the help of a dedicate theoretical model. The atomic In and Sb fluxes entering the droplet should be proportional to the TMIn and TDMASb line pressures, for the fixed pyrolysis efficiencies at a given growth temperature. This central assumption can be clarified by the following facts. Our data clearly show that the axial growth rate is approximately proportional to F_{Sb}, as demonstrated in Fig. 5.3 (b). This is standard phenomena for self-catalyzed VLS growth [180,189,195–197] and occurs because the catalyst droplet serves as a reservoir of group III atoms (In in our case) and the VLS growth conditions are always group V limited. Including the re-emitted flux of group V atoms scattered from the substrate surface or the neighboring NWs [189] does not change the linear scaling of the axial growth rate with group V flux. On the other hand, group V species are not diffusive on the NW sidewalls [189,195,196]. Conversely, VS growth on the NW sidewalls is usually group III limited [181,188,195,197] and may involve surface diffusion of In adatoms. This would not change the linear scaling of the average NW diameter with group III flux, clearly demonstrated in Fig. 5.4 (b). Diffusivity of In on Si (111) surface might be

high, but we consider growth of InSb on InAs at a distance ~500 nm from the substrate. Surface diffusion of In is known to not strongly affect even the Au-catalyzed CBE growth of InAs NWs, which is evidenced by their Poissonian length distributions [198]. When the VLS growth is driven by surface diffusion, the NW length distributions become much broader, with the variance scaling as the squared mean length [199] (against the linear scaling in the Poissonian case [198]). Finally, we are dealing only with the average values of the InSb segment length, diameter, and In droplet angle. In this case, it seems reasonable to assume a linear scaling of the growth rates with the corresponding fluxes, leaving aside more delicate effects of re-emission, surface diffusion and random nucleation of NWs on the surface [198]. Deviations from the linear fits, seen in Figures 5.1 (c), 5.3 (b) and 5.4 (b), might be due to the effects listed above.

We have observed from experimental results that the In droplets cover the whole top facets of InSb NWs at any In/Sb ratio. However, higher In/Sb ratios yield vertical or even slightly inverse-tapered InSb NWs, such as shown in Fig. 5.1 (a) and 5.4 (a), whereas lower In/Sb ratios lead to tapered NW tops, such as seen in Fig. 5.3 (a) and 5.6 (a)-(b). Tapered NWs maintain a fixed contact angle of In droplet of ~79° until the transition from the VLS to VS growth regime at F_{In}/F_{Sb} = 0.2/0.9. The two typical geometries are demonstrated in Fig. 5.9 and can be understood on surface energetic grounds similarly to other III-V NWs.

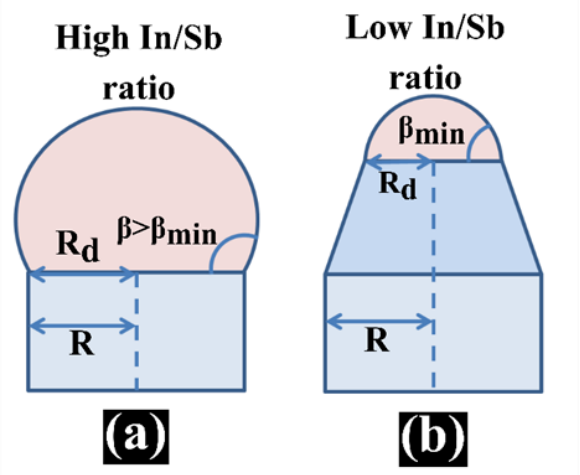

Figure 5.9 Illustration of (a) vertical (for $\beta > \beta_{min}$) or (b) tapered (at $\beta = \beta_{min}$) NW geometry, with $\beta_{min} \cong 79°$ as the small stable angle determined by the surface energetics.

It is reported previously, in-situ [186] and ex-situ [195] growth studies of self-catalyzed GaAs NWs show the bistability of the Ga droplet angle, with the two stable

angles around 90° and 130°. Inside this range, NWs grow with vertical sidewalls, while they taper at the small or inverse-taper at the large stable contact angle. Similar behavior is observed for self-catalyzed GaP NWs, with the vertical growth region shrinking to a narrow range around 123° [197]. In our case, we have determined the small stable contact angle of In droplets ~ 79°. The large stable contact angle is around 125-130° according to Fig. 5.4 (c). Clearly, the large stable contact angle corresponds to very high In/Sb ratios and is rarely achieved in our experiments. Conversely, the small stable contact angle is systematically observed, and determines the minimum In/Sb ratio at which InSb NWs can be grown in the VLS mode. Therefore, the two geometries shown in Fig. 5.9 will be used for modelling.

5.4.1 Radial and axial growth rate dependence

The VLS growth on the NW top occurring at the liquid-solid interface must be faster than the VS growth without any droplet. Therefore, the axial growth of InSb is mediated by nucleation of InSb islands under the droplet, even if it is smaller than the maximum NW diameter. This explains why maintaining the droplet is crucial for the formation of axial InAs/InSb NW heterostructures. Without any droplet, InSb tends to surround the InAs stem and forms a CS structure [188].

As discussed above, InSb segments grown on top of the InAs stems show the maximum radius increasing linearly with time, as demonstrated by Fig. 5.1 (c) and 5.2 (b). The measured content of Sb in the droplet is always negligible, and hence the droplet volume is controlled by the amount of In rather than Sb. The radial growth rate of InSb is independent of the TDMASb line pressure as shown in Fig. 5.3 (b) and it is proportional to the TMIn line pressure as observed in Fig. 5.4 (b). It is remarkable that the radial growth rate is exactly identical for different contact angles of the In droplets and even the NW configurations (vertical or tapered). Linear fits for the time and F_{In} dependences of the In-limited radial growth rates of InSb, shown in Fig. 5.1 (c), 5.2 (b) and 5.4 (b), respectively, yield:

$$\frac{dR}{dt} = a_{In}F_{In} \tag{5.1}$$

with $a_{In}F_{In} = 0.57 \pm 0.07$ nm/min at F_{In} = 0.2 Torr. Integration gives $R = R_0 + a_{In}F_{In}t$, with $R_0 \approx 30 \pm 5$ nm as the initial radius of InAs stems. This matches exactly the horizontal line in Fig. 5.3 (b) at t = 60 min. Therefore, radial growth of InSb

segments proceeds in the VS mode and has nothing to do with the droplet size evolution, in sharp contrast with Refs. [140], [196], and [200].

On the contrary, the axial growth rate of InSb segments is independent of the TMIn line pressure and is proportional to the TDMASb line pressure as plotted in Fig. 5.3 (b). According to Fig. 5.1 (c) and 5.2 (b) the NW length becomes a linear function of time after 30 min of growth. For shorter growth times, instead, the increase of length with *t* is slightly super-linear. This could be an effect of an overestimation of the InSb length at the beginning of the growth because of the InSb deposition on the tilted facets of the InAs stem NW tip, instead of the flat (111) top-facet as displayed in Fig. 5.10.

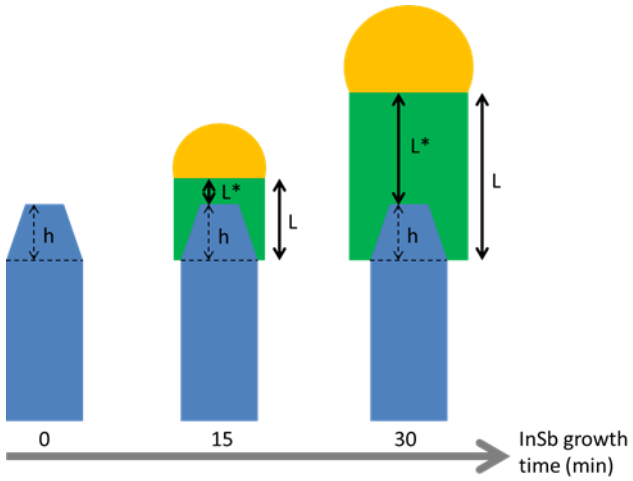

Figure 5.10. Schematic representation of the early stages of InSb growth. The measured InSb segment length (*L*) is overestimated compared to the real axial segment length (*L**) due to the InSb radial growth on the inclined facets of the InAs stem tip that results in a wrong InAs/InSb horizontal interface positioning.

As known from previously reported TEM analysis of the catalyst-free InAs NWs [66], the NW tip is not perfectly flat, showing instead some inclined facets, resulting in a tapered tip terminating with the flat (111) top facet. The tapered InAs tip shape is also visible in the EDX map of our InAs/InSb NWs of Fig. 5.6 (a). However, when we perform SEM imaging if the InAs/InSb NWs, the tapered InAs tip is not visible anymore, suggesting that InSb growth occurs also on the inclined facets of the InAs stem, burying the tapered InAs tip. Indeed, when we measure the InSb segment length (*L*), we take the InAs/InSb interface as the point at which we see the increase of the NW diameter. Therefore, *L* can differ from the actual InSb axial segment length (*L**), and this will result in an overestimation of the segment length, which is more relevant for short growth times. Figure 5.10 schematically explains this effect: the measured parameter *L* is given by the actual axial segment length *L** plus the height of the

tapered InAs tip (h). Since the latter is around 30-40 nm (as measured from the EDX maps), the overestimation of L is more relevant for short growth times ($t \leq 30$ min).

Furthermore, geometrical effects in directional CBE technique [201], may affect the early stage growth rate. Generally, the axial growth rate of self-catalyzed III-V NWs is proportional to the group V flux [140,180,181,195,196,198,200], however, the slope may depend on the droplet contact angle. Therefore, we can write:

$$\frac{dL}{dt} = b_{Sb}(\beta)F_{Sb} \tag{5.2}$$

with a β-dependent b_{Sb} in the general case (measured in nm/min × Torr). After the contact angle saturates to a certain β_c, as in Fig. 5.1 (d), the axial growth rate becomes independent of β and hence on the In flux. In particular, from the linear fits shown in Fig. 5.1 (c) and 5.2 (b), the axial growth rate is almost precisely doubled (4.5 ± 0.2 nm/min against 2.4 ± 0.12 nm/min) by increasing F_{Sb} from 0.35 Torr to 0.7 Torr.

5.4.2 The evolution of the droplet shape as a function of time and material fluxes

In order to describe the evolution of the droplet shape as a function of time and material fluxes, we note that the contact angle changes due to the two independent processes.

(1) On one hand, the contact angle of a droplet pinned at the NW corners decreases due to the radial growth on the NW sidewalls. We use the circular geometry for the NW top facet and spherical cup droplet shape. Then, whenever the NW radius increases by dR, the β decreases by $d\beta = -f(\beta)(1+\cos\beta)^2 dR/R$, with $f(\beta) = (1-\cos\beta)(2+\cos\beta)/[(1+\cos\beta)\sin\beta]$ as the geometrical function relating the droplet volume V to the cube of its base according to $V = (\pi R^3/3)f(\beta)$ [202]. Using Equation (5.1), this gives following relation,

$$(d\beta/dt)_1 = -f(\beta)(1+\cos\beta)^2 a_{In}F_{In}/R \tag{5.3}$$

(2) On the other hand, the contact angle changes due to any unbalanced In income from vapor and its sink due to the VLS growth of InSb NW section. In atoms should not desorb either from the droplet or the NW surface at 430 °C. Assuming also the absence of surface diffusion of In adatoms on the NW sidewalls [178,198], the total number of In atoms in the droplet N_{In} changes according to following equation,

$$dN_{In}/dt = (\pi R^2/\Omega_{InSb})[b_{In}(\beta)F_{In} - b_{Sb}(\beta)F_{Sb}] \tag{5.4}$$

Here, $b_{In}(\beta)$ is a β-dependent adsorption coefficient on the droplet surface for In similar to the one in Equation (5.2) for Sb, and $\Omega_{InSb} = 0.0680$ nm^3 is the elementary volume of InSb pair in ZB InSb [197]. Since the droplet contains only In atoms, we can write the corresponding change in the droplet volume, which equals $\Omega_{In} N_{In}$ (where $\Omega_{In} = 0.0261$ nm^3 is the elementary volume of liquid In) [197]. At a fixed R, we can present the volume change solely through $d\beta$ according to [202],

$$\boldsymbol{dN_{In}/dt = (\pi R^3/\Omega_{In})(1+\cos\beta)^{-2}(d\beta/dt)_2} \quad (5.5)$$

Equating these two expressions of equations (5.4) and (5.5), we obtain the contact angle change due to the In/Sb influx imbalance in the form of,

$$\boldsymbol{(d\beta/dt)_2 = (\Omega_{In}/\Omega_{InSb})(1+\cos\beta)^2[b_{In}(\beta)F_{In} - b_{Sb}(\beta)F_{Sb}]/R} \quad (5.6)$$

Therefore, the total change of the contact angle is given by combining the equations (5.3) and (5.6),

$$\boldsymbol{\frac{d\beta}{dt} = \frac{(1+\cos\beta)^2}{R_0 + a_{In}F_{In}t}\left[\frac{\Omega_{In}}{\Omega_{InSb}}(b_{In}(\beta)F_{In} - b_{Sb}(\beta)F_{Sb}) - f(\beta)a_{In}F_{In}\right]} \quad (5.7)$$

where we use the result of integration of Equation (5.1) for R in the denominator. Here, the first bracket term stands for the droplet shape evolution in the VLS process, similar to [203], while the second describes the decrease of the contact angle by In-limited VS radial growth on the NW sidewalls.

The stationary contact angle β_c is obtained from by considering the $\beta = \beta_c \cong$ constant

$$\boldsymbol{\frac{\Omega_{In}}{\Omega_{InSb}}(b_{In}(\beta_c)F_{In} - b_{Sb}(\beta_c)F_{Sb}) = f(\beta_c)a_{In}F_{In}} \quad (5.8)$$

provided that the left-hand side is positive. Of course, the small stable angle should be put to $\beta_{\min}$ if the solution to Equation (5.4) is smaller than $\beta_{\min}$, corresponding to the NW tapering as described above. Using the linear fits in Fig. 5.1 (d) at $\beta_c = \beta_* \cong 102°$, we obtain the unknown $b_{In}(\beta_*)F_{In}^*$, corresponding to these particular stationary contact angle and material fluxes. It is remarkable that our experimental data allow for the determination of the complete set of parameters describing the morphological evolution under these growth conditions, summarized in Table 5.6.

Table 5.6. Parameters describing the morphological evolution of InAs/InSb NWs and In droplets under F_{In} =0.2 Torr and F_{Sb} =0.35 Torr.

β_*	F_{In}^*	F_{Sb}^*	$a_{In}F_{In}^*$	$b_{Sb}(\beta_*)F_{Sb}^*$	$b_{In}(\beta_*)F_{In}^*$	$\Omega_{In}/\Omega_{InSb}$	A
Degree	**Torr**	**Torr**	**nm/min**	**nm/min**	**nm/min**		
102 ± 2	0.2	0.35	0.57 ± 0.07	2.4 ± 0.12	6.18 ± 0.05	0.384	0.534

Equation (5.7) describes the time evolution of the contact angle toward the stationary value determined by Equation (5.8). To simplify the analysis, we can expand the geometrical functions entering these equations in $\beta - \beta_*$ and keep only the linear terms: $b_k(\beta) \cong b_k(\beta_*) + b_k'(\beta_*)(\beta - \beta_*)$ for $k =$ In, Sb, and $f(\beta) \cong f(\beta_*) + f'(\beta_*)(\beta - \beta_*)$. Additionally, we account for a decrease of $(1 + cos\,\beta)^2$ in Equation (5.7) with increasing β by using a linear approximation. In the CBE system, beam angles of In and Sb with respect to the vertical equal to 38°. This allows us to find the constant $A = b_{In}'(\beta_*)/b_{In}(\beta_*) = b_{Sb}'(\beta_*)/b_{Sb}(\beta_*) \cong 0.534$ using the expressions for the geometrical factors of Ref. [201].

The final expressions for the droplet shape evolution contain no free parameters. The stationary contact angle is given by:

$$\boldsymbol{\beta_c = \beta_* + \frac{0.84(x - y)}{(1.45x + 0.84y)}} \tag{5.9}$$

for $\beta_c \geq \beta_{\min}$ and $\beta_c = \beta_{\min}$ otherwise, with $x = F_{In}/F_{In}^*$, $y = F_{Sb}/F_{Sb}^*$. The time evolution to this stationary state is described by:

$$\boldsymbol{\beta(t) = \frac{\beta_c(\beta_{max} - \beta_0) - \beta_{max}(\beta_c - \beta_0)(1 + t/\tau)^{-\delta}}{\beta_{max} - \beta_0 - (\beta_c - \beta_0)(1 + t/\tau)^{-\delta}}} \tag{5.10}$$

where:

$\delta = 4(\beta_{max} - \beta_c)\frac{(1.45x + 0.45y)}{x}$, $\tau = \frac{2R_0}{x}$.

and β_0 is the initial contact angle. Here, $\beta_{max} = 119^o$ for $\beta_c = \beta_* = 102^o$ at $x = y = 1$. We take $R_0 = 30 \pm 5$ nm and $\beta_0 = 82 \pm 3^\circ$ to fit all the data shown in Fig. 5.1, 5.2, 5.3, and 5.4.

Without any free parameters, our model provides excellent fit to all the data. This includes linear time dependences of the radius and length of InSb sections, linear scaling of *R* with the In line pressure and *L* with the Sb line pressure, non-linear time evolution of the contact angle to a flux-dependent stationary values (Fig. 5.1 (d) and 5.2 (c)), increase of the stationary contact angle with the In flux (Fig. 5.4 (c)) and its decrease with the Sb flux (Fig. 5.3(c)), and the NW tapering at the small stable contact angle. Overall, the achieved quantitative correlation of the model with the data is quite remarkable.

5.5 Conclusions

In conclusion, our study of self-catalyzed InAs/InSb axial heterostructured NWs exhibits some general features, which should relate to a wide range of epitaxial techniques and growth conditions. We have demonstrated that rapid radial growth of InSb is not a consequence of the droplet inflation but is rather due to the VS radial growth on the NW sidewalls so that In droplet may shrink and the whole NW extend. The presence of an In droplet on the NW top is absolutely required to maintain the axial growth of heterostructure. The growth kinetics of InSb NW sections as well as In droplets on their tops have been explained and quantified within a model containing no free parameters. More complex kinetic effects and local fluctuations of the material fluxes requires a separate study. Most importantly, our established model for the InSb morphology, which uses only the experimentally extracted parameters and fits quite well to all the data in a wide range of In/Sb ratios. While the growth geometry and critical values of the material fluxes may depend on a particular growth technique, the obtained results should be useful for engineering the morphology and the resulting properties of Au-free InAs/InSb axial heterostructured NWs for different applications.

Chapter 6: Self-catalyzed InSb/InAs quantum dot NWs

6.1 Introduction

NW-based HSs provide a wide range of opportunities for bandgap engineering by combining different materials [94]. As an example, III-V semiconductor NWs with embedded QDs were realized and their integration in high performance devices for electronics and optoelectronics was demonstrated in the last years [93,95-97,204,205]. The fabrication of QDs in NWs offers additional features over Stranski-Krastanow (SK) QDs, providing a tool for single QD control. This is a very important property that allows for example the implementation of a single-photon source for quantum cryptography and quantum computing [206-208]. Moreover, QDs in NWs are usually grown along the NW axis and this ensures the maximum collection efficiency and the possibility of controlled coupling to a NW waveguide mode [207,208].

InSb/InAs HSs represent one of the most promising material system for optoelectronic devices operating in the middle infrared range [110]. The NW geometry offers a great platform for improving the InAs/InSb material system quality and the range of possible applications. However, the Au-assisted growth that is commonly employed for the NW growth presents some limitations in the growth of double HS NWs, such as graded interfaces and kinking. In fact, it is challenging to preserve the stability of the catalyst nanoparticles (NPs) during material interchange [54,152,209]. In the specific case of InAs/InSb HS NW, straight InAs segment above the InSb segment is difficult to obtain, likely because of the change of composition of the Au-In alloy NPs [210]. The straight growth of InAs axial segment was reported only above InAsSb segments up to intermediate antimony composition [210]. All these shortcomings can be overcome by embedding InSb QDs in catalyst-free or self-catalyzed InAs NWs. In this chapter for the first-time, we will discuss the successful growth of self-catalyzed InSb QDs embedded in InAs NWs (refereed as InSb/InAs QD NWs hereafter) on Si (111) substrates. A systematic study of the influence of the growth parameters on the morphology of such NWs is conducted. Radial and axial growth rates are investigated as a function of growth parameters in order to study the growth mechanisms and to obtain InSb QD with controlled morphology. The

transmission electron microscopy measurements were performed in collaboration with Francesca Rossi (IMEM-CNR, Parma Italy). The results presented in this chapter are reported in Ref. [211].

6.2 Growth protocol of InSb/InAs QD NWs

InSb/InAs QD NWs were grown on Si (111) substrates. The following metal-MO precursors were used for the growth: trimethylindium (TMIn), tert-butylarsine (TBAs), and tris-dimethyl-aminoantimony (TDMASb). The growth protocol consisted of three steps. In the first step, catalyst-free InAs NW stems were grown via the VS growth mechanism on Si (111). The complete description of substrate preparation and growth protocols are described in chapter 3. The growth of InAs stems was carried out for 30 minutes with the growth parameters previously optimized for the InAs/InSb axial NW heterostructured growth, i.e. line pressures of TBAs (F_{As}) = 3.0 Torr and TMIn (F_{In}) = 0.2 Torr, and growth temperature of 410 ± 5 °C. The average length (L_{stem}) and edge-to-edge diameter (D_{stem}) of the InAs NW stems were 360 ± 21 nm and 50 ± 4 nm, respectively. In the second step, In-assisted VLS InSb QDs were grown on top of these InAs NW stems [184] after a direct switch of the precursor fluxes, without any growth interruption. The InSb QDs were grown for 5 minutes with line pressures of TDMASb (F_{Sb}) = 0.35 Torr and F_{In} = 0.6 Torr at same growth temperature of the InAs stems (410 ± 5 °C). The measured average length (L_{QD}) and edge-to-edge diameter (D_{QD}) of the InSb QDs were 40 ± 5 nm and 70 ± 4 nm, respectively. The contact angle β of the In NP on their tip was 118 ± 3° due to In-rich condition. Indeed, we chose these values of F_{In} (0.60 Torr) and F_{Sb} (0.35 Torr) based on our previous study of self-catalyzed InAs/InSb NWs as described in chapter 5, in order to provide stable conditions for the In droplet and the InSb QD shape and size, before the growth of InAs top segment. In the third step, the growth of InAs top segments was performed: at the end of the InSb QD growth, both TMIn and TDMASb fluxes were simultaneously interrupted and the growth temperature for the InAs top segment was adjusted in 3 min. At this point the growth of InAs top segment was started by opening the TMIn and TBAs lines with previously adjusted line pressures. In order to study the morphology and to explore the growth mechanisms (VLS or VS) of the InAs top segments, three different series of samples were grown as a function of growth temperature, MO line pressures, and time duration. At the end of growth, the F_{In} and F_{As} fluxes were stopped and the sample was cooled down to 150 ± 5 °C in 3 min, in

UHV conditions (i.e. without TBAs flux). For SEM imaging, the NWs were mechanically transferred from the as-grown substrates onto a Si substrate, in order to measure the different geometrical parameters from a 90° projection. Following this procedure, we could measure D_{QD} and L_{QD}, and these parameters at the end of the InAs top segment growth: the NW diameter specifically at the InSb QD position (D_{InSb}), the base diameter of the NWs (D_{bottom}), the total length of the NWs (L_{NWs}), the base radius (R), and the height (H) of the nanoparticle (NP). All these quantities were averaged over ~ 25 NWs for each batch. From these measured parameters we could calculate the NP volume (V_{NP}) and contact angle (β) [185,186], the InAs shell thickness around the InSb QD ($t_{shell} = (D_{InSb} - D_{QD})/2$), and the length of InAs top segment ($L_{top} = L_{NWs} - (L_{stem} + L_{QD})$).

6.3 Influence of growth parameters on the morphology of the InAs top segment

6.3.1 InAs growth temperature series

Initially, we studied the influence of the growth temperature (T_{InAs}) on the evolution of InAs top segment. In this set of experiments, the line pressures of 0.3 Torr and 0.25 Torr for F_{In} and F_{As} respectively, and the growth time of 15 min were kept constant, while the growth temperature of top InAs was varied (T_{InAs} = 320, 350, 380, 410, 430, and 440 ± 5 °C). SEM images of one representative InSb/InAs QD NW from each sample are presented in Fig. 6.1 (a). In the first red framed box, we show the InAs/InSb NW before the growth of InAs top segment. We can clearly see the In droplet on the top of NW, the InSb QD with larger diameter and the InAs stem with uniform diameter. The InSb QD shows the same kind of side facets of the InAs stem, (i.e. {110} [134,172]). The other NWs depicted in panel (a) are representative SEM images of InSb/InAs QD NWs where the InAs top segment was grown at different temperatures, T_{InAs}, as indicated in the figure. The presence of In NPs on the top of all NWs reveals a wide range of temperature window for the In-assisted InAs VLS growth. The InAs top segment grows with the same kind of side facets of InSb QD and InAs stem. In all samples, the NWs show the growth axis aligned with the <111> crystallographic direction and a straight, perpendicular NW/NP interface, except the sample grown at T_{InAs} = 320 ± 5 °C in which all NWs exhibits tilted NW/NP interface. This can be ascribed to the development of a more stable growth interface at this temperature, or to the instability of the droplet triggered by its larger volume [212,213].

We analyzed the In particle on the top of the NWs and we calculated its volume by considering it as a spherical cap having contact angle β and a base radius R. The NP volume is given by $V_{NP} = (\pi R^3/3)\, f(\beta)$, with $f(\beta) = [(1 - \cos\beta)\,(2 + \cos\beta)] / [(1 + \cos\beta)\,\sin\beta]$ [184]. The evolution of volume and β of the In NP as a function of T_{InAs} are plotted in Fig. 6.1 panel (b) and (c), respectively. It is observed from the plots that both volume and contact angle of In NP decrease with increasing growth temperature of InAs top segment.

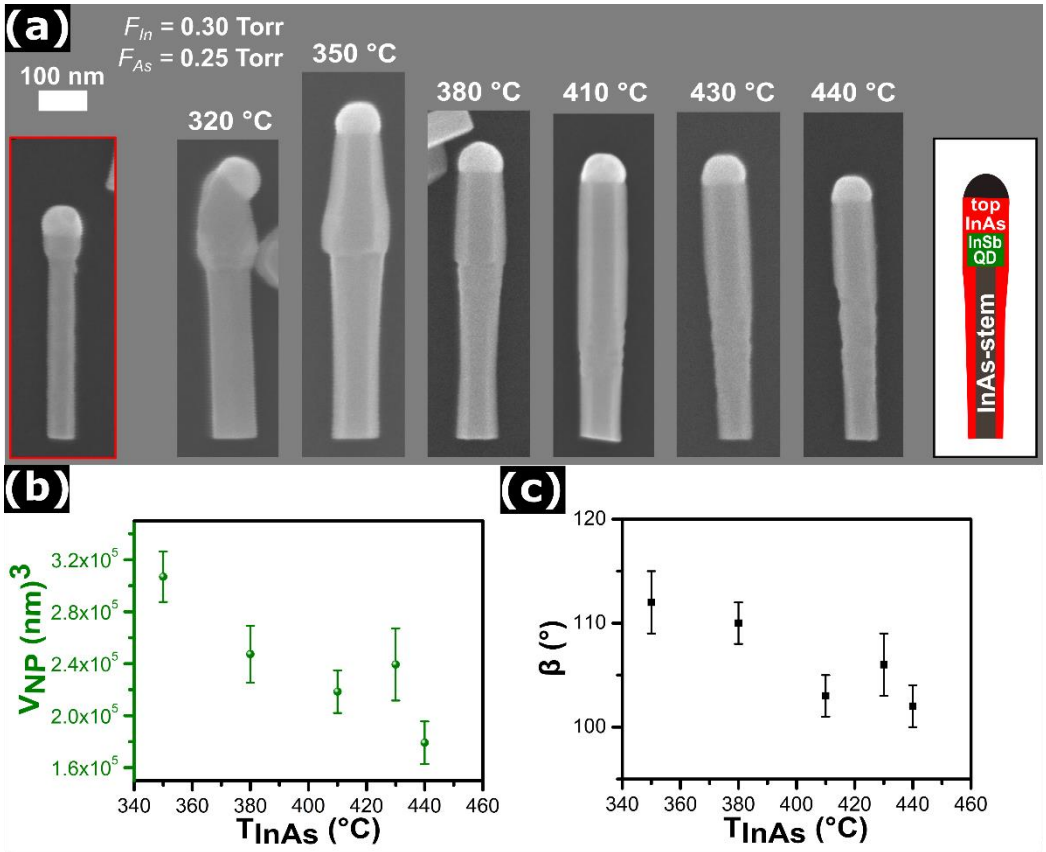

Figure 6.1. (a) Series of SEM images of the InSb/InAs QD NWs. The first NW shown in the red frame represents the InAs/InSb NW grown at 410 ± 5 °C. The other panels represent the InSb/InAs QD NWs where the InAs top segment has been grown with the line pressures F_{In} = 0.30 Torr and F_{As} = 0.25 Torr and growth time 15 min at different growth temperatures (T_{InAs}) as indicated in each panel. The drawing in the right side of the panel shows a schematic picture of the InSb/InAs QD NW structure. (b) Evolution of the NP volume as a function of T_{InAs}. (c) Evolution of contact angle (β) of the In NPs on the top of NWs as a function of T_{InAs}. The symbols represent an average value of each sample obtained by measuring ~ 25 NWs and error bars represent the standard deviation of the average.

The other measured parameters, as D_{InSb}, D_{bottom}, L_{NWs}, as a function T_{InAs} are described in Fig. 6.2 panel (a) and (b), respectively. It is clearly seen from the graphs that both axial and radial growth (both around the InSb dot and the InAs stem) during the InAs top segment deposition decrease with increasing the growth temperature. Panel (c) of Fig. 6.2 shows instead the relationship between the InAs shell thickness

around the QD (t_{shell}) and T_{InAs}. Notably, the shell thickness decreases by increasing the growth temperature from 340 to 440 ± 5 °C. The minimum value of shell thickness of 9 ± 3 nm is achieved at 440 ± 5 °C. Finally, the dependence of the InAs top segment length (L_{top}) on T_{InAs} is shown in Fig. 6.2 panel (d). The longest InAs top segment with L_{top} (210 ± 19 nm) is obtained at T_{InAs} = 350 ± 5 °C then it decreases. The minimum value of L_{top} (81 ± 19 nm) is measured at T_{InAs} = 440 ± 5 °C. It should be mentioned that in most of the samples, the position of the InSb QD is easily localized by SEM images, thanks to its wider diameter. In the samples in which the InAs/InSb interface was not well visible, we used EDX at SEM to localize the InSb QD (following the drop of As signal in the elemental line profile) and then we measured the NW diameter at that position by SEM imaging.

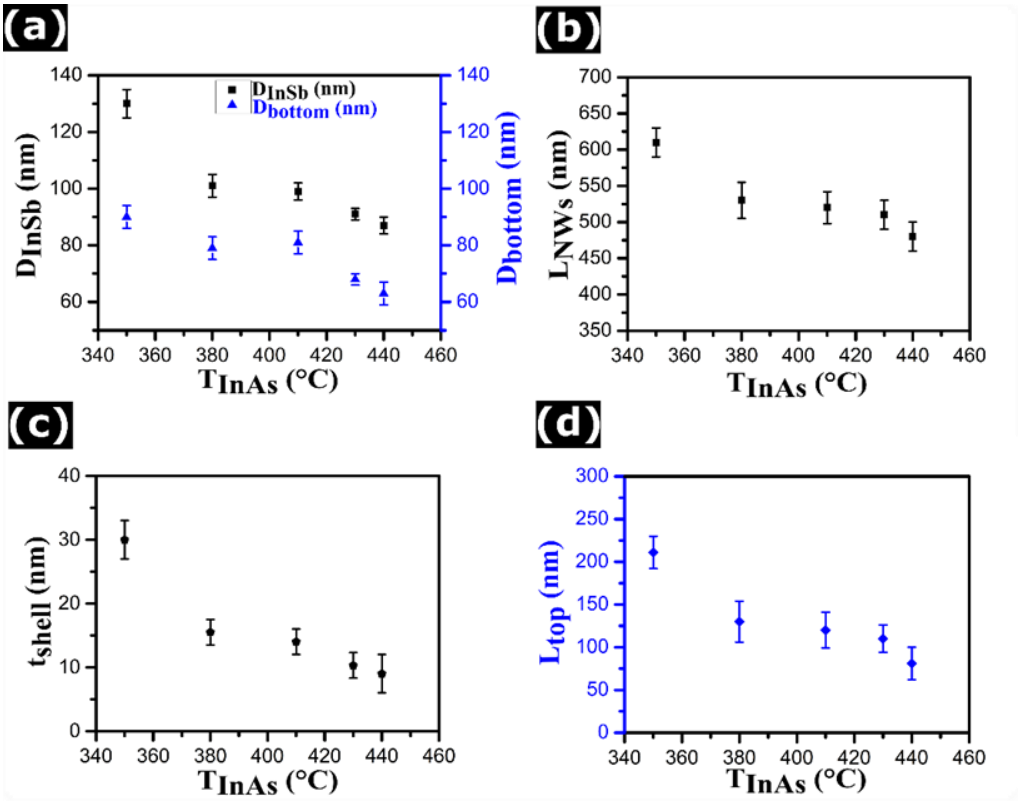

Figure 6.2. (a) Evolution of the diameter of NWs at the InSb QD and at the bottom of NWs versus T_{InAs}. (b) Evolution of total length of NWs (L_{NWs}) as a function of T_{InAs}. (c) Evolution of the InAs shell thickness as a function of T_{InAs} which represents the InAs radial growth around the InSb QD. (d) Evolution of length of InAs top segments (L_{top}) as a function of T_{InAs}. The symbols represent an average value of each sample obtained by measuring ~ 25 NWs and error bars represent the standard deviation of the average.

6.3.2 As line pressure series

In the second set of experiments, we selected T_{InAs} = 440 ± 5 °C, which was found to minimize the shell thickness around the InSb QD and we varied F_{As} from 0.20

Torr to 0.50 Torr. The growth time and F_{In} were set to 15 min and 0.30 Torr, respectively. Figure 6.3 (a) shows SEM images of representative NWs of this series of samples. First we observed that the NP volume decreases with increasing F_{As} and the NP base radius shrinks above 0.35 Torr, yielding pencil like shape of the NW tips. Then we noticed that the length of InAs segment increases with increasing F_{As} up to 0.40 Torr. For $F_{As} \geq 0.40$ Torr the length starts to decrease, moreover at 0.50 Torr there is no particle on the top of the NWs. It is well known in self-catalyzed growth that the group III particle starts to shrink with increasing group V flux and can be completely consumed in group V rich condition. The contact angle of the In droplet on the top of NWs as a function of F_{As} is plotted in panel (b) of Fig. 6.3. The contact angle slowly decreases with increasing F_{As} line pressure. It remains greater than 90° for $F_{As} < 0.35$ Torr, while for higher F_{As} it becomes smaller than 90°. The evolution of contact angle confirms the consumption of In NP with increasing F_{As}.

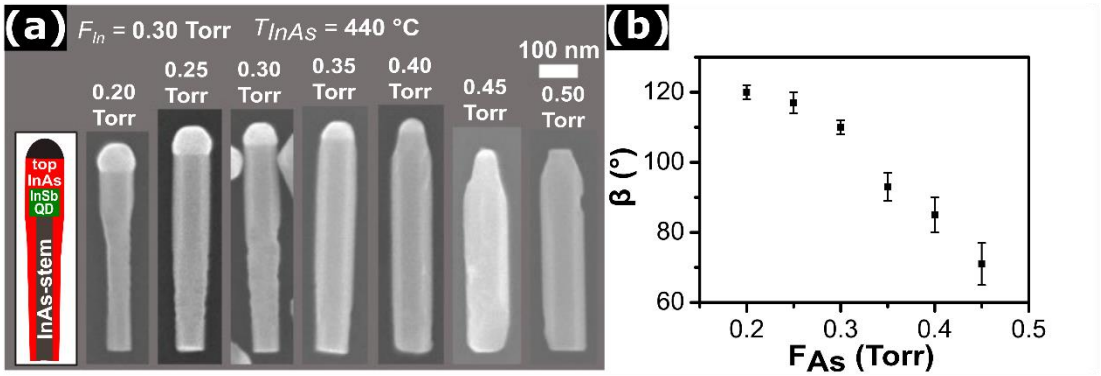

Figure 6.3. (a) SEM images of InSb/InAs QD NWs obtained with fixed line pressures F_{In} = 0.30 Torr, growth time 15 min and T_{InAs} = 440 ± 5 °C, while F_{As} varied from 0.20 Torr to 0.50 Torr as indicated in each panel. The droplet volume decreases with increasing F_{As} and finally there is no droplet in the sample grown with F_{As} 0.50 Torr. The drawing in the left side of the panel shows a schematic picture of the InSb/InAs QD NW structure. (b) Plot of contact angle (β) of In droplets versus F_{As}. The symbols represent an average value of each sample obtained by measuring ~ 25 NWs and error bars represent the standard deviation of the average.

Next, we calculated the effect of F_{As} on the evolution of the NW shape, i.e. on the radial and axial InAs growth. Both NW diameter around the QD and the base diameter increase with increasing F_{As} but with different slopes as shown in Fig. 6.4 (a) and this explains why for F_{As} = 0.50 Torr the NW diameter is uniform along the whole length. The values of InAs shell thickness around InSb QD as a function of F_{As} are extracted from D_{InSb} and plotted in Fig. 6.4 (c). It can be seen that the shell thickness increases with increasing F_{As}. This suggests that the radial growth of InAs around the InSb QD is As-limited and it is directly proportional to F_{As}. The possible explanation

is that the high As line pressure reduces the desorption rate of In adatoms [214,215]. Hence, the sticking probability of In adatoms on the NW sidewalls is enhanced at high F_{As}, which increases the radial growth rate of InAs. These findings are consistent with previously reported results in the case of self-catalyzed InAs [62] and GaAs NWs [180,216].

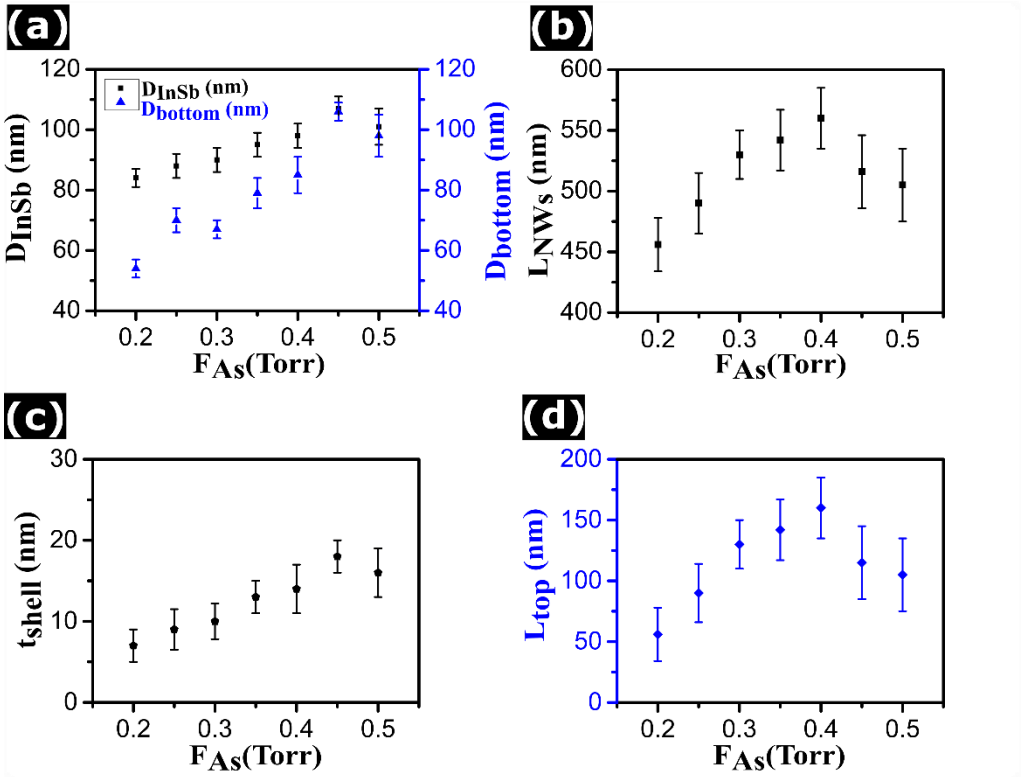

Figure 6.4. (a) Expansion of radial growth of the NWs at the InSb QD and at the bottom of NWs versus F_{As}. (b) Evolution of total length of NWs (L_{NWs}) as a function of F_{As}. (c) Evolution of shell thickness around the InSb QD versus F_{As}. (d) Evolution of length of top InAs segments (L_{top}) as a function of F_{As}. The symbols represent an average value of each sample obtained by measuring ~ 25 NWs and error bars represent the standard deviation of the average.

The influence of As line pressure on L_{NWs} is plotted in Fig. 6.4 (b), while L_{top} is shown in the Fig. 6.4 (d). For the length of InAs top segment, two distinct regions are observed. The axial growth rate increases with increasing As line pressure up to 0.40 Torr. Here it shows a maximum value of 160 ± 32 nm, and above 0.40 Torr L_{top} decreases. The decrement of L_{top} is ascribed to the consumption of the In NP on the top of NWs. Indeed, the axial growth mechanism of the NWs is VLS for As line pressure from 0.20 Torr to 0.4 Torr, and the axial growth rate is known to be directly proportional to the As flux in self- catalyzed InAs NWs [55]. At F_{As} = 0.45 Torr the In particle is still visible (still VLS growth mode) but its volume and contact angle are strongly reduced, explaining why the axial growth rate decreases. Finally, for As line

pressure higher than 0.45 Torr the growth mode becomes VS due to the absence of NP on the top of NWs and the axial growth rate drops.

6.3.3 Time series

In the last set of experiments, the time evolution of InAs top segment under In rich conditions was studied. In this series of samples, the line pressures of F_{In}, F_{As}, and growth temperature were kept constant at 0.30 Torr, 0.30 Torr, and 440 ± 5 °C, respectively, while the growth time of InAs top segments was varied as t = 5, 10, 15, 20, 30, and 45 min. The representative SEM images from each sample are shown in Fig. 6.5 panel (a). An In droplet is found on the top of all NWs, which is evidence of the self-catalyzed VLS growth mechanism persisting at any growth time. As clearly seen from the SEM images, the InAs top segment elongates axially and, at the same time, there is a shell growth along the whole NW length that occurs with different rates around the InSb QD and around the InAs stem. Indeed, after 20 min of growth time, the InAs/InSb interface is not visible anymore because the NW diameter is uniform from the bottom to the top.

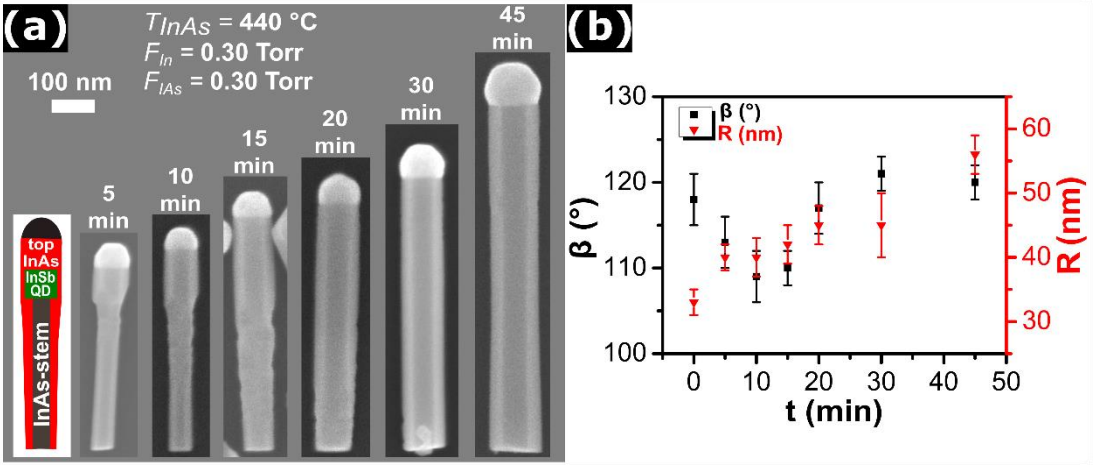

Figure 6.5. (a) SEM images of representative InSb/InAs QD NWs, obtained with fixed line pressures F_{In} = 0.30 Torr, F_{As} = 0.30 Torr, at T_{InAs} = 440 ± 5 °C, while the growth time of InAs top segments varies from 5 min to 45 min as indicated in each panel. The drawing in the left side of the panel shows a schematic picture of the InSb/InAs QD NW structure. (b) The evolution of contact angle of In droplets on the top of NWs and the base radius of NP as a function of growth time. The time t = 0 min is corresponding to the contact angle and base radius at the end of InSb segment growth. The symbols represent an average value of each sample obtained by measuring ~ 25 NWs and error bars represent the standard deviation of the average.

The evolution of the contact angle and base radius of the NP as a function of growth time are plotted in Fig. 6.5 panel (b). At zero time (representing the InAs/InSb NW as without any InAs top segment), the calculated values of the contact angle and

base radius are 118 ± 3° and 33 ± 2 nm, respectively. At the beginning of InAs top segment growth, for $0 < t < 15$ min, the contact angle decreases. This behavior is probably associated with an increment of the base radius of the NP/NW interface that is faster than the increase of NP size at the early growth stages [184,194,202]. Then, the contact angle slightly increases with the growth time and it stabilizes around 120 ± 3°.

We measured also D_{InSb}, D_{bottom}, and L_{NWs} as a function of the InAs top segment growth time. The corresponding values are plotted in Fig. 6.6 panel (a) and (b). The calculated InAs shell thickness around the InSb QD as a function of growth time is shown in Fig. 6.6 (c). The shell thickness increases linearly with increasing growth time. The growth rate of the InAs shell around the InSb QD can be derived from the slope of the linear fit of experimental data points. We obtain a radial growth rate of 0.46 ± 0.04 nm/min.

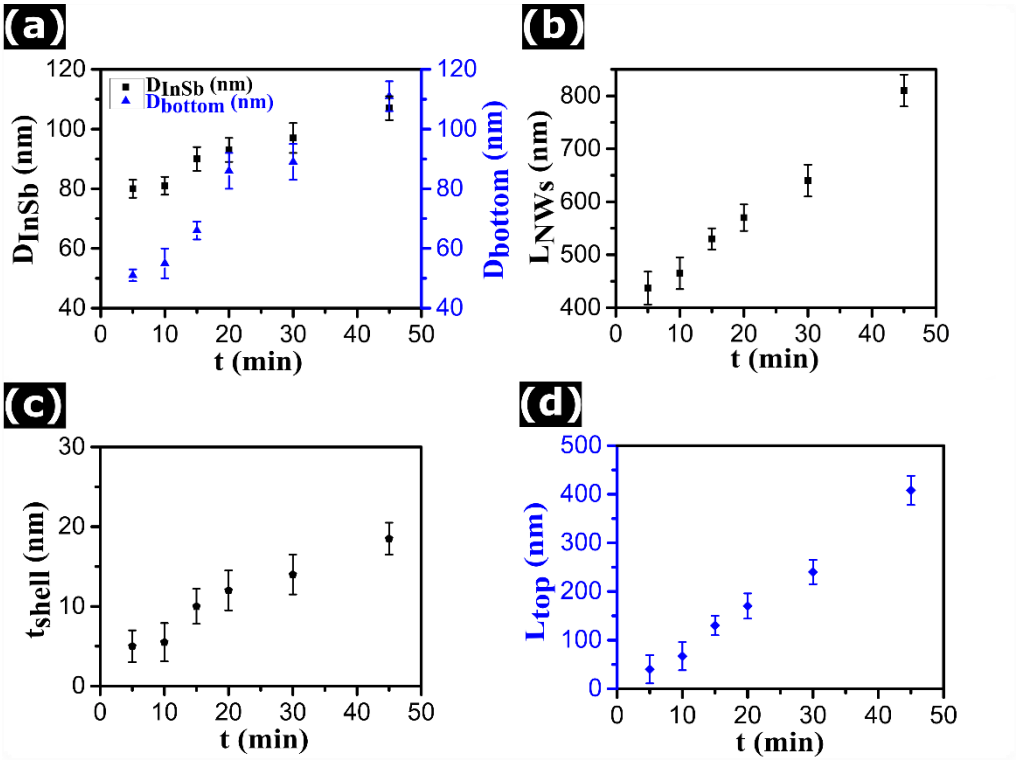

Figure 6.6. (a) Expansion of radial growth of the NWs at the InSb QD and at the bottom of NWs as a function of growth time. (b) Evolution of total length of NWs as a function of growth time. (c) Evolution of shell thickness of top InAs segments around the InSb QD as a function of growth time. (d) Evolution of length of InAs top segments as a function of growth time. The symbols represent an average value of each sample obtained by measuring ~ 25 NWs and error bars represent the standard deviation of the average.

The influence of growth time on the length of InAs top segments is plotted in Fig. 6.6 (d). Also in this case we observed that the length of InAs top segments

increases linearly with increasing growth time. We have not observed any delay or incubation time and saturation of NW length up to 45 min of growth time. The absence of incubation time is attributed to the In droplet already formed on top of the InSb segment. The axial growth rate can be obtained from the slope of the linear fit of experimental data points whose intercept passing through the origin. We obtain an axial growth rate of 8.60 ± 0.25 nm/min. The axial growth rate is much higher as compared to the radial growth rate, as typically observed in VLS versus VS growth. However, the length elongation is always accompanied by an expansion in diameter as commonly observed in self-catalyzed NW growth.

6.3.4 In NP consumption experiment

In order to better understand the InAs radial growth mechanisms, and explain why the growth rate is different around the InAs stem and the InSb QD, we conducted an additional experiment. The idea of this experiment was to partially consume the In NP on top of the InAs/InSb NWs in order to start the InAs top segment growth with a smaller NP. In this experiment, the InAs/InSb NWs were kept under the As line pressure of 1 Torr for 1 min at 410 ± 5 °C at the end of the InSb QD growth, to partially consume the In NP. Indeed, this procedure reduces the NP size and the contact angle β that previously was around 120° becomes smaller than 90°.

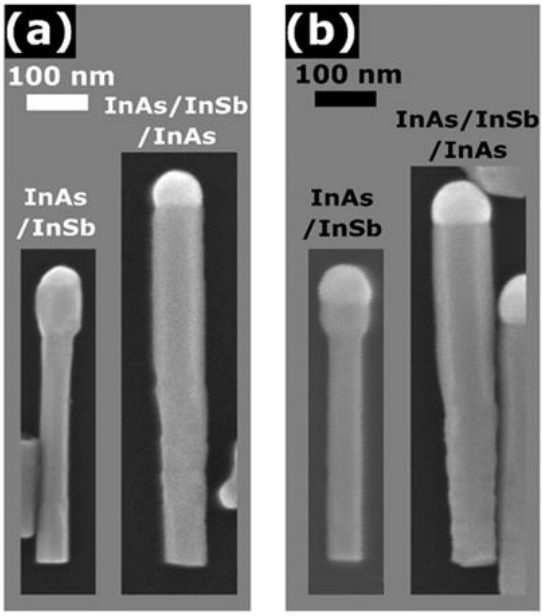

Figure 6.7. (a) SEM images of InAs/InSb heterostructured NW and InSb/InAs QD NWs, obtained with partial consumption of In NP under F_{As} = 1 Torr for 1 min. The growth of top InAs segment was performed with line pressures of F_{In} = 0.30 Torr F_{As} = 0.30 Torr, and growth time of 15 min at T_{InAs} = 440 °C. (b) SEM images of InAs/InSb heterostructured NW and InSb/InAs QD NWs, obtained without consumption of the In NP.

Subsequently, the growth of InAs top segment was carried out using the same growth condition: F_{In} = 0.30 Torr and F_{As} = 0.30 Torr for 15 min at T_{InAs} = 440 ± 5 °C. Figure 6.7 shows the SEM images of nanowires of the samples with (a) and without (b) consumption of the In NP, before (left) and after (right) the InAs top segment growth. All the measured parameters are listed in Table 6.1.

Table 6.1. Measured and calculated geometrical parameters for the samples reported in Fig. 6.7.

Type of growth	**Growth Conditions**	**R (nm)**	**H (nm)**	**β (°)**	**D_{Insb} (nm)**	**D_{bottom} (nm)**	**L_{NWs} (nm)**
InAs/InSb	Without In NP consumption	33 ± 2	54 ± 4	118 ± 3	70 ± 4	50 ± 4	400 ± 21
InAs/InSb	With In NP consumption	32 ± 2	31 ± 3	88 ± 5	75 ± 3	51 ± 3	460 ± 35
InAs/InSb /InAs	Without In NP consumption	44 ± 2	67 ± 5	113 ± 3	90 ± 4	68 ± 5	535 ± 33
InAs/InSb /InAs	With In NP consumption	36 ± 4	50 ± 7	109 ± 3	79 ± 6	66 ± 6	555 ± 40

As clearly observed from the SEM images, the NP consumption with As flux results in a smaller NP on top of the NWs. The measured contact angle after consumption of In NP is 88 ± 5° which is obviously lower than standard contact angle 118 ± 3° of InAs/InSb NWs. At the end of the InAs top segment growth, the measured values of D_{InSb}, D_{bottom} and L_{NWs} are 79 ± 6 nm, 66 ± 6 nm, and 555 ± 40 nm for the sample with NP consumption, and 90 ± 4 nm, 68 ± 5 nm, and 535 ± 33 nm, respectively.

By comparing the values of D_{InSb} in the two samples with the InAs top segment, we can clearly see that D_{InSb} is smaller (79 ± 6 nm) in the sample grown after In NP consumption, compared to the sample grown without NP consumption (90 ± 4 nm), while the value of D_{bottom} is the same in both samples (66 ± 6 and 68 ± 5 nm). Therefore, we can conclude that the In droplet size plays a role in the InAs radial growth around the InSb QD, while it does not affect the InAs radial growth at the NW bottom. This

suggests that there are different In adatom diffusion paths towards the growth front: one from the substrate, that is independent from the NP size, and one from the NW sidewalls, involving only a collection area close to the NP (within a diffusion length from the droplet), and directly influenced by the NP dynamics [200].

6.3.5 The evolution of diameter of NWs versus length

The presence of different In adatom diffusion paths are even more evident if we consider the diameter evolution of the NWs at different positions along the growth axis. Indeed, we measured the diameter of the NWs from the base to the top every 100 ± 4 nm along the growth axis, for 15 min, 30 min and 45 min samples of the time series shown in Fig. 6.5. The results are plotted in Fig. 6.8 panel (a). Considering the lower part of the NW (below the QD position), it is clear that it has a uniform diameter at the beginning of the growth of the InAs top segment, then it starts to be inverse tapered at 15 min of growth and continue to be inverse tapered below 30 min. Then the diameter becomes uniform for 30 min growth and it evolves as tapered at 45 min of growth. On the other hand, the diameter of the upper part of the NW (above the QD position) is uniform up to 30 min of InAs top segment growth and it becomes inverse tapered at 45 min of growth.

Panel (b) of Fig. 6.8 shows the NW diameter versus InAs growth time for 2 positions along the growth axis: at 100 ± 4 nm and at 400 ± 4 nm from the base. The former representing the diameter of the lower part of the InAs stem and the latter the diameter of the NW at the InSb QD position, i.e. D_{InSb}. We found that D_{InSb} increases almost linearly with growth time, with constant slope, suggesting a constant growth mechanism, that is probably the diffusion of the In adatoms on the NW sidewalls close to the NP (within a diffusion length from the droplet). Conversely, the diameter of NWs at 100 nm from the base, after an initial delay, increases quickly from 10 min to 20 min of growth time and then it continues to increase but with an abrupt change of slope. This behavior suggests that for the first 20 min of growth there are two contributions to the InAs radial growth in the lower part of the NWs, i.e the diffusion of the In adatoms from the substrate and the diffusion on the NW sidewalls toward the growth front. Above 20 min of growth (L_{NWs} > 570 nm) the In droplet is too far from the NW base so that sidewall diffusion within the collection area close to the NP does not contribute anymore to the radial growth at the NW base. Indeed, above 30 minutes of InAs growth the only contribution to the radial growth at the lower part of the NWs

is the diffusion from the substrate and we do observe a gradual tapering. This suggests a diffusion length of the In adatoms lower than 280 nm, consistent with the tapering shape observed at the NW lower segment in the 45 minutes sample. A schematic illustration of the combination of the two mechanisms for the InAs radial growth and the effect on the final NW shape is shown in Fig. 6.8 panel (c). Similar results were reported for Ga-assisted GaAs [217] and GaP [218] NWs.

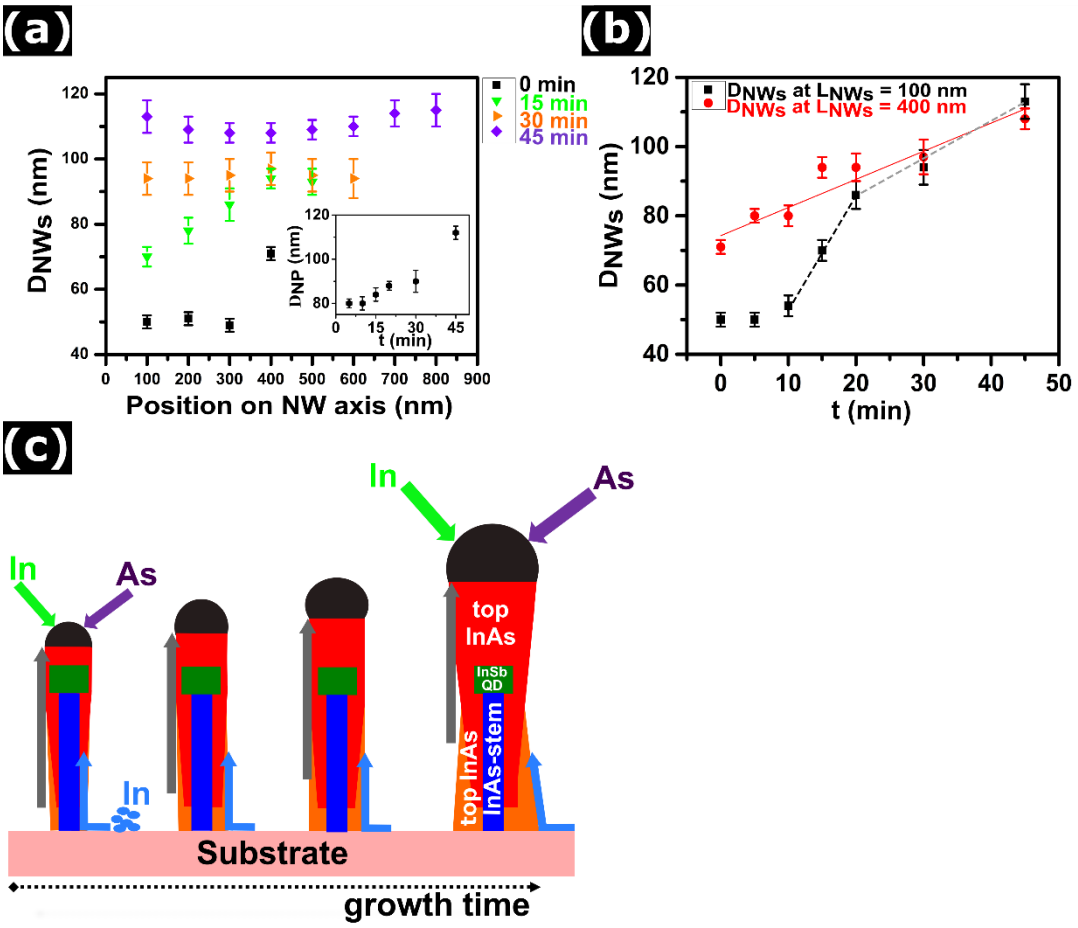

Figure 6.8. (a) NW diameter as a function of position along the length of NW, for 15 min, 30 min and 45 min samples of the time series shown in Fig. 6.5 (a). The black, green, orange, and violet colors represent 0 min, 15 min, 30 min and 45 min growth times, respectively. The inset of panel (a) shows the relationship between D_{NP} and growth time. (b) Evolution of the diameter of NWs at the base of NWs and around the InSb QD with respect to the growth time. The red line represents the linear fit of the DInSb versus time, while the black and grey dotted lines are just to guide the eye and highlight the change of slope. (c) A schematic illustration of the growth mechanisms for the radial growth and the resulting shape of the NWs.

6.4 Discussion

Considering these results, we can provide a general description of the axial and radial growth of the InAs top segment: the T_{InAs} and F_{As} series, and the NP-consumption experiment clearly demonstrate that the volume of the In NP is playing an important role for both the axial and the radial growth of the InAs top segment.

Indeed, at low growth temperature the NP volume is larger, therefore the radial growth in the top part of the NW is enhanced [200]. At the same time, the VLS axial growth is also enhanced by bigger NPs. As the growth temperature is increased, the NP become smaller and so both axial and radial growth rate decrease. Moreover, at high growth temperature In desorption starts to be sizeable [61] so that both growth rates decrease. Moreover, considering the As line pressure series, we found that when the growth conditions preserve an In droplet with $\beta > 90°$ on top of the NWs, both axial and radial growths are enhanced by increasing F_{As}, meaning that both VLS and VS growth are As-limited. Finally, the time evolution of the NW diameter for samples growth under In-rich conditions allowed us to confirm that there are two contributions to the radial InAs growth, i.e. diffusion of In adatoms from the substrate toward the growth front, and the diffusion on the NW sidewalls within a diffusion length distance from the NP. The second contribution is strongly affected by the NP size and dynamics. The two diffusion paths and the total length of the NW determine the final shape of the NW.

6.5 Crystal structure analysis

In order to study the crystal structure of the InSb/InAs QD NWs, we performed TEM analysis. Figure 6.9 shows the HAADF-STEM (a) and HR-TEM images (b), with the corresponding FFT of the InSb/InAs QD NWs with InAs top segment grown with F_{In} = 0.30 Torr, F_{As} = 0.25 Torr, for t = 15 min at the growth temperature of 440 °C. From the STEM micrograph we could identify the InSb QD thanks to the different Z contrast of InAs and InSb materials and we could measure the diameter and length of InSb QD and length of InAs top segment of many NWs obtaining D_{InSb} = 85 ± 4 nm, L_{QD} = 39 ± 6 nm, and L_{top} = 105 ± 5 nm, respectively, consistent with the results obtained from SEM images. From the HR-TEM analysis, we observed that InAs-stem and InAs-top segment have a WZ crystal structure with several defects such as stacking faults and twins perpendicular to the growth direction. It is commonly observed that the InAs NWs grown by catalyst-free and self-catalyzed growth methods show highly defective (or mixed WZ/ZB) crystal structure [55,66]. By contrast, the InSb QD shows a defect-free ZB crystal structure without any stacking faults, consistently with the energetically preferred cubic structure of the InSb crystals [42,103,184] generally attributed to the low ionicity of group III to Sb bonds [42]. This

analysis confirms the good crystal quality of the self-catalyzed InSb QD embedded into InAs NWs.

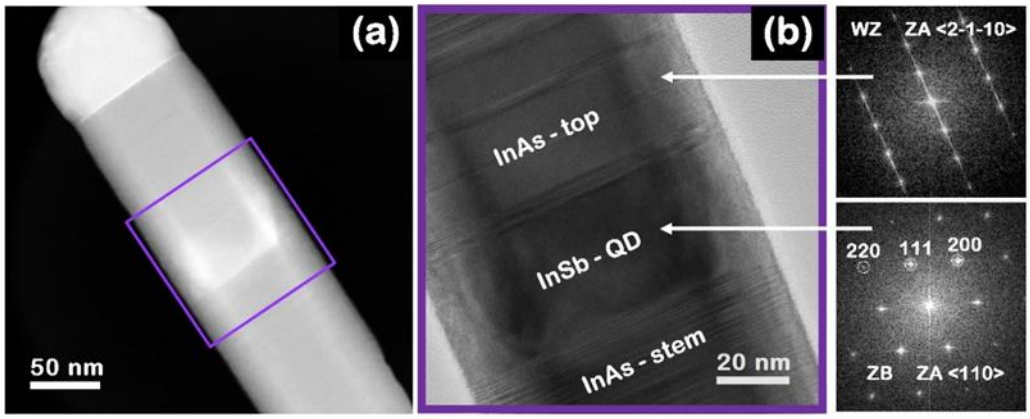

Figure 6.9. TEM analysis of a representative InSb/InAs QD NW. (a) HAADF-STEM image, (b) HR-TEM image of the NW region framed by the purple square in panel (a). The FFT analysis shown on the bottom right confirms the ZB structure of the QD segment.

6.6 Conclusions

In conclusion, we have demonstrated the growth of self-catalyzed InSb/InAs QD NWs on Si (111) substrates by chemical beam epitaxy technique. The morphology and the growth mechanisms of the InAs top segment were thoroughly investigated as a function of growth temperature, As line pressure, and growth time. We found that both axial and radial growth rates decrease by increasing the growth temperature. Furthermore, both axial and radial growth rates are enhanced by the As line pressure, therefore both the VLS axial growth and the VS radial growth are As-limited in a self-catalyzed growth regime. Finally, we found that the volume of the In NP is controlling both the axial and the radial growth of the InAs top segment. Indeed, the radial growth around the InSb QD and the top part of the NW is mainly determined by the volume of the In NP, while the radial InAs growth at the bottom part of the NWs is affected from both the NP size and the surface diffusion of In adatoms from the substrate only below a certain NW length, then becoming independent from NP dynamics. Our study provides useful guidelines for the realization of InSb/InAs QD NWs with the desired shape and morphology, for device applications. Moreover, we believe that the obtained results could be useful for engineering the properties of other self-catalyzed NWs systems.

Chapter 7: Conclusions

The main perspective of this thesis is the growth of self-catalyzed and catalyst-free InAs and Sb based NWs and their HSs on Si (111) substrates. The growth of NWs has been conducted by using chemical beam epitaxy. We have discussed several strategies to obtain the desired morphology of the grown NWs. The growth mechanisms and dynamics have been studied thoroughly by tuning the growth parameters. Optimized catalyst-free InAs/InP/GaAsSb CDS NWs were achieved by varying the growth parameters. We found that an InP shell thickness between 1 nm and 8 nm is uniform along all the crystallographic directions. The strain is accommodated through a tetragonal distortion of the lattice without forming structural defects. After successful growth of CDS NWs, two-probe and four-probe electronic devices were fabricated to investigate the impact of InP barriers on the charge-transport properties of the InAs/InP/GaAsSb CDS NWs. We observed that a 10 nm-thick InP barrier effectively suppressed the conduction band-to-valence band tunneling between the InAs core and the outer GaAsSb shell. Moreover, field effect modulation of charge transport in our devices indicates an n- and p-type nature of the InAs core and the GaAsSb shell, respectively.

The growth mechanisms of self-catalyzed InAs/InSb axial heterostructured NWs have been thoroughly investigated as a function of the In and Sb line pressures, and growth time. We have demonstrated that rapid radial growth of InSb is not a consequence of the droplet inflation but is rather due to the VS radial growth on the NW sidewalls, so that the In droplet may shrink and the whole NW extend. The presence of an In droplet on the NW top is absolutely required to maintain the axial growth of the heterostructure. The growth kinetics of InSb NW sections and of the In droplets on their tops have been explained and quantified within a model containing no free parameters. Next, we used them as templates to grow self-catalyzed InSb/InAs QDs. The morphology and the growth mechanisms of the InAs top segment have been studied as a function of growth temperature, As line pressure, and growth time. We found that the axial and radial growth rates decrease with increasing growth temperature. Furthermore, the axial and radial growth rates are As-limited by VLS and VS growth modes in a self-catalyzed regime. We observed that the volume of the In

NP is controlling both the axial and the radial growth of the InAs top segment. Results achieved from time series allowed us to understand the evolution of the diameter along the entire length of the nanowire.

Our research activities provide useful guidelines for obtaining device-quality InAs and Sb containing axial and multi shell NW heterostructures and give a clear route for engineering the morphology of such heterostructures. In particular, InSb QD NWs might find applications both as mid-infrared detectors and as building blocks of optoelectronic devices taking advantage of the outstanding electronic properties of antimonide semiconductors. Moreover, the present approach can be applied to grow heterostructures of other lattice-mismatch materials, in order to expand the range of options for device fabrication to be employed for a wide range of various applications.

References

[1] Li, Y.; Qian, F.; Xiang, J.; Lieber, C. M. Nanowire Electronic and Optoelectronic Devices. *Mater. Today* **2006**, *9*, 18–27.

[2] Intel. Advancing Moore's Law —The Road to 14 nm.

[3] Moore, G. E. Cramming more components onto integrated circuits. *Proc. IEEE* **1998**, *86*, 82–85.

[4] Cartwright, J. Intel enters the third dimension. *Nature* **2011**.

[5] Riel, H.; Wernersson, L. E.; Hong, M.; del Alamo, J. A. III–V Compound Semiconductor Transistors—from Planar to Nanowire Structures. *MRS Bulletin* **2014**, *39*, 668–677.

[6] Alamo, J. A. Nanometre-Scale Electronics with III–V Compound Semiconductors. *Nature* **2011**, *479*, 317–323.

[7] Joyce, H. J.; Boland, J. L.; Davies, C. L.; Baig, S. A.; Johnston, M. B. A Review of the Electrical Properties of Semiconductor Nanowires: Insights Gained from Terahertz Conductivity Spectroscopy. *Semicond. Sci. Technol.* **2016**, *31*, 103003–103024.

[8] Dayeh, S. A.; Tang, W.; Boioli, F.; Kavanagh, K. L.; Zheng, H.; Wang, J.; Mack, N. H.; Swadener, G.; Huang, J. Y.; Miglio, L.; Tu, K. N.; Picraux, S. T. Direct Measurement of Coherency Limits for Strain Relaxation in Heteroepitaxial Core/Shell Nanowires. *Nano Lett.* **2013**, *13*, 1869–1876.

[9] Reimer, M. E.; Bulgarini, G.; Akopian, N.; Hocevar, M.; Bavinck, M. B.; Verheijen, M. A.; Bakkers, E. P. A. M.; Kouwenhoven, L. P.; Zwiller, V. Bright Single-Photon Sources in Bottom-up Tailored Nanowires. *Nat. Commun.* **2012**, *3*, 737–742.

[10] Bulgarini, G.; Reimer, M. E.; Bouwes Bavinck, M.; Jöns, K. D.; Dalacu, D.; Poole, P. J.; Bakkers, E. P. A. M.; Zwiller, V. Nanowire Waveguides Launching Single Photons in a Gaussian Mode for Ideal Fiber Coupling. *Nano Lett.* **2014**, *14*, 4102–4106.

[11] Kelzenberg, M. D.; Boettcher, S. W.; Petykiewicz, J. A.; Turner-Evans, D. B.; Putnam, M. C.; Warren, E. L.; Spurgeon, J. M.; Briggs, R. M.; Lewis, N. S.; Atwater, H. A. Enhanced Absorption and Carrier Collection in Si Wire Arrays for Photovoltaic Applications. *Nat. Mater.* **2010**, *9*, 239–244.

[12] Krogstrup, P.; Jørgensen, H. I.; Heiss, M.; Demichel, O.; Holm, J. V.; Aagesen, M.; Nygard, J.; Fontcuberta I Morral, A. Single-Nanowire Solar Cells beyond the Shockley-Queisser Limit. *Nat. Photonics* **2013**, *7*, 306–310.

[13] Ng, H. T.; Han, J.; Yamada, T.; Nguyen, P.; Chen, Y. P.; Meyyappan, M. Single Crystal Nanowire Vertical Surround-Gate Field-Effect Transistor. *Nano Lett.* **2004**, *4*, 1247–1252.

[14] Lind, E.; Persson, A. I.; Samuelson, L.; Wernersson, L. Improved Subthreshold Slope in an InAs Nanowire Heterostructure Field-Effect Transistor. *Nano Lett.* **2006**, *6*, 1842–1846.

[15] Law, M.; Greene, L. E.; Johnson, J. C.; Saykally, R. Nanowire Dye-Sensitized Solar Cells. *Nature Mater.* **2005**, *4*, 455–459.

[16] Garnett, E. C.; Yang, P. Silicon Nanowire Radial p - n Junction Solar Cells. *J. Am. Chem. Soc.* **2008**, *130*, 9224–9225.

[17] Czaban, J. A.; Thompson, D. A.; Lapierre, R. R. GaAs Core-Shell Nanowires for Photovoltaic Applications. *Nano Lett.* **2009**, *9*, 148–154.

[18] Yao, M.; Cong, S.; Arab, S.; Huang, N.; Michelle, L.; Cronin, S. B.; Dapkus, D. P.; Zhou, C. Tandem Solar Cells Using GaAs Nanowires on Si: Design, Fabrication, and Observation of Voltage Addition. *Nano Lett.* **2015**, *15*, 7217–7224.

[19] Thelander, C.; Mårtensson, T.; Björk, M. T.; Ohlsson, B. J.; Larsson, M. W.; Wallenberg, L. R.; Samuelson, L.; Bjo, M. T. Single-Electron Transistors in Heterostructure Nanowires. *Appl. Phys. Lett.* **2003**, *83*, 4458–4460.

[20] Bjo, M. T.; Thelander, C.; Hansen, A. E.; Jensen, L. E.; Larsson, M. W.; Wallenberg, L. R.; Samuelson, L. Few-Electron Quantum Dots in Nanowires. *Nano Lett.* **2004**, *4*, 1621–1625.

[21] Thelander, C.; Nilsson, H. A.; Jensen, L. E.; Samuelson, L. Nanowire Single-Electron Memory. *Nano Lett.* **2005**, *5*, 635–638.

[22] Nilsson, H. A.; Duty, T.; Abay, S.; Wilson, C.; Wagner, J. B.; Thelander, C.; Delsing, P.; Samuelson, L. A Radio Frequency Single-Electron Transistor Based on an InAs / InP Heterostructure Nanowire. *Nano Lett.* **2008**, *8*, 872–875.

[23] Li, Z.; Yuan, X.; Fu, L.; Peng, K.; Wang, F.; Fu, X.; Caro_, P.; White, T.P.; Tan, H.H.; Jagadish, C. Room temperature GaAsSb single nanowire infrared photodetectors. *Nanotechnology* **2015**, *26*, 445202.

[24] Weng, W. Y.; Hsueh, T.J.; Chang, S.J.;Wang, S.B.; Hsueh, H.T.; Huang, G.J. A high-responsivity GaN nanowire UV photodetector. IEEE J. Sel. Top. *Quantum Electron*. **2011**, *17*, 996–1001.

[25] Miao, J.; Hu, W.; Guo, N.; Lu, Z.; Zou, X.; Liao, L.; Shi, S.; Chen, P.; Fan, Z.; Ho, J.C.; et al. Single InAs nanowire room-temperature near-infrared photodetectors. *ACS Nano* **2014**, *8*, 3628–3635.

[26] Björk, M. T.; Ohlsson, B. J.; Thelander, C.; Persson, A. I.; Deppert, K.; Wallenberg, L. R.; Samuelson, L. Nanowire Resonant Tunneling Diodes. *Appl. Phys. Lett.* **2002**, *83*, 4458–4460.

[27] Dey, A. W.; Svensson, J.; Ek, M.; Lind, E.; Thelander, C.; Wernersson, L. E. Combining Axial and Radial Nanowire Heterostructures: Radial Esaki Diodes and Tunnel Field-Effect Transistors. *Nano Lett.* **2013**, *13*, 5919–5924.

[28] Borg, B. M.; Dick, K. A.; Ganjipour, B.; Pistol, M. E.; Wernersson, L. E.; Thelander, C. InAs/GaSb Heterostructure Nanowires for Tunnel Field-Effect Transistors. *Nano Lett.* **2010**, *10*, 4080–4085.

[29] Soci, C.; Zhang, A.; Bao, X.-Y.; Kim, H.; Lo, Y.;Wang, D. Nanowire Photodetectors. *J. Nanosci. Nanotechnol.* **2010**, *10*, 1430–1449.

[30] Li, Z.; Tan, H.H.; Jagadish, C.; Fu, L. III–V Semiconductor Single Nanowire Solar Cells: A Review. *Adv. Mater. Technol.* **2018**, *3*, 1800005.

[31] Jiang, X.; Xiong, Q.; Nam, S.; Qian, F.; Li, Y. InAs / InP Radial Nanowire Heterostructures as High Electron Mobility Devices. *Nano Lett.* **2007**, *7*, 3214–3218.

[32] Tomioka, K.; Fukui, T. Tunnel field-effect transistor using InAs nanowire/Si heterojunction. *Appl. Phys. Lett.* **2011**, *98*, 083114.

[33] Offermans, P.; Brongersma, S. H. Procedia Engineering Gas Sensing with Vertical Functionalized InAs Nanowire Arrays. *Procedia Eng.* **2010**, *5*, 1111–1114.

[34] Heeres, E. C.; Bakkers, E. P. A. M.; Roest, A. L.; Kaiser, M.; Oosterkamp, T. H.; Jonge, N. De. Electron Emission from Individual Indium Arsenide Semiconductor Nanowires. *Nano Lett.* **2007**, *7*, 536–540.

[35] Borg, B. M.; Wernersson, L. Synthesis and Properties of Antimonide Nanowires. *Nanotechnology* **2013**, *24*, 202001–202018.

[36] Mingo, N. Thermoelectric Figure of Merit and Maximum Power Factor in III-V Semiconductor Nanowires. *Appl. Phys. Lett.* **2004**, *84*, 2652–2654.

[37] Lind, E.; Memisevic, E.; Dey, A. W.; Wernersson, L. E. III-V Heterostructure Nanowire Tunnel FETs. *IEEE J. Electron Devices Soc.* **2015**, *3*, 96–102.

[38] Shafa, M.; Akbar, S.; Gao, L.; Fakhar-e-Alam, M.; Wang, Z. M. Indium Antimonide Nanowires: Synthesis and Properties. *Nanoscale Res. Lett.* **2016**, *164*.

[39] Lutchyn, R. M.; Bakkers, E. P. A. M.; Kouwenhoven, L. P.; Krogstrup, P.; Marcus, C. M.; Oreg, Y. Majorana zero modes in superconductor–semiconductor heterostructures. *Nat. Rev. Mater.* **2018**, *3*, 52–68.

[40] Fang, M.; Han, N.; Wang, F.; Yang, Z. X.; Yip, S.; Dong, G.; Hou, J. J.; Chueh, Y.; Ho, J. C. III-V Nanowires: Synthesis, Property Manipulations, and Device Applications. *J. Nanomater.* **2014**, *2014*.

[41] Zi, Y.; Zhao, Y.; Candebat, D.; Appenzeller, J.; Yang, C. Synthesis of Antimony-Based Nanowires Using the Simple Vapor Deposition Method. *ChemPhysChem* **2012**, *13*, 2585–2588.

[42] Yip, S.; Shen, L.; Ho, J.C. Recent Advances in III-Sb Nanowires: From Synthesis to Applications. *Nanotechnology* **2019**, *30*, 202003–202027.

[43] Barrigón, E.; Heurlin, M.; Bi, Z.; Monemar, B.; Samuelson, L. Synthesis and Applications of III-V Nanowires. *Chem. Rev.* **2019**, *119*, 9170–9220.

[44] Li, Z.; Allen, J.; Allen, M.; Tan, H.H.; Jagadish, C.; Fu, L. Review on III-V Semiconductor Single Nanowire-Based Room Temperature Infrared Photodetectors. *Materials* **2020**, *13*, 1400.

[45] Joyce, H. J.; Gao, Q.; Hoe Tan, H.; Jagadish, C.; Kim, Y.; Zou, J.; Smith, L. M.; Jackson, H. E.; Yarrison-Rice, J. M.; Parkinson, P.; Johnston, M. B. III-V Semiconductor Nanowires for Optoelectronic Device Applications. *Prog. Quantum Electron.* **2011**, *35*, 23–75.

[46] Wagner, R. S.; Ellis, W. C. Vapor-Liquid-Solid Mechanism of Single Crystal Growth. *Appl. Phys. Lett.* **1964**, *4*, 89–90.

[47] Hiruma, K.; Yazawa, M.; Haraguchi, K.; Ogawa, K.; Katsuyama, T.; Koguchi, M.; Kakibayashi, H. GaAs free-standing quantum-size wires. *J. Appl. Phys.* **1993**, *74*, 3162–3171.

[48] Dick, K. A.; Caroff, P. Metal-Seeded Growth of III−V Semiconductor Nanowires: Towards Gold-Free Synthesis. *Nanoscale* **2014**, *6*, 3006−3021.

[49] Gomes, U. P.; Ercolani, D.; Zannier, V.; Beltram, F.; Sorba, L. Controlling the Diameter Distribution and Density of InAs Nanowires Grown by Au-Assisted Methods. *Semicond. Sci. Technol.* **2015**, *30*, 115012–115020.

[50] Vukajlovic-Plestina, J.; Kim, W.; Ghisalberti, L.; Varnavides, G.; Tütüncuoglu, G.; Potts, H.; Friedl, M.; Güniat, L.; Carter, W. C.; Dubrovskii, V. G.; Fontcuberta i Morral, A. Fundamental Aspects to Localize Self-Catalyzed III-V Nanowires on Silicon. *Nat. Commun.* **2019**, *10*, 869.

[51] Güniat, L.; Caroff, P.; Fontcuberta I Morral, A. Vapor Phase Growth of Semiconductor Nanowires: Key Developments and Open Questions. *Chem. Rev.* **2019**, *119*, 8958–8971.

[52] Paladugu, M.; Zou, J.; Guo, Y. N.; Zhang, X.; Kim, Y.; Joyce, H. J.; Gao, Q.; Tan, H. H.; Jagadish, C. Nature of heterointerfaces in GaAs/InAs and InAs/GaAs axial nanowire heterostructures. *Appl. Phys. Lett.* **2008,** *93*, 101911.

[53] Li, L.; Pan, D.; So, H.; Wang, X.; Yu, Z.; Zhao, J. GaAsSb/InAs Core-Shell Nanowires Grown by Molecular-Beam Epitaxy. *J. Alloys Compd.* **2017**, *724*, 659–665.

[54] Zannier, V.; Ercolani, D.; Gomes, U. P.; David, J.; Gemmi, M.; Dubrovskii, V. G.; Sorba, L. Catalyst Composition Tuning: The Key for the Growth of Straight Axial Nanowire Heterostructures with Group III Interchange. *Nano Lett.* **2016**, *16*, 7183–7190.

[55] Gomes, U.P.; Ercolani, D.; Zannier, V.; David, J.; Gemmi, M.; Beltram, F.; Sorba, L. Nucleation and Growth Mechanism of Self-Catalyzed InAs Nanowires on Silicon. *Nanotechnology* **2016**, *27*, 255601–255607.

[56] Zhang, G.; Sasaki, S.; Tateno, K.; Gotoh, H.; Sogawa, T. Au-Free InAs Nanowires Grown in In-Particle-Assisted Vapor-Liquid-Solid Mode: Growth, Structure, and Electrical Property. *AIP Adv.* **2013**, *3*, 052107–052118.

[57] Mattila, M.; Hakkarainen, T.; Lipsanen, H. Catalyst-free growth of In(As)P nanowires on silicon. *Appl. Phys. Lett.* **2006**, *89*, 063119.

[58] Novotny, C. J.; Yu, P. K. L. Vertically aligned, catalyst-free InP nanowires grown by metalorganic chemical vapor deposition. *Appl. Phys. Lett.* **2005**, *87*, 203111.

[59] Jabeen, F.; Grillo, V.; Rubini, S.; Martelli, F. Self-catalyzed growth of GaAs nanowires on cleaved Si by molecular beam epitaxy. *Nanotechnology* **2008**, *19*, 275711.

[60] Ghalamestani, S. G.; Mazid Munshi, A.; Dheeraj, D. L.; Fimland, B. O.; Weman, H.; Dick, K. A. Self-Catalyzed MBE Grown GaAs/$GaAs_xSb_{1-x}$ Core-Shell Nanowires in ZB and WZ Crystal Structures. *Nanotechnology* **2013**, *24*, 405601–405606.

[61] Anyebe, E. A. Influence of Growth Parameters on In-Droplet-Assisted Growth of InAs Nanowires on Silicon. *Appl. Nanosci.* **2017**, *7*, 365–370.

[62] Grap, T.; Rieger, T.; Blömers, C.; Schäpers, T.; Grützmacher, D.; Lepsa, M. I. Self-Catalyzed VLS Grown InAs Nanowires with Twinning Superlattices. *Nanotechnology* **2013**, *24*, 335601–335607.

[63] Koblmüller, G.; Hertenberger, S.; Vizbaras, K.; Bichler, M.; Bao, F.; Zhang, J. P.; Abstreiter, G. Self-Induced Growth of Vertical Free-Standing InAs Nanowires on Si (111) by Molecular Beam Epitaxy. *Nanotechnology* **2010**, *21*, 365602–365606.

[64] Rieger, T.; Grützmacher, D.; Lepsa, M. I. Si Substrate Preparation for the VS and VLS Growth of InAs Nanowires. *Phys. Status Solidi - Rapid Res. Lett.* **2013**, *7*, 840–844.

[65] Gomes, U. P.; Ercolani, D.; Zannier, V.; Battiato, S.; Ubyivovk, E.; Mikhailovskii, V.; Murata, Y.; Heun, S.; Beltram, F.; Sorba, L. Heterogeneous Nucleation of Catalyst-Free InAs Nanowires on Silicon. *Nanotechnology* **2017**, *28*, 065603–065609.

[66] Gomes, U. P.; Ercolani, D.; Sibirev, N. V.; Gemmi, M.; Dubrovskii, V. G.; Beltram, F.; Sorba, L. Catalyst-Free Growth of InAs Nanowires on Si (111) by CBE. *Nanotechnology* **2015**, 26, 415604.

[67] Lieber, C. M. Semiconductor Nanowires: A Platform for Nanoscience and Nanotechnology. *MRS Bull.* **2011**, *36*, 1052–1063.

[68] Hayden, O.; Agarwal, R.; Lu, W. Semiconductor Nanowire Devices. *Nano Today* **2008**, *3*, 12–22.

[69] FRENSLEY, W. R. *Heterostructure and Quantum Well Physics*; ACADEMIC PRESS, INC., 1994; Vol. 24.

[70] Batey, J.; Wright, S. L. Energy Band Alignment in GaAs:(Al,Ga)As Heterostructures: The Dependence on Alloy Composition. *J. Appl. Phys.* **1986**, *59*, 200–209.

[71] Demichel, O.; Heiss, M.; Bleuse, J.; Mariette, H.; Fontcuberta Morral, I. A. Impact of Surfaces on the Optical Properties of GaAs Nanowires. *Appl. Phys. Lett.* **2010**, *97*, 201907–201910.

[72] Yong, C. K.; Wong-Leung, J.; Joyce, H. J.; Lloyd-Hughes, J.; Gao, Q.; Tan, H. H.; Jagadish, C.; Johnston, M. B.; Herz, L. M. Direct Observation of Charge-Carrier Heating at WZ-ZB InP Nanowire Heterojunctions. *Nano Lett.* **2013**, *13*, 4280–4287.

[73] Thelander, C.; Caroff, P.; Plissard, S.; Dey, A. W.; Dick, K. A. Effects of Crystal Phase Mixing on the Electrical Properties of InAs Nanowires. *Nano Lett.* **2011**, *11*, 2424–2429.

[74] Spirkoska, D.; Arbiol, J.; Gustafsson, A.; Conesa-Boj, S.; Glas, F.; Zardo, I.; Heigoldt, M.; Gass, M. H.; Bleloch, A. L.; Estrade, S.; Kaniber, M.; Rossler, J.; Peiro, F.; Morante, J. R.; Abstreiter, G.; Samuelson, L.; Fontcuberta I Morral, A. Structural and Optical Properties of High Quality Zinc-Blende/Wurtzite GaAs Nanowire Heterostructures. *Phys. Rev. B - Condens. Matter Mater. Phys.* **2009**, *80*, 1–9.

[75] Vainorius, N.; Jacobsson, D.; Lehmann, S.; Gustafsson, A.; Dick, K. A.; Samuelson, L.; Pistol, M. E. Observation of Type-II Recombination in Single Wurtzite/Zinc-Blende GaAs Heterojunction Nanowires. *Phys. Rev. B - Condens. Matter Mater. Phys.* **2014**, *89*, 1–8.

[76] Smith, L. M.; Jackson, H. E.; Yarrison-Rice, J. M.; Jagadish, C. Insights into Single Semiconductor Nanowire Heterostructures Using Time-Resolved Photoluminescence. *Semicond. Sci. Technol.* **2010**, *25*, 024010–024022.

[77] Grönqvist, J.; Søndergaard, N.; Boxberg, F.; Guhr, T.; Åberg, S.; Xu, H. Q. Strain in Semiconductor Core-Shell Nanowires. *J. Appl. Phys.* **2009**, *106*, 053508.

[78] Salehzadeh, O.; Kavanagh, K. L.; Watkins, S. P. Geometric Limits of Coherent III-V Core/Shell Nanowires. *J. Appl. Phys.* **2013**, *114*, 054301.

[79] Rieger, T.; Grützmacher, D.; Lepsa, M. I. Misfit Dislocation Free InAs/GaSb Core-Shell Nanowires Grown by Molecular Beam Epitaxy. *Nanoscale* **2015**, *7*, 356–364.

[80] Treu, J.; Bormann, M.; Schmeiduch, H.; Döblinger, M.; Morkötter, S.; Matich, S.; Wiecha, P.; Saller, K.; Mayer, B.; Bichler, M.; et al. Enhanced Luminescence Properties of InAs-InAsP Core-Shell Nanowires. *Nano Lett.* **2013**, *13*, 6070–6077.

[81] Heurlin, M.; Stankevič, T.; Mickevičius, S.; Yngman, S.; Lindgren, D.; Mikkelsen, A.; Feidenhans'l, R.; Borgström, M. T.; Samuelson, L. Structural Properties of Wurtzite InP-InGaAs Nanowire Heterostructures. *Nano Lett.* **2015**, *15*, 2462–2467.

[82] Yuan, X.; Caroff, P.; Wang, F.; Guo, Y.; Wang, Y.; Jackson, H. E.; Smith, L. M.; Tan, H. H.; Jagadish, C. Antimony Induced {112}A Faceted Triangular $GaAs_{1-x}Sb_x$/InP Core/Shell Nanowires and their Enhanced Optical Quality. *Adv. Funct. Mater.* **2015**, *25*, 5300–5308.

[83] Ercolani, D.; Rossi, F.; Li, A.; Roddaro, S.; Grillo, V.; Salviati, G.; Beltram, F.; Sorba, L. InAs/InSb Nanowire Heterostructures Grown by Chemical Beam Epitaxy. *Nanotechnology* **2009**, *20*, 505605–505610.

[84] Dick, K. A.; Caroff, P.; Bolinsson, J.; Messing, M. E.; Johansson, J.; Deppert, K.; Wallenberg, L. R.; Samuelson, L. Control of III-V Nanowire Crystal Structure by Growth Parameter Tuning. *Semicond. Sci. Technol.* **2010**, *25*, 024009–024020.

[85] Weman, H.; Dasa, D. L. III-Antimonide Nanowires. In *Advances in III-V Semiconductor Nanowires and Nanodevices*; Li, J., Wang, D., LaPierre, R. R., Eds.; Bentham Science Publishers Ltd.: Danvers, MA, USA, 2011; pp. 89−104.

[86] Tomioka, K.; Fukui, T. Recent Progress in Integration of III-V Nanowire Transistors on Si Substrate by Selective-Area Growth. *J. Phys. D. Appl. Phys.* **2014**, *47*, 394001–394013.

[87] Rocci, M.; Rossella, F.; Gomes, U. P.; Zannier, V.; Rossi, F.; Ercolani, D.; Sorba, L.; Beltram, F.; Roddaro, S. Tunable Esaki Effect in Catalyst-Free InAs/GaSb Core-Shell Nanowires. *Nano Lett.* **2016**, *16*, 7950–7955.

[88] Vasen, T.; Ramvall, P.; Afzalian, A.; Doornbos, G.; Holland, M.; Thelander, C.; Dick, K.A.; Wernersson, L. E.; Passlack, M. Vertical Gate-All-Around Nanowire GaSb-InAs Core-Shell n-Type Tunnel FETs. *Sci. Rep.* **2019**, *9*, 202–210.

[89] Ganjipour, B.; Leijnse, M.; Samuelson, L.; Xu, H. Q.; Thelander, C. Transport Studies of Electron-Hole and Spin-Orbit Interaction in GaSb/InAsSb Core-Shell Nanowire Quantum Dots. *Phys. Rev. B* **2015**, *91*, 161301–161305.

[90] Furthmeier, S.; Dirnberger, F.; Gmitra, M.; Bayer, A.; Forsch , M.; Hubmann, J.; Schu¨ller, C.; Reiger , E.; Fabian, J.; Korn, T.; Bougeard, D. Enhanced spin-orbit coupling in core/shell nanowires. *Nat. Commun.* **2016**, *7*, 12413–12419.

[91] Keller, A. J.; Lim, J. S.; Sánchez, D.; López, R.; Amasha, S.; Katine, J. A.; Shtrikman, H.; Goldhaber-Gordon, D. Cotunneling Drag Effect in Coulomb-Coupled Quantum Dots. *Phys. Rev. Lett.* **2016**, *117*, 066602–066606.

[92] Grasselli, F.; Bertoni, A.; Goldoni, G. The role of internal dynamics in the coherent evolution of indirect excitons. *Superlattices Microst.* **2017**, *108*, 73–78.

[93] Kats, V. N.; Kochereshko, V. P.; Platonov, A. V.; Chizhova, T. V.; Cirlin, G. E.; Bouravleuv, A. D.; Samsonenko, Y. B.; Soshnikov, I. P.; Ubyivovk, E. V.; Bleuse, J.; Mariette, H. Optical Study of GaAs Quantum Dots Embedded into AlGaAs Nanowires. *Semicond. Sci. Technol.* **2012**, *27*, 015009–015013.

[94] Wu, J.; Ramsay, A.; Sanchez, A.; Zhang, Y.; Kim, D.; Brossard, F.; Hu, X.; Benamara, M.; Ware, M. E.; Mazur, Y. I.; Salamo, G. J.; Aagesen, M.; Wang, Z.; Liu, H. Defect-Free Self-Catalyzed GaAs/GaAsP Nanowire Quantum Dots Grown on Silicon Substrate. *Nano Lett.* **2016**, *16*, 504–511.

[95] Borgström, M. T.; Zwiller, V.; Müller, E.; Imamoglu, A. Optically Bright Quantum Dots in Single Nanowires. *Nano Lett.* **2005**, *5*, 1439–1443.

[96] Van Weert, M. H. M.; Akopian, N.; Perinetti, U.; Van Kouwen, M. P.; Algra, R. E.; Verheijen, M. A.; Erik, P. A. M. B.; Kouwenhoven, L. P.; Zwiller, V. Selective Excitation and Detection of Spin States in a Single Nanowire Quantum Dot. *Nano Lett.* **2009**, *9*, 1989–1993.

[97] Roddaro, S.; Pescaglini, A.; Ercolani, D.; Sorba, L.; Beltram, F. Manipulation of Electron Orbitals in Hard-Wall InAs/InP Nanowire Quantum Dots. *Nano Lett.* **2011**, *11*, 1695–1699.

[98] Aichele, T.; Tribu, A.; Sallen, G.; Bocquel, J.; Bellet-Amalric, E.; Bougerol, C.; Poizat, J. P.; Kheng, K.; André, R.; Tatarenko, S.; Mariette, H. CdSe Quantum Dots in ZnSe Nanowires as Efficient Source for Single Photons up to 220 K. *J. Cryst. Growth* **2009**, *311*, 2123–2127.

[99] Renard, J.; Songmuang, R.; Tourbot, G.; Bougerol, C.; Daudin, B.; Gayral, B. Evidence for Quantum-Confined Stark Effect in GaN/AlN Quantum Dots in Nanowires. *Phys. Rev. B - Condens. Matter Mater. Phys.* **2009**, *80*, 2–5.

[100] Lu, Q.; Zhuang, Q.; Krier, A. Gain and Threshold Current in Type II In(As)Sb Mid-Infrared Quantum Dot Lasers. *Photonics* **2015**, *2*, 414–425.

[101] Sokura, L. A.; Nevedomskiy, V. N.; Bert, N. A. Structural Features of Indium Antimonide Quantum Dots on the Indium Arsenide Substrate. *St. Petersbg. Polytech. Univ. J. Phys. Math.* **2015**, *1*, 109–112.

[102] Lu, Q.; Zhuang, Q.; Marshall, A.; Kesaria, M.; Beanland, R.; Krier, A. InSb Quantum Dots for the Mid-Infrared Spectral Range Grown on GaAs Substrates Using Metamorphic InAs Buffer Layers. *Semicond. Sci. Technol.* **2014**, *29*, 075011–075018.

[103] Fan, D.; Li, S.; Kang, N.; Caroff, P.; Wang, L. B.; Huang, Y. Q.; Deng, M. T.; Yu, C. L.; Xu, H. Q. Formation of Long Single Quantum Dots in High Quality InSb Nanowires Grown by Molecular Beam Epitaxy. *Nanoscale* **2015**, *7*, 14822–14828.

[104] Anyebe, E. A. Recent Progress on the Gold-Free Integration of Ternary III–As Antimonide Nanowires Directly on Silicon. *Nanomaterials* **2020**, *10*, 2064.

[105] Borg, B. M.; Dick, K. A.; Eymery, J.; Wernersson, L. Enhanced Sb Incorporation in InAsSb Nanowires Grown by Metalorganic Vapor Phase Epitaxy Vapor Phase Epitaxy. *Appl. Phys. Lett.* **2011**, *98*, 113104–113106.

[106] Gao, Z.; Sun, J.; Han, M.; Yin, Y.; Gu, Y. Recent Advances in Sb-Based III – V Nanowires. *Nanotechnology* **2019**, *30*, 212002–212027.

[107] Pea, M.; Ercolani, D.; Li, A.; Gemmi, M.; Rossi, F.; Beltram, F.; Sorba, L. Suppression of Lateral Growth in InAs/InAsSb Heterostructured Nanowires. *J. Cryst. Growth* **2013**, *366*, 8–14.

[108] Chen, J. F.; Hsiao, R. S.; Huang, W. D.; Wu, Y. H.; Chang, L.; Wang, J. S.; Chi, J. Y. Strain Relaxation and Induced Defects in InAsSb Self-Assembled Quantum Dots. *Appl. Phys. Lett.* **2006**, *88*, 15–18.

[109] Bomphrey, J. J.; Ashwin, M. J.; Jones, T. S. The Formation of High Number Density InSb Quantum Dots, Resulting from Direct InSb/GaSb (001) Heteroepitaxy. *J. Cryst. Growth* **2015**, *420*, 1–5.

[110] Moiseev, K. D.; Parkhomenko, Y. A.; Ankudinov, A. V; Gushchina, E. V; Mikha, M. P.; Titkov, A. N.; Yakovlev, Y. P. InSb / InAs Quantum Dots Grown by Liquid Phase Epitaxy. *Tech. Phys. Lett.* **2007**, *33*, 295–298.

[111] Carrington, P. J.; Repiso, E.; Lu, Q.; Fujita, H.; Marshall, A. R. J.; Zhuang, Q.; Krier, A.; La, L. InSb Based Quantum Dot Nanostructures for Mid-Infrared Photonic Devices. *Proc. SPIE* **2016**, *9919*.

[112] Tasco, V.; Deguffroy, N.; Baranov, A. N.; Tournié, E.; Satpati, B.; Trampert, A.; Dunaevski, M.; Titkov, A. High-Density InSb-Based Quantum Dots Emitting in the Mid-Infrared. *J. Cryst. Growth* **2007**, *301–302*, 713–717.

[113] Mazur, Y. I.; Dorogan, V. G.; Salamo, G. J.; Tarasov, G. G.; Liang, B. L.; Reyner, C. J.; Nunna, K.; Huffaker, D. L. Coexistence of Type-I and Type-II Band Alignments in Antimony-Incorporated InAsSb Quantum Dot Nanostructures. *Appl. Phys. Lett.* **2012**, *100*, 033102–033105.

[114] Ting, D. Z.; Soibel, A.; Khoshakhlagh, A.; Keo, S. A.; Rafol, S. B.; Höglund, L.; Luong, E. M.; Fisher, A. M.; Hill, C. J.; Gunapala, S. D. Development of InAs/InAsSb Type II Strained-Layer Superlattice Unipolar Barrier Infrared Detectors. *J. Electron. Mater.* **2019**, *48*, 6145–6151.

[115] Jia, B. W.; Tan, K. H.; Loke, W. K.; Wicaksono, S.; Yoon, S. F. Growth and Characterization of InSb on (1 0 0) Si for Mid-Infrared Application. *Appl. Surf. Sci.* **2018**, *440*, 939–945.

[116] Tokumitsu, E.; Yamada, T.; Konagai, M.; Takahashi, K. Photo- metalorganic Molecular- beam Epitaxy: A New Epitaxial Growth Technique. *J. Vac. Sci. Technol. A Vacuum, Surfaces, Film.* **1989**, *7*, 706–710.

[117] Tsang, W. T. Chemical Beam Epitaxy of InP and GaAs. *Appl. Phys. Lett.* **1984**, *45*, 1234–1236.

[118] Tsang, W. T. Chemical Beam Epitaxy. *IEEE Circuits Devices Mag.* **1988**, *4*, 18–24.

[119] Egerton, R. F. Physical Principles of Electron Microscopy An Introduction to TEM, SEM, and AEM. In: *chemistry and Materials Science*, Springer, Boston, MA, **2005**.

[120] Wirth, R. Focused Ion Beam (FIB) Combined with SEM and TEM: Advanced Analytical Tools for Studies of Chemical Composition, Microstructure and Crystal Structure in Geomaterials on a Nanometre Scale. *Chem. Geol.* **2009**, *261*, 217–229.

[121] Rajput, N. S.; Luo, X. *FIB Micro-/Nano-Fabrication*, Second Edition.; Yi Qin, 2015.

[122] Richard, M. L. Focused Ion Beams Techniques for Nanomaterials Characterization. *Micro. Resear. And Tech.* **2006**, *69*, 538–549.

[123] Hÿtch, M. J.; Snoeck, E.; Kilaas, R. Quantitative Measurement of Displacement and Strain Fields from HREM Micrographs. *Ultramicroscopy* **1998**, *74*, 131–146.

[124] Grillo, V.; Rossi, F. STEM_CELL: A Software Tool for Electron Microscopy. Part 2 Analysis of Crystalline Materials. *Ultramicroscopy* **2013**, *125*, 112–129.

[125] Yan, X.; Fan, S.; Zhang, X.; Ren, X. Analysis of Critical Dimensions for Nanowire Core-Multishell Heterostructures. *Nanoscale Res. Lett.* **2015**, 10, 1–7.

[126] Ji, X.; Yang, X.; Du, W.; Pan, H.; Yang, T. Selective-Area MOCVD Growth and Carrier-Transport-Type Control of InAs(Sb)/GaSb Core-Shell Nanowires. *Nano Lett.* **2016**, *16*, 7580–7587.

[127] Vurgaftman, I.; Meyer, J. R.; Ram-Mohan, L. R. Band Parameters for III-V Compound Semiconductors and Their Alloys. *J. Appl. Phys.* **2001**, *89*, 5815–5875.

[128] Borg, B. M.; Dick, K. A.; Ganjipour, B.; Pistol, M. E.; Wernersson, L. E.; Thelander, C. InAs/GaSb Heterostructure Nanowires for Tunnel Field-Effect Transistors. *Nano Lett.* **2010**, *10*, 4080–4085.

[129] Abergel, D. S. L. Excitonic Condensation in Spatially Separated One-Dimensional Systems. *Appl. Phys. Lett.* **2015**, 106, 213104.

[130] De La Mata, M.; Magén, C.; Caroff, P.; Arbiol, J. Atomic Scale Strain Relaxation in Axial Semiconductor III-V Nanowire Heterostructures. *Nano Lett.* **2014**, *14*, 6614–6620.

[131] Liu, X.; Liu, P.; Huang, H.; Chen, C.; Jin, T.; Zhang, Y.; Huang, X.; Jin, Z.; Li, X.; Tang, Z. Growth and Large-Scale Assembly of InAs/InP Core/Shell Nanowire: Effect of Shell Thickness on Electrical Characteristics. *Nanotechnology* **2013**, *24*, 245306.

[132] Glas, F. Stress Relaxation in Nanowires with Heterostructures. In: *Wide Band Gap Semiconductor Nanowires 1*; Consonni, V., Feuillet, G., Eds.; ISTE Ltd and John Wiley & Sons, Inc, **2014**, pp 25−57.

[133] Lewis, R. B.; Nicolai, L.; Küpers, H.; Ramsteiner, M.; Trampert, A.; Geelhaar, L. Anomalous Strain Relaxation in Core-Shell Nanowire Heterostructures via Simultaneous Coherent and Incoherent Growth. *Nano Lett.* **2017**, *17*, 136–142.

[134] Arif, O.; Zannier, V.; Li, A.; Rossi, F.; Ercolani, D.; Beltram, F.; Sorba, L. Growth and Strain Relaxation Mechanisms of InAs/InP/GaAsSb Core-Dual-Shell Nanowires. *Cryst. Growth Des.* **2020**, *20*, 1088–1096.

[135] Oshima, M.; Watanabe, Y.; Heun, S.; Sugiyama, M.; Kiyokura, T. Initial Stages of Nanocrystal Semiconductors on Si Substrates. *J. Electron Spectros. Relat. Phenomena* **1996**, *80*, 129–132.

[136] Taguchi, A. First-Principles Investigations of Surface Reconstructions of an InAs(1 1 1)B Surface. *J. Cryst. Growth* **2005**, *278*, 468–472.

[137] Uccelli, E.; Arbiol, J.; Magen, C.; Krogstrup, P.; Russo-Averchi, E.; Heiss, M.; Mugny, G.; Morier-Genoud, F.; Nygård, J.; Morante, J. R.; et al. Three-Dimensional Multiple-Order Twinning of Self-Catalyzed GaAs Nanowires on Si Substrates. *Nano Lett.* **2011**, *11*, 3827–3832.

[138] Li, T.; Chen, Y.; Lei, W.; Zhou, X.; Luo, S.; Hu, Y.; Wang, L.; Yang, T.; Wang, Z. Effect of Growth Temperature on the Morphology and Phonon Properties of InAs Nanowires on Si Substrates. *Nanoscale Res. Lett.* **2011**, *6*, 463–469.

[139] Mandl, B.; Stangl, J.; Mårtensson, T.; Mikkelsen, A.; Eriksson, J.; Karlsson, L. S.; Bauer, G.; Samuelson, L.; Seifert, W. Au-Free Epitaxial Growth of InAs Nanowires. *Nano Lett.* **2006**, *6*, 1817–1821.

[140] Priante, G.; Ambrosini, S.; Dubrovskii, V. G.; Franciosi, A.; Rubini, S. Stopping and Resuming at Will the Growth of GaAs Nanowires. *Cryst. Growth Des.* **2013**, *13*, 3976–3984.

[141] Popovitz-Biro, R.; Kretinin, A.; Von Huth, P.; Shtrikman, H. InAs/GaAs Core-Shell Nanowires. *Cryst. Growth Des.* **2011**, *11*, 3858–3865.

[142] Fonseca, I. The Wulff Theorem Revisited. *Proceedings: Mathematical and Physical Sciences.* **1991**, *432*, 125–145.

[143] Lai, F.; Chen, Y.; Guo, H. Surface energies of non-centrosymmetric nanocrystals by the inverse Wulff construction method. *Phys. Chem. Chem. Phys.* **2019**, *21*, 16486–16496.

[144] Ishizuka, A.; Hytch, M.; Ishizuka, K. Stem Moiré Analysis for 2D Strain Measurements. *Microscopy* **2017**, *66*, 217–221.

[145] Grandal, J.; Wu, M.; Kong, X.; Hanke, M.; Dimakis, E.; Geelhaar, L.; Riechert, H.; Trampert, A. Plan-View Transmission Electron Microscopy Investigation of GaAs/(In,Ga)As Core-Shell Nanowires. *Appl. Phys. Lett.* **2014**, *105*, 121602.

[146] Yamaguchi, K.; Takeda, Y.; Kameda, K.; Itagaki, K. Measurements of Heat of Formation of GaP, InP, GaAs, InAs, GaSb, and InSb. *Mat. Trans. JIM* **1994**, *35*, 596–602.

[147] Andrews, D. A.; Davies, G. J. The Influence of Growth Conditions on the Growth Rate and Composition of GaAs and GaInAs Alloys Grown by Chemical Beam Epitaxy. *J. Appl. Phys.* **1990**, *67*, 3187–3189.

[148] Caridi, E. A.; Stark, J. B. Strain Tensor Elements for Misfit-Strained [hhk]-Oriented Cubic Crystals. *Appl. Phys. Lett.* **1992**, *60*, 1441–1443.

[149] Yu, P. Y.; Cardona, M. Vibrational Properties of Semiconductors, and Electron-Phonon Interactions. In: *Fundamentals Semiconductors Physics and Materials Properties*; Stanley, H. E., Rhodes, W. T., Eds.; fourth edition: Springer, Verlag Berlin Heidelberg, **2010**, pp 107–158.

[150] Kunert, B.; Mols, Y.; Baryshniskova, M.; Waldron, N.; Schulze, A.; Langer, R. How to Control Defect Formation in Monolithic III/V Hetero-Epitaxy on (100) Si? A Critical Review on Current Approaches. *Semicond. Sci. Technol.* **2018**, *33*, 093002.

[151] Tomioka, K.; Fukui, T. Recent progress in integration of III–V nanowire transistors on Si substrate by selective-area growth. *J. Phys. D: Appl. Phys.* **2014**, *47*, 394001–394013.

[152] Gudiksen, M. S.; Lauhon, L. J.; Wang, J.; Smith, D. C.; Lieber, C. M. Growth of nanowire superlattice structures for nanoscale photonics and electronics. *Nature* **2002**, *415*, 617–620.

[153] Lauhon, L. J.; Gudiksen, M. S.; Wang D.; Lieber, C. M. Epitaxial core–shell and core–multishell nanowire heterostructures. *Nature* **2002**, *420*, 57–61.

[154] Johansson, J.; Dick, K. A. Recent advances in semiconductor nanowire heterostructures. *Cryst. Eng. Comm.* **2011**, *13*, 7175–7184.

[155] Zhang, Y.; Wu, J.; Aagesen M.; Liu, H. III–V nanowires and nanowire optoelectronic devices. *J. Phys. D: Appl. Phys.* **2015**, *48*,463001–463029.

[156] Battiato, S.; Wu, S.; Zannier, V.; Bertoni, A.; Goldoni, G.; Li, A.; Xiao, S.; Han, X. D.; Beltram, F.; Sorba, L.; Xu, X.; Rossella, F. Polychromatic emission in a wide energy range from InP-InAs-InP multishell nanowires. *Nanotechnology* **2019**, *30*, 194004.

[157] Wu, S.; Peng, K.; Battiato, S.; Zannier, V.; Bertoni, A.; Goldoni, G.; Xie, X.; Yang, J.; Xiao S.; Qian, C.; Song, F.; Sun, S.; Dang, J.; Yu, Y.; Beltram, F.; Sorba, L.; Li, A.; Li, B.; Rossella, F.; Xu, X. Anisotropies of the g-factor tensor and diamagnetic coefficient in crystal-phase quantum dots. *Nano Res.* **2019**, *12*, 2842–2848.

[158] Roy, M.; De Luca, M.; Rurali, R.; Zardo, I. A review on III–V core–multishell nanowires: growth, properties, and applications. *J. Phys. D: Appl. Phys.* **2017**, *50*, 143001–143034.

[159] Ganjipour, B.; Ek, M.; Borg, B. M.; Dick, K. A.; Pistol, M.E.; Wernersson, L. E.; Thelander, C. Carrier control and transport modulation in GaSb/InAsSb core/shell nanowires. *Appl. Phys. Lett.* **2012**, *101*, 103501–103504.

[160] Esaki, L. Long journey into tunneling. *Proc. IEEE* **1974**, *62*, 825–831.

[161] Borg, B. M.; Ek, M.; Ganjipour, B.; De A. W.; Dick, K. A.; Wernersson, L. E. Thelander, C. Influence of doping on the electronic transport in GaSb/InAs(Sb) nanowire tunnel devices. *Appl. Phys. Lett.* **2012**, *101*, 043508–043511.

[162] Dey, A. W.; Borg, B. M.; Ganjipour, B.; Ek, M.; Dick K. A.; Lind, E.; Thelander, C.; Wernersson, L. High-Current GaSb/InAs(Sb) Nanowire Tunnel Field-Effect Transistors. *IEEE Electron Device Lett.* **2013**, *34*, 211–213.

[163] Ganjipour, B.; Dey, A. W.; Borg, B. M.; Ek, M.; Pistol, M. E.; Dick, K. A.; Wernersson, L. E.; Thelander, C. High Current Density Esaki Tunnel Diodes Based on GaSb-InAsSb Heterostructure Nanowires. *Nano Lett.* **2011**, *11*, 4222–4226.

[164] Zeng, X.; Otnes, G.; Heurlin, M.; Mourão, R. T.; Borgström, M. T. InP/GaInP nanowire tunnel diodes. *Nano Res.* **2018**, *11*, 2523–2531.

[165] Salimian, S.; Arif, O.; Zannier, V.; Ercolani, D.; Rossi, F.; Momtaz, Z. S.; Beltram, F.; Roddaro, S.; Rossella, F.; Sorba, L. Electrical probing of carrier separation in InAs/InP/GaAsSb core-dualshell nanowires. *Nano Res.* **2020**, *13*, 1065–1070.

[166] Caroff, P.; Wagner, J.B.; Dick, K.A.; Nilsson, H.A.; Jeppsson, M.; Deppert, K.; Samuelson, L.; Wallenberg, L.R.; Wernersson, L.E. High-Quality InAs/InSb Nanowire Heterostructures Grown by Metal-Organic Vapor-Phase Epitaxy. *Small* **2008**, *4*, 878–882.

[167] Li, L. K. Molecular-Beam Epitaxial Growth of InSb on GaAs and Si for Infrared Detector Applications. *J. Vac. Sci. Technol. B Microelectron. Nanom. Struct.* **1993**, *11*, 872–874.

[168] Ashley, T.; Buckle, L.; Datta, S.; Emeny, M. T.; Hayes, D. G.; Hilton, K. P.; Jefferies, R.; Martin, T.; Phillips, T. J.; Wallis, D. J.; Wilding, P. J.; Chau, R. Heterogeneous InSb quantum well transistors on silicon for ultra-high speed. *Electron. Lett.* **2005**, *43*, 777–779.

[169] Capper, P.; Irvine, S.; Joyce, T. Epitaxial Crystal Growth: Methods and Materials. In *Springer Handbook of Electronic and Photonic Materials*; Kasap, S., Capper, P., Eds.; Springer: Cham, Switzerland, 2017; pp. 309−341.

[170] Kanisawa, K.; Yamaguchi, H.; Hirayama, Y. Two-Dimensional Growth of InSb Thin Films on GaAs(111)A Substrates. *Appl. Phys. Lett.* **2000**, *76*, 589–591.

[171] Webb, J.L.; Knutsson, J.; Hjort, M.; Gorji Ghalamestani, S.; Dick, K.A.; Timm, R.; Mikkelsen, A. Electrical and Surface Properties of InAs/InSb Nanowires Cleaned by Atomic Hydrogen. *Nano Lett.* **2015**, *15*, 4865–4875.

[172] Anandan, D.; Kakkerla, R.K.; Yu, H.W.; Ko, H.L.; Nagarajan, V.; Singh, S.K.; Lee, C.T.; Chang, E.Y. Growth of Foreign-Catalyst-Free Vertical InAs/InSb Heterostructure Nanowires on Si (1 1 1) Substrate by MOCVD. *J. Cryst. Growth* **2019**, *506*, 45–54.

[173] Caroff, P.; Messing, M.E.; Mattias Borg, B.; Dick, K.A.; Deppert, K.; Wernersson, L.E. InSb Heterostructure Nanowires: MOVPE Growth under Extreme Lattice Mismatch. *Nanotechnology* **2009**, *20*, 495606–495612.

[174] Li, A.; Sibirev, N.V.; Ercolani, D.; Dubrovskii, V.G.; Sorba, L. Readsorption Assisted Growth of InAs/InSb Heterostructured Nanowire Arrays. *Cryst. Growth Des.* **2013**, *13*, 878–882.

[175] Nilsson, H.A.; Caroff, P.; Thelander, C.; Larsson, M.; Wagner, J.B.; Wernersson, L.E.; Samuelson, L.; Xu, H.Q. Giant, Level-Dependent g Factors in InSb Nanowire Quantum Dots. *Nano Lett.* **2009**, *9*, 3151–3156.

[176] Lugani, L.; Ercolani, D.; Beltram, F.; Sorba, L. Growth Mechanism of InAs-InSb Heterostructured Nanowires Grown by Chemical Beam Epitaxy. *J. Cryst. Growth* **2011**, *323*, 304–306.

[177] Li, T.; Gao, L.; Lei, W.; Guo, L.; Pan, H.; Yang, T.; Chen, Y.; Wang, Z. InAs-Mediated Growth of Vertical InSb Nanowires on Si Substrates. *Nanoscale Res. Lett.* **2013**, *8*, 333–338.

[178] Lugani, L.; Ercolani, D.; Sorba, L.; Sibirev, N.V.; Timofeeva, M.A.; Dubrovskii, V.G. Modeling of InAs-InSb Nanowires Grown by Au-Assisted Chemical Beam Epitaxy. *Nanotechnology* **2012**, *23*, 095602–095609.

[179] Badawy, G.; Gazibegovic, S.; Borsoi, F.; Heedt, S.; Wang, C.; Koelling, S.; Verheijen, M.A.; Kouwenhoven, L.P.; Bakkers, E.P.A.M. High Mobility Stemless InSb Nanowires. *Nano Lett.* **2019**, *19*, 3575–3582.

[180] Colombo, C.; Spirkoska, D.; Frimmer, M.; Abstreiter, G.; Fontcuberta, I.; Morral, A. Ga-Assisted Catalyst-Free Growth Mechanism of GaAs Nanowires by Molecular Beam Epitaxy. *Phys. Rev. B* **2008**, *77*, 155326–155330.

[181] Dubrovskii, V.G. Theory of VLS growth of compound semiconductors. In *Semiconductors and Semimetals*; Fontcuberta i Morral, A., Dayeh, S.A., Jagadish, C., Eds.; Academic Press: Burlington, MA, USA, 2015; Volume 93, pp. 1−78.

[182] So, H.; Pan, D.; Li, L.; Zhao, J. Foreign-Catalyst-Free Growth of InAs/InSb Axial Heterostructure Nanowires on Si (111) by Molecular-Beam Epitaxy. *Nanotechnology* **2017**, *28*, 135704–135712.

[183] Pozuelo, M.; Zhou, H.; Lin, S.; Lipman, S.A.; Goorsky, M.S.; Hicks, R.F.; Kodambaka, S. Self-Catalyzed Growth of InP/InSb Axial Nanowire Heterostructures. *J. Cryst. Growth* **2011**, *329*, 6–11.

[184] Arif, O.; Zannier, V.; Dubrovskii, V. G.; Shtrom, I. V.; Rossi, F.; Beltram, F.; Sorba, L. Growth of Self-Catalyzed InAs/InSb Axial Heterostructured Nanowires: Experiment and Theory. *Nanomaterials* **2020,** *10*, 494.

[185] Yuan, Y.; Randall Lee, T. Contact angle and wetting properties. In *Surface Science Techniques*; Bracco, G., Holst, B., Eds.; Springer Series in Surface Sciences; Springer: Berlin/Heidelberg, Germany, 2013; Volume 51, pp. 3−34.

[186] Panciera, F.; Baraissov, Z.; Patriarche, G.; Dubrovskii, V.G.; Glas, F.; Travers, L.; Mirsaidov, U.; Harmand, J.C. Phase selection in self-catalyzed GaAs nanowires. *Nano Lett.* **2020**, *20*, 1669–1675.

[187] Robson, M.; Azizur-Rahman, K.M.; Parent, D.; Wojdylo, P.; Thompson, D.A.; Lapierre, R.R. Multispectral Absorptance from Large-Diameter InAsSb Nanowire Arrays in a Single Epitaxial Growth on Silicon. *Nano Futur.* **2017**, *1*, 035001–035007.

[188] Sokolovskii, A.S.; Robson, M.T.; Lapierre, R.R.; Dubrovskii, V.G. Modeling Selective-Area Growth of InAsSb Nanowires. *Nanotechnology* **2019**, *30*, 285601–285607.

[189] Glas, F.; Ramdani, M.R.; Patriarche, G.; Harmand, J.C. Predictive Modeling of Self-Catalyzed III-V Nanowire Growth. *Phys. Rev. B* **2013**, *88*, 195304–195317.

[190] Salim, S.; Lim, C. K.; Jensen, F. Gas-phase Decomposition Reactions of Tris(dimethylamino)phosphine, -arsine, and -stibine reagents. *Chem. Mater.* **1995**, *7*, 507-516.

[191] Glas, F.; Harmand, J. C.; Patriarche, G. Why Does Wurtzite Form in Nanowires of III-V Zinc Blende Semiconductors? *Phys. Rev. Lett.* **2007**, *99*, 146101–146104.

[192] Wen, C. Y.; Tersoff, J.; Hillerich, K.; Reuter, M. C.; Park, J. H.; Kodambaka, S.; Stach, E. A.; Ross, F. M. Periodically Changing Morphology of the Growth Interface in Si, Ge, and GaP Nanowires. *Phys. Rev. Lett.* **2011**, *107*, 025503–025506.

[193] Jacobsson, D.; Panciera, F.; Tersoff, J.; Reuter, M. C.; Lehmann, S.; Hofmann, S.; Dick, K. A.; Ross, F. M. Interface Dynamics and Crystal Phase Switching in GaAs Nanowires. *Nature* **2016**, *531*, 317–322.

[194] Dubrovskii, V. G.; Sibirev, N. V.; Halder, N. N.; Ritter, D. Classification of the Morphologies and Related Crystal Phases of III–V Nanowires Based on the Surface Energy Analysis. *J. Phys. Chem. C* **2019**, *123*, 18693–18701.

[195] Kim, W.; Dubrovskii, V.G.; Vukajlovic-Plestina, J.; Tütüncüoglu, G.; Francaviglia, L.; Güniat, L.; Potts, H.; Friedl, M.; Leran, J.B.; Fontcuberta, I.; et al. Bistability of Contact Angle and Its Role in Achieving Quantum-Thin Self-Assisted GaAs Nanowires. *Nano Lett.* **2018**, *18*, 49–57.

[196] Dubrovskii, V.G.; Xu, T.; Álvarez, A.D.; Plissard, S.R.; Caroff, P.; Glas, F.; Grandidier, B. Self-Equilibration of the Diameter of Ga-Catalyzed GaAs Nanowires. *Nano Lett.* **2015**, *15*, 5580–5584.

[197] Leshchenko, E.D.; Kuyanov, P.; LaPierre, R.R.; Dubrovskii, V.G. Tuning the morphology of self-assisted GaP nanowires. *Nanotechnology* **2018**, *29*, 225603–2256609.

[198] Dubrovskii, V.G.; Sibirev, N.V.; Berdnikov, Y.; Gomes, U.P.; Ercolani, D.; Zannier, V.; Sorba, L. Length Distributions of Au-Catalyzed and In-Catalyzed InAs Nanowires. *Nanotechnology* **2016**, *27*, 375602–375610.

[199] Dubrovskii, V.G.; Berdnikov, Y.; Schmidtbauer, J.; Borg, M.; Storm, K.; Deppert, K.; Johansson, J. Length distributions of nanowires growing by surface diffusion. *Cryst. Growth Des.* **2016**, *16*, 2167–2172.

[200] Tersoff, J. Stable Self-Catalyzed Growth of III-V Nanowires. *Nano Lett.* **2015**, *15*, 6609–6613.

[201] Glas, F. Vapor Fluxes on the Apical Droplet during Nanowire Growth by Molecular Beam Epitaxy. *Phys. Status Solidi B* **2010**, *247*, 254–258.

[202] Dubrovskii, V.G. Development of Growth Theory for Vapor-Liquid-Solid Nanowires: Contact Angle, Truncated Facets, and Crystal Phase. *Cryst. Growth Des.* **2017**, *17*, 2544–2548.

[203] Dubrovskii, V.G. Stabilization of the Morphology and Crystal Phase in Ensembles of Self- Catalyzed GaAs Nanowires. *Phys. Status Solidi Rapid Res. Lett.* **2019**, *13*, 1900301–1900305.

[204] Prete, D.; Erdman, P. A.; Demontis, V.; Zannier, V.; Ercolani, D.; Sorba, L.; Beltram, F.; Rossella, F.; Taddei, F.; Roddaro, S. Thermoelectric Conversion at 30 K in InAs/InP Nanowire Quantum Dots. *Nano Lett.* **2019**, *19*, 3033–3039.

[205] Sadre Momtaz, Z.; Servino, S.; Demontis, V.; Zannier, V.; Ercolani, D.; Rossi, F.; Rossella, F.; Sorba, L.; Beltram, F.; Roddaro, S. Orbital Tuning of Tunnel Coupling in InAs/InP Nanowire Quantum Dots. *Nano Lett.* **2020**, *20*, 1693–1699.

[206] Harmand, J.; Liu, L.; Patriarche, G.; Tchernycheva, M.; Photonique, L. De; Nanostructures, D.; Nozay, D. Potential of Semiconductor Nanowires for Single Photon Sources. *Proc. SPIE*, **2009**, *7222*, 1–10.

[207] Dalacu, D.; Mnaymneh, K.; Lapointe, J.; Wu, X.; Poole, P. J.; Bulgarini, G.; Zwiller, V.; Reimer, M. E. Ultraclean Emission from InAsP Quantum Dots in Defect-Free Wurtzite InP Nanowires. *Nano Lett.* **2012**, *12*, 5919–5923.

[208] Dalacu, D.; Mnaymneh, K.; Wu, X.; Lapointe, J.; Aers, G. C.; Poole, P. J.; Robin, L.; Dalacu, D.; Mnaymneh, K.; Wu, X.; Lapointe, J.; Aers, G. C.; Poole, P. J.; Williams, R. L. Selective-Area Vapor-Liquid-Solid Growth of Tunable InAsP Quantum Dots in Nanowires. *Appl. Phys. Lett.* **2011**, *98*, 251101–251103.

[209] Svensson, S. F.; Jeppesen, S.; Thelander, C.; Samuelson, L.; Linke, H.; Dick, K. A. Control and Understanding of Kink Formation in InAs-InP Heterostructure Nanowires. *Nanotechnology* **2013**, *24*, 345601–345609.

[210] Ercolani, D.; Gemmi, M.; Nasi, L.; Rossi, F.; Pea, M.; Li, A.; Salviati, G.; Beltram, F.; Sorba, L. Growth of InAs/InAsSb Heterostructured Nanowires. *Nanotechnology* **2012**, *23*, 115606–115614.

[211] Arif, O.; Zannier, V.; Rossi, F.; Ercolani, D.; Beltram, F.; Sorba, L. Self-Catalyzed InSb/InAs Quantum Dot Nanowires. *Nanomaterials* **2021,** *11*, 179.

[212] Li, B.; Yan, X.; Zhang, X.; Ren, X. Self-Catalyzed Growth of InAs Nanowires on InP Substrate. *Nanoscale Res. Lett.* **2017**, *12*, 3–7.

[213] Yan, X.; Zhang, X.; Li, J.; Wu, Y.; Ren, X. Self-Catalyzed Growth of Pure Zinc Blende ⟨110⟩ InP Nanowires. *Appl. Phys. Lett.* **2015**, *107*, 023101–023105.

[214] Yamaguchi, M.; Horiuchi, I.; Paek, J. H.; Sawaki, N. In-Assisted Catalyst-Free MBE-VLS Growth of InAs Nanowires on Si Substrate. *AIP Conf. Proc.* **2011**, *1399*, 229–230.

[215] Hertenberger, S.; Rudolph, D.; Becker, J.; Bichler, M.; Finley, J. J.; Abstreiter, G.; Koblmüller, G. Rate-Limiting Mechanisms in High-Temperature Growth of Catalyst-Free InAs Nanowires with Large Thermal Stability. *Nanotechnology* **2012**, *23*, 235602–235613.

[216] Rudolph, D.; Hertenberger, S.; Bolte, S.; Paosangthong, W.; Spirkoska, D.; Döblinger, M.; Bichler, M.; Finley, J. J.; Abstreiter, G.; Koblmüller, G. Direct

Observation of a Noncatalytic Growth Regime for GaAs Nanowires. *Nano Lett.* **2011**, *11*, 3848–3854.

[217] Küpers, H.; Lewis, R. B.; Tahraoui, A.; Matalla, M.; Krüger, O.; Bastiman, F.; Riechert, H.; Geelhaar, L. Diameter Evolution of Selective Area Grown Ga-Assisted GaAs Nanowires. *Nano Res.* **2018**, *11*, 2885–2893.

[218] Oehler, F.; Cattoni, A.; Scaccabarozzi, A.; Patriarche, G.; Glas, F.; Harmand, J. C. Measuring and Modeling the Growth Dynamics of Self-Catalyzed GaP Nanowire Arrays. *Nano Lett.* **2018**, *18*, 701–708.